

Diffractive Dark-Ground Imaging of Ultra-Low Atom-Numbers in a MOT

Konstantinidis Gregory-Orfeus

*Supervisors: Wolf von Klitzing
Peter Rakitzis*



IESL - FORTH



University of Crete

December 2011

Abstract

*Submitted to the University of Crete
in partial fulfillment
of the requirements for the degree of
Doctor of Philosophy*

In this work, the theoretical principles of laser cooling and magneto-optical trapping are presented, and the magneto-optical trap (MOT) of the experiment is characterized for the loading and loss rates. By using fluorescence imaging, single atom resolution is achieved in the MOT. The theory of diffractive dark-ground imaging is presented, along technical considerations for the implementation of the technique. Imaging techniques of high sensitivity and resolution are vital to the study of the quantum phenomena inherent with cold atom ensembles and in the interactions between single particles. We implement diffractive dark-ground imaging as a sensitive technique to detect small cold atomic samples at very low optical densities prepared in a MOT. The originally achieved single atom resolution in the MOT by fluorescence imaging allows for the calibration of the atom number measured with fluorescence imaging, which is used as a reference to the atom number measured with diffractive dark-ground imaging. The diffractive dark-ground technique is used to image free expanding atom clouds released from a MOT of atom numbers down to 100 and optical densities down to 0.01 at an exposure time of 100 μs . The same technique applied on a BEC setup has resulted in the detection of atom numbers down to 7 atoms at the same range of optical densities, and it displays an improvement to the signal to noise ratio of a factor of 10 compared to classical absorption imaging.

Acknowledgements

The work for this thesis was done in the Cretan Matter Waves laboratory at the Institute of Electronic Structure and Lasers (I.E.S.L.) of the Foundation for Research and Technology (FO.R.T.H.) in Crete. I thank the supervisor, Dr. Wolf von Klitzing, for providing me with the opportunity to do the experiments and for his advising on the experiments. I thank the supervising professor, Prof. Petros Rakitzis, and Prof. Dimitris Charalambidis, members of the three-member Consulting Committee, for their support on the PhD. I thank Prof. Nikos Flytzanis, Prof. Grigoris Athanasiou, Dr. Paris Tzallas, Prof. Olivier Morizot, for attaining to the seven-member Jury Committee and for their presence in the thesis presentation.

I would like to thank the post-docs of the group Mark Baker, Paul C. Condylis, Daniel S. Sanchez, Jules Grucker, Michael Morrissey, Aggelos Lazoudis for their support and willingness to provide helpful advice, and especially Olivier Morizot for his work and for teaching me several things on the experiment. I thank the PhD co-students Melina Pappa and Vasiliki Bolpasi for the nice time and the fun we shared on our cooperation and discussions. I thank the master students Waldemar Deibel and especially Gustav Wikström for his partnership and work on the experiment.

I thank all the people in FORTH, the researchers, the professors, the students, the technical support staff for their help in the course of this work, and especially the people in the machine workshop for without their constructions the experiments wouldn't have been possible.

I thank my friends, everyone.

Contents

Abstract	iii
1 Introduction	1
2 Trapping of Atoms in a Magneto-Optical Trap	3
2.1 Radiation Pressure and Doppler cooling	3
2.1.1 The Doppler cooling limit	6
2.2 Quadrupole magnetic field	8
2.2.1 Atoms in the Magnetic Potential	9
2.2.2 The Magneto-Optical Trap	10
2.3 Loading of Atoms into the Trap	14
2.4 Collisional losses in the MOT	16
2.4.1 Collisions with the background gases	16
2.4.2 Light-assisted collisions in the trap	17
2.4.3 The lifetime of the MOT	19
3 Theory on Imaging Techniques	21
3.1 Atom-light interactions	21
3.2 Absorption imaging	22
3.3 Fourier-filtering techniques	24
3.3.1 Dispersive dark-ground imaging	25
3.3.2 Phase-contrast imaging	27
3.3.3 Other imaging techniques	27
3.4 Diffractive dark-ground imaging	28
3.4.1 The light field in diffraction dark-ground imaging	28
3.4.2 Fourier treatment of diffractive dark-ground imaging	30
3.4.3 Background level on the images	34
3.4.4 Dark spot size	34
3.4.5 Diffusion and expansion of the atom cloud during the imaging time	37
4 The Experimental Setup	41
4.1 Lasers system	41
4.1.1 Hyperfine structure of ^{87}Rb	42
4.1.2 Extended cavity master laser	42

4.1.3	Slave laser	45
4.1.4	The AOM board	47
4.2	The vacuum system	50
4.2.1	The getter source	51
4.2.2	The octagon glass cell	52
4.3	The magnetic coils	52
4.4	The MOT	54
4.5	The imaging system	55
4.5.1	The CCD camera	55
4.5.2	The imaging system	57
4.5.3	Auxiliary detection system	59
5	Fluorescence Imaging of a Single Atom	63
5.1	Fluorescence imaging of trapped single atoms with the CCD	64
5.2	Lifetime of single atoms in the MOT	67
6	Diffractive Dark-Ground Imaging of Low-Atom Clouds	71
6.1	Alignment of the imaging optics	71
6.2	Sequence of the experiment	73
6.3	Imaging atom clouds with diffractive dark-ground imaging	74
6.4	Conclusions	79
A	Constants and Rb Properties	81

List of Figures

2.1	The Scattering Force	5
2.2	Plot of the Scattering Force over Atom Velocity	6
2.3	Magnetic Field Lines for the Quadrupole Field	9
2.4	Simulated Quadrupole Field Profile	10
2.5	Zeeman Effect and Space Dependence of the Scattering Force	11
2.6	The Magneto-Optical Trap	13
2.7	Loading Curve of the MOT	16
3.1	Optical Path for Absorption Imaging, Dispersive Dark-Ground Imaging and Phase-Shift Imaging	26
3.2	Optical Path for Diffractive Dark-Ground Imaging	29
3.3	Absorption Profile $k(x)$ and Image Profile without Background	32
3.4	Image Profiles with Residual Background	35
3.5	Transmission Curves of the Light from the Atoms and of the Probe Light	36
4.1	Hyperfine Level Structure of the D_2 Line of ^{87}Rb	43
4.2	Frequency Stabilization Diagram	45
4.3	Schematic of the Slave Laser Layout	46
4.4	Spectrum of the Slave Laser	48
4.5	Schematic of the AOM Board	49
4.6	AOM Operation Principle	50
4.7	The Vacuum System	51
4.8	Schematic of the Dispensers	52
4.9	Coils Dimensions	53
4.10	Measured B-field of the Coils	54
4.11	Variation of the Magnetic Field Gradient with Coil Distance	55
4.12	Block Diagram of the Light and MOT Optical Layout	56
4.13	Imaging System Layout	58
4.14	Auxiliary Detection System	60
4.15	Picture of the Setup	61
5.1	Fluorescence over Time in a Low-Atom Number MOT with the CCD Camera	65
5.2	Fluorescence Images of Low-Atom Numbers	66

5.3	Histogram of Occurrence of Total Counts of Fluorescence Images in a Low-Atom Number MOT	67
5.4	Fluorescence over Time in a Low-Atom Number MOT with the SPCM	69
5.5	Histogram of the Duration Times	70
5.6	Histogram of the Capturing Times	70
6.1	Resolution Target	72
6.2	Beam Profile and Image of the Dark Spot	73
6.3	Diffractive Dark-Ground Images of Low-Atom Numbers	74
6.4	Atom Number with Diffractive Dark-Ground Imaging	75
6.5	Illumination Time and Beam Intensity	78

List of Tables

A.1	Fundamental constants	81
A.2	Rubidium 87 Physical Properties	82
A.3	Rubidium 87 D ₂ Optical Properties	82
A.4	Rubidium 87 D Field Interaction Properties	83

Chapter 1

Introduction

In cold atom experiments the imaging of the atomic sample is a fundamental part of the experiment for extracting information about the cold atomic sample. The most commonly used imaging technique is absorption imaging, where a probe beam illuminating the sample is partially absorbed by the atoms, and the shadow of the atom cloud is observed at the image plane. Absorption imaging has been extensively used in experiments of cold atomic samples and Bose-Einstein condensates (for example in [1]) as a tool to study the sample itself and extract information about its size, its temperature and for measuring its atom number.

In the same scientific field, several other techniques based on the interaction of a probe beam with the sample of cold atoms have been developed from classical absorption imaging with two main goals being to image non-destructively and/or increase the sensitivity of the imaging technique.

In Fourier-filtering imaging, the unscattered probe light is processed at the Fourier plane of the collection optics. The principles of Fourier-filtering had been commonly used in microscopy, before they were introduced to the imaging of cold atomic samples. In dark field microscopy, the unscattered probe light is excluded from the image by an opaque object which results in a bright image on a dark background. In phase-contrast microscopy, the phase shifts of the probe light are observed as contrast changes in the image. Fritz Zernike was awarded the Nobel prize in 1953 for introducing the phase-contrast method in 1934 [2, 3]. Phase-contrast illumination mode is used in microscopes up to this day to provide contrast images of transparent living specimens.

In analogy to the aforementioned principles used in microscopy, imaging techniques for cold atomic samples has been developed, such as dispersive imaging and phase-contrast imaging, among others. Phase-contrast imaging has been used in the non-destructive imaging of macroscopic coherence phenomena in ultra-cold atoms in a BEC [4, 5]. Classical absorption imaging, mainly due to its straightforward nature, is still being employed and has recently revealed quantum phenomena in macroscopic coherent atomic samples such as the observation of tunneling in a Josephson junction between two BEC's [6] and squeezing and entanglement in a BEC [7].

Furthermore, in the last few years there has been an increasing interest in the

field of quantum information and, more generally, of quantum interaction of single particles, which entails for example the realization of a single photon source [8] and single photon –single atom entanglement [9, 10]. The detection of highly localized single atoms in tightly confining traps relevant to the above applications has been achieved mainly with fluorescence imaging. In this technique the fluorescence light emitted by the atom in a field of light is collected for imaging.

Throughout this work, the cold atomic samples used for the experiments have been prepared in a magneto-optical trap (MOT) [11]. The confinement of atoms in the magneto-optical trap is based on cooling the atoms down with laser light and combining the laser cooling with magnetic fields to achieve confinement of the atoms. In 1997, the Nobel prize in physics has been awarded to S. Chu, W. D. Phillips and C. Cohen-Tannoudji ([12–14]) for their contribution on developing the laser cooling techniques which led to the creation of the MOT. The MOT has been used extensively in cold atom experiments for the preparation of cold atomic samples, and as an atom source for the realization of BEC.

In this work we are able to trap single atoms and observe their presence in the MOT by means of fluorescence imaging. Single atoms have been observed for the first time in a MOT in 1994 by Z. Hu and H. J. Kimble [15]. We employ diffraction dark-ground imaging, a Fourier-filtering technique based on the dark ground (or "dark field") principle, as a sensitive technique to detect weak signals from small cold atomic samples at very low optical densities. The technique is applied on free expanding atom clouds released from a MOT, which display a very low optical density. Future scope with this technique is the detection of even lower atom numbers down to a single atoms by using a higher optical resolution.

The structure of this work is as follows: in Chapter 2, the magneto-optical trap and its principles of operation are discussed. A brief overview of the parameters of the MOT in our experiment is given. The lifetime of the atom cloud, and the lifetime of single atoms in a MOT are discussed.

In Chapter 3, the theoretical background of the most common imaging techniques, such as absorption imaging and phase-contrast is discussed. The diffractive dark-ground technique is presented, a Fourier analysis of the imaging process is given and several imaging parameters are discussed.

In Chapter 4, the experimental setup is described that consists namely of the vacuum system, the laser system, the magneto-optical trap and the imaging system.

In Chapter 5, the trapping of single atoms in a MOT is observed with fluorescence imaging. The lifetime of single atoms in the MOT is measured.

In Chapter 6, diffractive dark-ground imaging is used to image free expanding atom clouds released from a MOT. The imaged atom clouds display a very low optical density. The atom number measured with diffractive dark-ground imaging is compared to the atom number measured with fluorescence imaging.

Chapter 2

Trapping of Atoms in a Magneto-Optical Trap

The light force exerted on atoms due to scattering of photons has been used to develop laser cooling as a tool for slowing down atoms. Initially, the light force was used by W. D. Phillips to slow down an atomic beam [16]. The three dimensional cooling of an atomic vapor known as the optical molasses technique was realized by S. Chu and co-workers [17]. The application of these techniques resulted in low temperature atomic vapor samples, and made it possible for the cold atomic sample to be loaded into magnetic confining potentials. This led to the development of the magneto-optical trap (MOT) [11]. The confinement of atoms in the magneto-optical trap has been used extensively in cold atom experiments for the preparation of cold atomic samples. The occurrence of temperatures within the optical molasses technique below the Doppler limit, which was the theoretical limit by that time, was explained later by C. Cohen-Tannoudji and J. Dalibard [18], and S. Chu and co-workers [19].

In 1997, the Nobel prize in physics has been awarded to S. Chu, W. D. Phillips and C. Cohen-Tannoudji ([12–14]) for their contribution on developing the laser cooling techniques.

In our experiments we use the magneto-optical trap to prepare a cold atomic sample, which will be used as an object for the application of fluorescence imaging and the development of our diffractive dark-ground imaging technique.

2.1 Radiation Pressure and Doppler cooling

The radiation of light applied to an atom results in the excitation of the atom by the absorption of photons from the light field. Each photon carries momentum equal to $\hbar k$, where $k = 2\pi/\lambda$ is the laser beam's wave-vector. According to the conservation of momentum, each absorbed photon will transfer momentum to the atom equal to $\hbar k$ to the direction of the photon's motion. For an atom moving with a direction opposite to a beam of light, the momentum transfer from the absorbed photons to the atom will have a direction opposite to the motion of the atom, whereas the

momentum from the re-emitted photons towards all directions averages out. This results in an average scattering force that is slowing the atom down. The magnitude of the scattering force equals

$$F_{\text{sc}} = \hbar k R_{\text{sc}} , \quad (2.1)$$

where R_{sc} is the scattering rate of photons given by

$$R_{\text{sc}} = \frac{\Gamma}{2} \frac{I/I_s}{1 + I/I_s + 4\delta^2/\Gamma^2} . \quad (2.2)$$

For a two-level atom interacting with radiation the scattering force is given by [20]

$$F_{\text{sc}} = \hbar k \frac{\Gamma}{2} \frac{I/I_s}{1 + I/I_s + 4\delta^2/\Gamma^2} , \quad (2.3)$$

where Γ is the spontaneous decay rate of the excited state, I is the intensity of the laser beam and I_s is the saturation intensity. The frequency detuning

$$\delta = (\omega - \omega_0) - \vec{k} \cdot \vec{v} \quad (2.4)$$

is the laser beam's detuning $\omega - \omega_0$ from the resonance frequency ω_0 of the atomic transition taking into account the Doppler shift kv due to the movement of the atom. At high intensities the scattering force tends to the maximum $\hbar k \Gamma/2$, which results in a maximum deceleration of $a_{\text{max}} = \hbar k (\Gamma/2)/M$ for an atom of mass M . For a rubidium atom the maximum acceleration due to radiation pressure is $a_{\text{max}} \approx 10^5 \text{ m s}^{-2}$, which is 10^4 times larger than the acceleration due to gravity.

Each photon that is being absorbed or emitted by an atom results in a change of momentum of $\hbar k$ on the atom. For an atom of mass M the recoil velocity v_{rec} is the velocity of the atom for absorbing or emitting a photon at wavelength λ given by

$$v_{\text{rec}} = \frac{\hbar k}{M} = \frac{h}{\lambda M} . \quad (2.5)$$

In atom cooling experiments atoms are moving towards all directions. Therefore atom cooling is employed three-dimensionally by means of three pairs of counter-propagating laser beams, one pair along each Cartesian axis. The laser beams are derived from the same laser and have a frequency ω . The laser is red detuned, which means its frequency is lower than the resonance frequency of the atomic transition. We first consider the case in one dimension of a pair of counter-propagating laser beams and an atom moving towards one direction (Fig. 2.1). Due to the Doppler effect, the beam propagating along the same direction with the atom will have its frequency reduced as $\omega - kv$ taking it even further below resonance. The beam propagating in the opposite direction will have its frequency increased as $\omega + kv$ bringing it closer to the resonance. Therefore, the atom will scatter preferably photons from the beam opposite to its motion and experience a mean radiation force that is slowing the atom down.

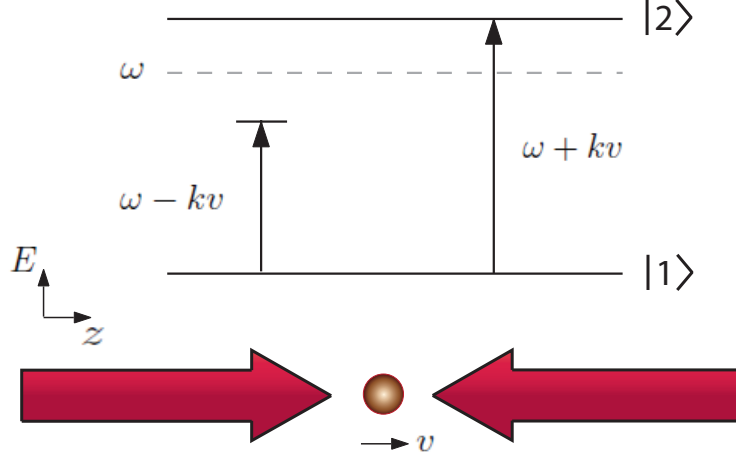


Figure 2.1: A pair of counter-propagating laser beams of frequency ω applied on an atom moving with velocity v along the z -axis. Due to the Doppler effect the frequency of the beam moving opposite to the atom is brought closer to resonance, thus the atom scatters more photons from the beam opposite to its motion.

The force arising from such an imbalance in the scattering of photons from the two counter-propagating beams can be written as

$$F_z = F_{\text{sc}}(\omega - \omega_0 - kv) - F_{\text{sc}}(\omega - \omega_0 + kv). \quad (2.6)$$

The previous equation in the limit of low velocities $kv \ll \delta$ can be written as

$$F_z \simeq \frac{8\hbar k^2 v \delta}{\Gamma} \frac{I/I_s}{(1 + I/I_s + 4\delta^2/\Gamma^2)^2}. \quad (2.7)$$

The force of the two counter-propagating beams acting on the atom is plotted in Fig. 2.2 as a function of the velocity of the atom. For $\omega - \omega_0 < 0$ (red detuning) the gradient of the net force is negative at small velocities, leading to the deceleration of the atom. The net force varies linearly with velocity as

$$F_{\text{molasses}} = -\alpha v, \quad (2.8)$$

where α is the friction coefficient and for red-detuned light is given by

$$\alpha = -\frac{8\hbar k^2 \delta}{\Gamma} \frac{I/I_s}{(1 + I/I_s + 4\delta^2/\Gamma^2)^2}. \quad (2.9)$$

The net force has its maxima where $kv = \pm\delta$. The capture velocity for the one-dimensional model is the velocity at the force maxima given by $v_c = \pm\delta/k$. By the fact that atoms are scattering photons at a rate R_{sc} , and that each scattered photon slows the atom down by v_{rec} , one is able to calculate the distance required to stop an atom of initial velocity v_c as

$$d = \frac{v_c^2}{2R_{\text{sc}} v_{\text{rec}}}. \quad (2.10)$$

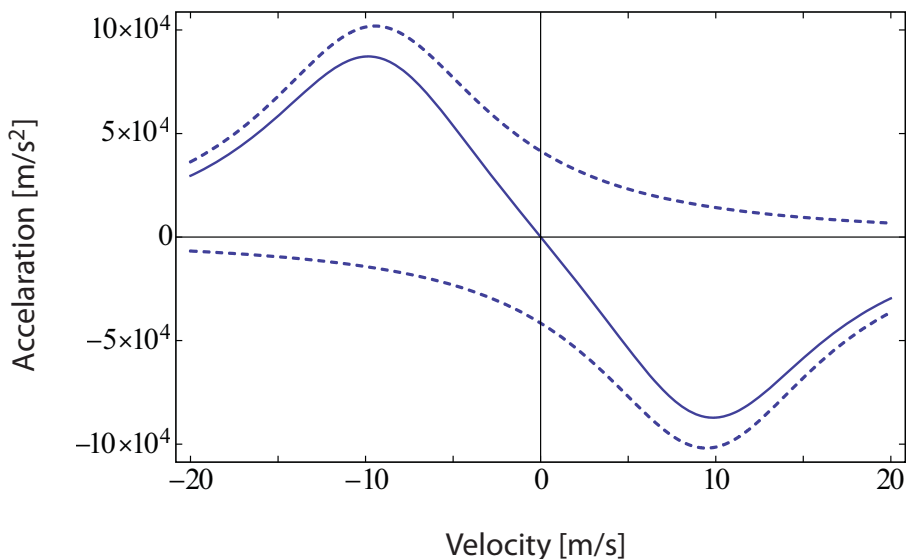


Figure 2.2: The force from the radiation pressure on the atom from two red-detuned counter-propagating laser beams. Dashed line shows the force from each beam, solid line shows the sum of the two beam. The parameters have been chosen as $I = I_s$ and $\delta = -2\Gamma$.

The principle of the one-dimensional cooling can be generalized to the three dimensions. The three pairs of counter-propagating laser beams intersect in the middle resulting in cooling the atom cloud from all directions. The atom is experiencing a damping force from the light, therefore, the atoms being cooled by the intersecting light beams are considered to be within a viscous medium, which is called an "optical molasses". The name "optical molasses", which refers to a syrup or honey-like medium, was given by the group who first realized this cooling technique in 1985 ([17]).

The dependence of the molasses force to the velocity of the atom, although the slowing down of an atom is achieved, means that the molasses force cannot lead to the trapping of the atom, since the force tends to 0 for $v \rightarrow 0$ at any point in space.

2.1.1 The Doppler cooling limit

The cooling process, where the atoms are slowed down by the photon momentum of absorbing photons, is counterbalanced by the diffusion of atoms in the momentum space, which occurs due to the recoil of spontaneously emitted photons towards a random direction and due to fluctuations in the absorption of the cooling light. The cooling down by the light force and the thermalization due to diffusion are two competing processes, and although an overall cooling of the atoms occurs, towards lower velocities an equilibrium is reached. The spontaneous emission towards a random direction can be described with the random walk model, where during a time t the mean number of photons $N = R_{sc} t$ scattered by an atom will result in a

mean displacement proportional to \sqrt{N} along a certain direction. Thus, the mean square velocity along the z -axis will increase according to

$$\bar{v}_z^2 = (1 + \eta) R_{\text{sc}} t v_{\text{rec}}^2, \quad (2.11)$$

and also the mean square momentum is given by [21, 22]

$$\bar{p}_z^2 = 2 D_p t = (\hbar k)^2 (1 + \eta) R_{\text{sc}} t, \quad (2.12)$$

where D_p is the *momentum diffusion coefficient*. In the factor $(1 + \eta)$ of the diffusion coefficient the unity contribution comes from the fluctuations in the number of the absorbed photons, which results in fluctuations in the velocity spread along the axis of the cooling beam. The contribution of the term proportional to η is the recoil from the spontaneously emitted photons towards a random direction. The value of η assuming isotropic emission is $\eta = 1/3$ along one axis. Since the cooling process occurs along three orthogonal axes, for the molasses technique the contribution is three times larger, thus $\eta = 1$. Also, since a pair of beams is employed for each axis, the overall factor $(1 + \eta)$ is twice as large.

For the two-level atom model, we can obtain the equilibrium temperature by equating the rate of change in the kinetic energy due to cooling by the molasses force with the rate of change in the kinetic energy due to the heating caused by the atom diffusion. At equilibrium, one can write [23]:

$$\frac{1}{2} M v_{\text{rec}}^2 2(1 + \eta) R_{\text{sc}} - \alpha \bar{v}_z^2 = 0. \quad (2.13)$$

The first term on the left is the rate of change in the kinetic energy due to the recoil, which is proportional to the rate of change of the square momentum $d\bar{p}_z^2/dt$. The second term is the rate of change in the kinetic energy due to the molasses cooling:

$$\frac{1}{2} M \frac{d}{dt} (v_z^2) = M v_z \frac{dv_z}{dt} = v_z F_{\text{molasses}} = -\alpha v_z^2. \quad (2.14)$$

From Eq. 2.13, the mean square velocity along the z -axis at equilibrium can be written as

$$\bar{v}_z^2 = \frac{2 M R_{\text{sc}} v_{\text{rec}}^2}{\alpha}. \quad (2.15)$$

From the relation $k_B T/2 = m \bar{v}_z^2/2$ (equipartition theorem), the equilibrium temperature is given by [21]

$$k_B T = -\frac{\hbar \Gamma^2}{8 \delta} \left[1 + \frac{I}{I_s} + \left(\frac{2\delta}{\Gamma} \right)^2 \right]. \quad (2.16)$$

For $I \ll I_s$, the previous function of $x = -\delta/\Gamma$ at the minimum $\delta = -2\Gamma$ gives

$$k_B T_D = \frac{\hbar \Gamma}{2}. \quad (2.17)$$

The above theoretical result is called the *Doppler cooling limit* and it is $140 \mu K$ for rubidium and $240 \mu K$ for sodium. The Doppler limit is the minimum expected temperature within the optical molasses technique resulting from the above treatment, where only the scattering of photons from the six laser beams has been considered. More subtle mechanisms involving the M_F sub-levels in the structure of the two-level atom result in temperatures below the Doppler limit. The sub-Doppler cooling mechanism has been given two equivalent explanations [18, 19], and predicts a limit down to the recoil energy $k_B T = \hbar^2 k^2 / M$, known as the *recoil limit*. The recoil limit is never reached in a MOT, because the external magnetic fields that perturb the M_F states of the atom need to be controlled to a precision of the recoil energy, which is 10 times less than the energy in the magnetic field of the earth. Typically, temperatures of at least one order of magnitude below the Doppler limit are reached in a MOT.

2.2 Quadrupole magnetic field

As explained in the previous section, the radiative force successfully cools down atoms, but it is not sufficient to trap atoms. As the velocity of the atoms tends to zero, the force itself tends to zero, and the atoms can drift away from the cooling region at the intersection of the three pairs of laser beams. The trapping of the atoms can be achieved by the addition of a magnetic field, which makes the force position dependent.

For that purpose a quadrupole magnetic field is used in combination with three circularly polarized pairs of laser beams. A quadrupole magnetic field is created by a pair of identical coils in anti-Helmholtz configuration, i.e. with currents running opposite to each other. The created magnetic field has zero field in the center and is increasing towards all directions linearly for small displacements from the center. The anti-Helmholtz configuration has been first developed by W. Paul for the confinement of neutrons [24] and has been later used for the magnetostatic trapping of neutral atoms using high gradients [?]. Contrary to the magnetostatic trapping of neutral atoms, the magnetic field used in combination with the optical molasses technique has low gradient and is not able to confine atoms by itself. It provides only with a position dependence to the radiation force, which is essential for the trapping to occur, while it is the radiation force that is confining the atoms.

The magnetic field generated by a pair of anti-Helmholtz coils has a cylindrical symmetry with zero field in the center. The field near the center is increasing linearly described by the equations [25]:

$$\begin{aligned} B_z &= 2 b z \\ B_r &= -b \rho, \end{aligned} \tag{2.18}$$

where z is the axis of symmetry and ρ is the radial coordinate. The gradient b near the center of the magnetic field at $z = 0$ is given by [26]:

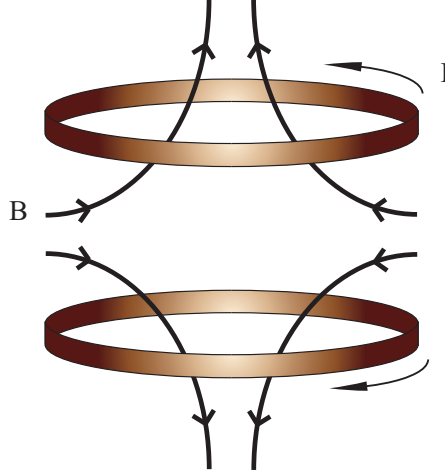


Figure 2.3: Magnetic field lines for the quadrupole magnetic field. The magnetic fields created by the two coils cancel out in the center resulting in $B = 0$. The coils have identical structure, and their currents are equal though running in opposite directions.

$$b = \frac{3}{2} \mu_0 I \frac{a R^2}{(a^2 + R^2)^{5/2}}, \quad (2.19)$$

where R is the radius of the coils, $2a$ is the separation distance of the coils and μ_0 is the vacuum permeability. The current I is equal for the two coils and it is running in opposite directions for the two coils in anti-Helmholtz configuration. The quadrupole magnetic field lines are shown on Fig. 2.3. The profile of the quadrupole magnetic field along the z -axis ($\rho = 0$) is shown on Fig. 2.4.

2.2.1 Atoms in the Magnetic Potential

The potential energy of an atom with magnetic dipole moment $\vec{\mu}$ in the applied external magnetic field is given by

$$U = -\vec{\mu} \cdot \vec{B}. \quad (2.20)$$

We consider an atom in the state $|J I F m_F\rangle$. In the presence of a magnetic field due to the Zeeman effect the energy levels are split with a corresponding Zeeman energy of

$$U = g_F m_F \mu_B B, \quad (2.21)$$

where μ_B is the Bohr magneton and F is the total angular momentum with $m_F = -F, \dots, -1, 0, 1, \dots, F$. The Landé g-factor g_F is a function of the angular momentum quantum numbers of the atom [20]

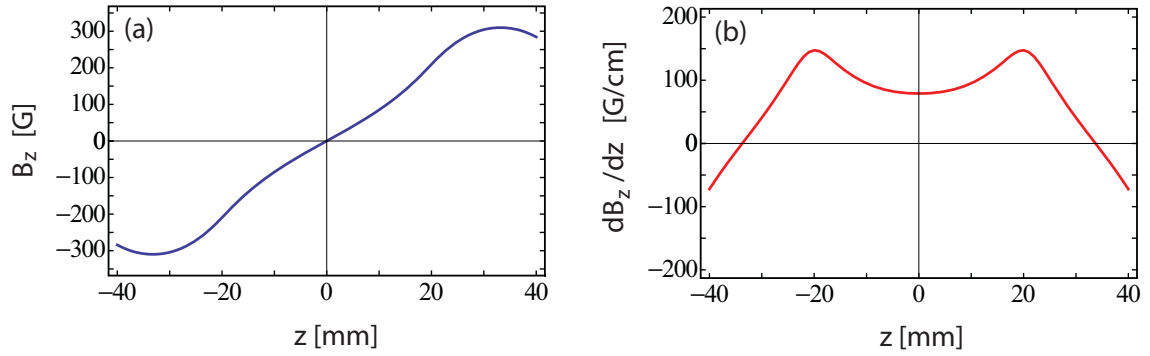


Figure 2.4: Simulated quadrupole magnetic field profile for the parameters of the setup discussed in Chapter 4. (a) Magnetic field along the z -axis ($\rho = 0$). The magnetic field is zero at the center, and it is increasing linearly for small displacements from the center. (b) Magnetic field gradient along the z -axis. The gradient at the center is effectively constant and linear in the region of the confinement of the atoms, which is of the order of $100 \mu\text{m}$.

$$g_F = \left[1 + \frac{J(J+1) + S(S+1) - L(L+1)}{2J(J+1)} \right] \left[\frac{F(F+1) + J(J+1) - I(I+1)}{2F(F+1)} \right], \quad (2.22)$$

where S , L and I the electron spin, orbital angular momentum and nuclear spin quantum numbers respectively. In addition, $J = L + S$ and $F = J + I$.

For the cooling and trapping of rubidium 87 (nuclear spin $I = 3/2$) in our experiments we use the closed transition $5^2S_{1/2} \rightarrow 5^2P_{3/2}$, as discussed in Chapter 4, with quantum numbers $F = 2$ for the ground state and $F' = 3$ for the excited state. The Zeeman shift between two states is proportional to $g'_F m'_F - g_F m_F$. For ^{87}Rb and the transition between the states $F = 2$, $m_F = 2$ and $F' = 3$, $m'_F = 3$ it is $g'_F m'_F - g_F m_F = 1$, as is the case with most of the alkali atoms and the transitions used in cold atomic experiments.

In the presence of an external magnetic field the atomic energy level are perturbed, and the Zeeman energy given in Eq. 2.21 depends directly on the magnitude of the magnetic field B . For an inhomogeneous magnetic field that varies in space, the atomic energy levels experience a Zeeman shift that is space dependent.

2.2.2 The Magneto-Optical Trap

The principle of the magneto-optical trap (MOT) is based on the imbalance created to the scattering force by the presence of a quadrupole magnetic field, which gives a spatial dependence to the force. The center of the quadrupole field is placed so that it coincides with the crossing point of the three pairs of beams used for laser cooling.

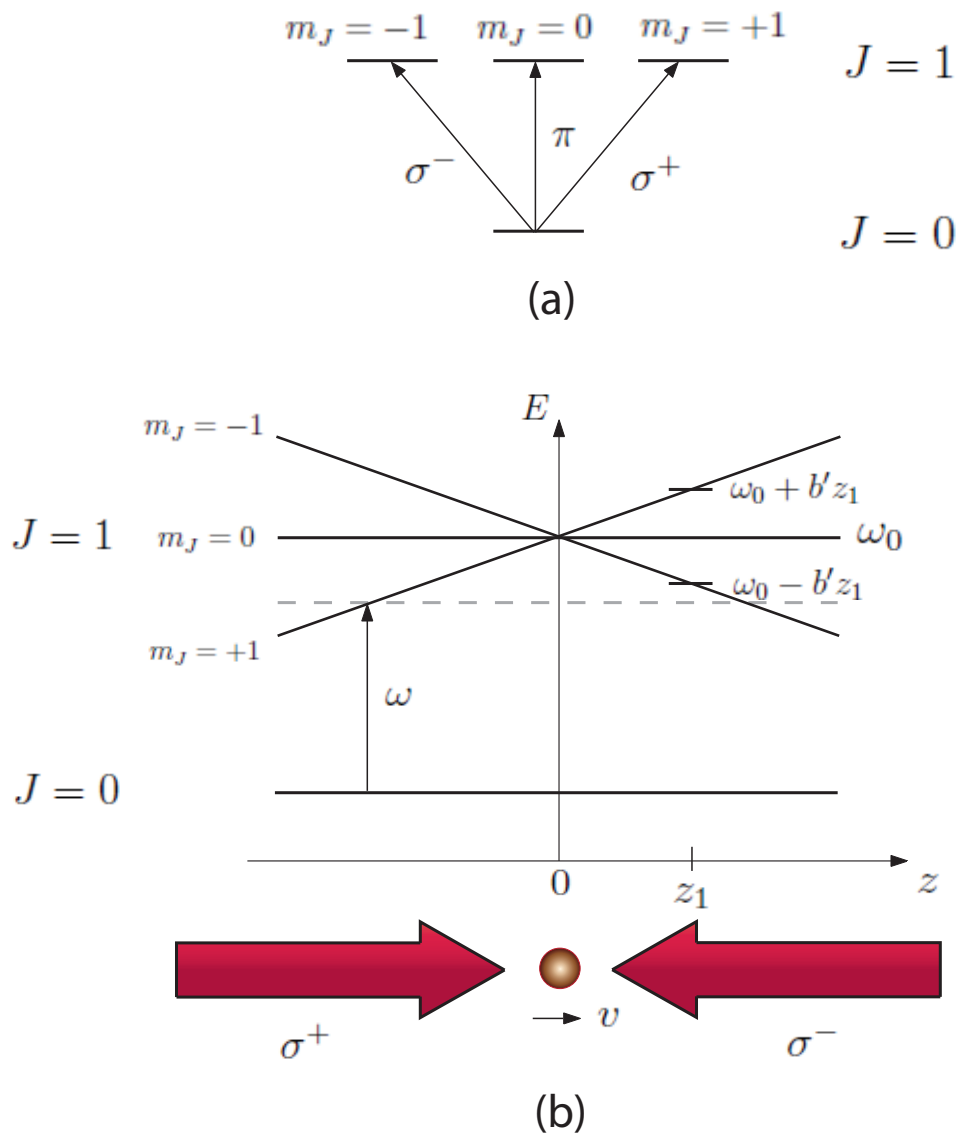


Figure 2.5: The Zeeman effect on the $J = 0 \rightarrow J = 1$ transition gives a space dependence to the scattering force. (a) In the presence of a magnetic field polarized light of π , σ^+ and σ^- polarization couples with the $m_J = 0$, $m_J = +1$ and $m_J = -1$ Zeeman sub-levels respectively. (b) The atom at position $z = z_1$ moving towards $z > 0$ sees the beam propagating opposite to its direction as being closer to resonance than the beam propagating along the same direction with the atom. Thus, the atom absorbs more photons from the opposite beam and feels a net radiative force that is pushing the atom back to the center ($z = 0$).

We consider the simple case of a $J = 0 \rightarrow J = 1$ transition. The quadrupole magnetic field has $B = 0$ in the center, and close to the center the gradient is linear towards all direction. The Zeeman effect causes the three sub-levels $m_J = 0, \pm 1$ of the $J = 1$ level to vary linearly with the position of the atom relative to the center.

We consider the one-dimensional model of the scattering force of two counter-propagating laser beams with the addition of the quadrupole magnetic field. The energy of the magnetic sub-levels along z -axis is shown in Fig. 2.5. The counter-propagating laser beams have a circular polarization in addition to being red-detuned. The laser beams are circularly polarized in such a way with respect to the magnetic field, so that an atom moving along the z -axis sees the beam propagating with the same direction as having σ^+ polarization and the beam propagating with the opposite direction as having σ^- polarization. For an atom at rest in the center ($z = 0$), where there is no magnetic field, the atom sees both beams equally detuned and there is zero mean radiative force. If the atom moves towards the right side ($z > 0$), it will see the beam propagating opposite to the direction of the atom being closer to resonance, as the σ^- polarization of the beam is coupling with the Zeeman energy of the $m_J = -1$ sub-level. The beam propagating along the direction of the atom, which couples with the $m_J = +1$ sub-level, is further from resonance. Consequently, the atom absorbs more photons from the counter-propagating beam and feels a net radiative force that is restoring the atom back to the center $z = 0$. The same argument can be inverted for the motion of the atom towards the left side ($z < 0$).

The effective detuning given in Eq. (2.4) is modified by the Zeeman shift according to

$$\delta = (\omega - \omega_0) - \vec{k} \cdot \vec{v} \pm \mu_B bz / \hbar, \quad (2.23)$$

where b is the magnetic field gradient close to the center. The Zeeman shift $\mu_B B / \hbar$ is positive (blue) for the beam propagating along the same direction with the atom and negative (red) for the beam propagating opposite to the atom. The force in Eq. 2.6 modified by the Zeeman shift can be written as

$$F_{\text{MOT}} = F_{\text{scatt}}(\omega - \omega_0 - kv - b'z) - F_{\text{scatt}}(\omega - \omega_0 + kv + b'z), \quad (2.24)$$

where we have substituted $b' = \mu_B bz / \hbar$, and b is the linear gradient near the center $z = 0$. Assuming low velocities $kv \ll \Gamma$ and a small Zeeman shift $\mu_B bz / \hbar \ll \Gamma$, the denominator in Eq. (2.3) can be expanded so that one can write Eq. (2.25) in the form [23]

$$F_{\text{MOT}} = -\alpha v - \kappa z. \quad (2.25)$$

The first term is the damping force with damping coefficient α . The second term, which arises from the Zeeman effect, leads to a restoring force with spring constant κ .

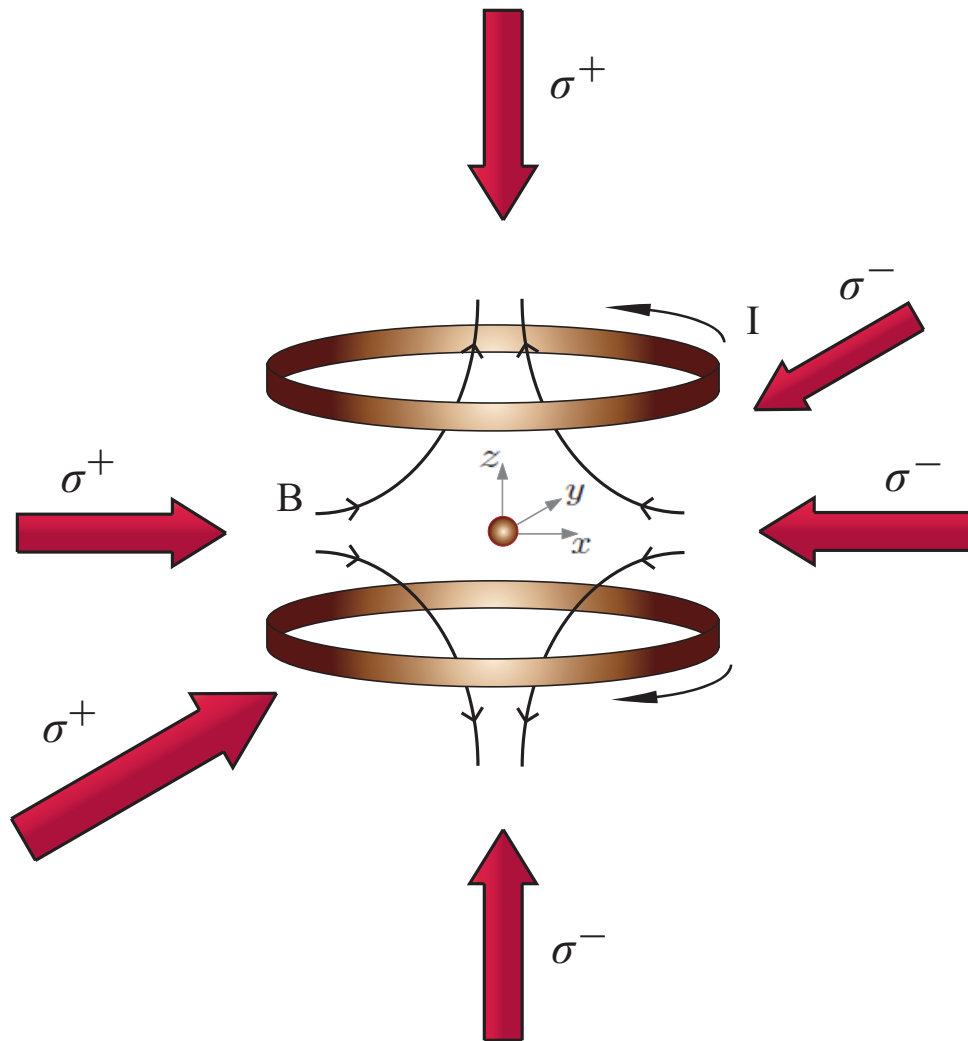


Figure 2.6: Schematic of the magneto-optical trap. The MOT consists of a pair of anti-Helmholtz coils, whose center coincides with the intersection of three pairs of counter-propagating beams with circular polarization. The polarization of the beams is prepared in such a way, so that an atom moving for example towards $x > 0$ sees the beam propagating opposite to it along the x -axis as having σ^- and the beam propagating in the same direction with the atom as having σ^+ . The same applies for the y -axis. For the z -axis, the polarization of the beams needs to be inverted with respect to polarization of the beams on the xy -plane. An atom moving towards $z > 0$ sees the beam propagating opposite to it as having σ^+ and the beam propagating in the same direction with the atom as having σ^- . The inversion of polarization between the beams on the xy -plane and the beams on the z -axis is required, because the direction of the magnetic field lines along the z -axis is opposite to the direction of the magnetic lines on the xy -plane.

The one-dimensional argument discussed above can be generalized to the three dimensions for the trapping of atoms in space for the actual magneto-optical trap. The force in three dimensions can be written as

$$\vec{F}_{\text{MOT}} = -\alpha\vec{v} - \kappa\vec{r}. \quad (2.26)$$

Atoms that enter the trapping volume of the intersecting beams are damped in an effective harmonic potential and the restoring force is gathering the atoms to the center, thus leading to the efficient trapping of atoms in the MOT. Figure 2.6 shows the magneto-optical trap configuration for trapping atoms in real space.

We note that the approach of considering a simple $J = 0 \rightarrow J = 1$ transition applies to the more general case of the $|F m_F\rangle \rightarrow |F' m'_F\rangle$ hyperfine transitions used in cold atom experiments. The Zeeman energy is the energy between the m_F sub-levels and it is given by $(g'_F m'_F - g_F m_F)\mu_B B$. Since $(g'_F m'_F - g_F m_F) \simeq 1$ for many of the transitions used in laser cooling, the discussion above about the Zeeman shift to the scattering force applies to the more general case.

2.3 Loading of Atoms into the Trap

In cold atom experiments, the MOT is loaded continuously from the background atomic vapor within a vacuum chamber. The rate at which atoms from the background vapor are captured in the MOT is balanced by the losses due to collisions with the background gas. Collisions of trapped atoms with atoms from the background gas is the main loss mechanism in the MOT, which results in the ejecting of one trapped atom. For the loading of the MOT, one can formulate the following rate equation

$$\frac{dN(t)}{dt} = R - \frac{N(t)}{\tau}, \quad (2.27)$$

where N is the number of atoms in the trap, R is the loading rate, the useful influx of atoms in the trap, and τ is the loading time constant determined by losses due to collisions with the background gas.

In our experiments we use ^{87}Rb atoms for trapping, and apart from the background gases untrapped rubidium atoms are also present in the vacuum chamber. Assuming the rate of collisions with background rubidium atoms is negligible compared to the rate of collisions with non-rubidium atoms [27], the collision associated losses are mainly due to collisions of the trapped atoms with the atoms from the background gases, and the loss rate can be written as

$$\frac{1}{\tau} = n_b \sigma \bar{v}, \quad (2.28)$$

where n_b is the density of the background gases, σ is the collisional scattering cross section and $\bar{v} = (2k_B T/M)^{1/2}$ is the most probable velocity for the gas in the background.

For the atoms at velocities lower than the capture velocity v_c of the trap, assuming that the background rubidium vapor has a thermal distribution, and also assuming that all atoms that enter the trapping region with v_c are captured, one can calculate the capture rate R from kinetic theory [27–29] as

$$R = \frac{2}{\pi^2} n_{\text{Rb}} A \frac{v_c^4}{\bar{v}^3}, \quad (2.29)$$

where n_{Rb} is the rubidium density, \bar{v} is the thermal velocity for rubidium and $A = 3\pi d^2/2$ is the effective trapping area. For the effective trapping area a uniform circular distribution has been assumed with diameter d equal to the stopping distance in Eq. (2.10). The solution to Eq. (2.27) is an exponential growth in the number of trapped atoms

$$N = N_s (1 - e^{-t/\tau}) \quad (2.30)$$

with $N_s = R\tau$ the steady-state number of atoms. It is possible to observe such loading curves according to the solution of Eq. (2.30) by collecting the fluorescence emitted by the atoms in the trap due to absorption and re-emission of the light from the trapping beams. During such measurements, we use a single-photon counting avalanche photo-diode (APD) to collect the fluorescence emitted by atoms in the trap. A theoretical estimation of the number of atoms N from the optical power P from fluorescence detected with the APD is provided by the following expression:

$$P = \frac{hc}{\lambda} \frac{\Omega}{4\pi} N R_{\text{sc}}, \quad (2.31)$$

where Ω is the solid angle subtended by the collecting lens, hc/λ is the photon energy, and R_{sc} is the photon scattering rate given in Eq. (2.2) with I the total intensity of the six trapping beams.

Figure 2.7 shows a typical curve of the loading process detected with the APD. The MOT trapping beams are turned on at time $t = 0$. By fitting Eq. (2.30) to the signal of the APD we are able to calculate the loading time constant equal to $\tau \simeq 13$ s. The avalanche photo-diode has been calibrated down to the fluorescence level of a single atom (as described in Chapter 5), which enables us to directly translate the signal from the APD to the number of atoms. From the number of atoms at the steady state $N_s = 315$, we calculate the capture rate at times near $t = 0$ equal to $R = N_s/\tau \simeq 25$ at./s.

The steady-state number of atoms can be written using Eq. (2.29) and Eq. (2.28) in the following form:

$$N_s \sim \frac{n_{\text{Rb}}}{n_b} \frac{d^2}{\sigma} \left(\frac{v_c}{\bar{v}} \right)^4. \quad (2.32)$$

As one can observe from the previous expression, the steady-state number of atoms is linearly dependent to the ratio of the background rubidium density to the total background density n_{Rb}/n_b . The background rubidium pressure $P_{\text{Rb}} = n_{\text{Rb}} k_B T$ can be calculated by substituting n_{Rb} from Eq. (2.29) as

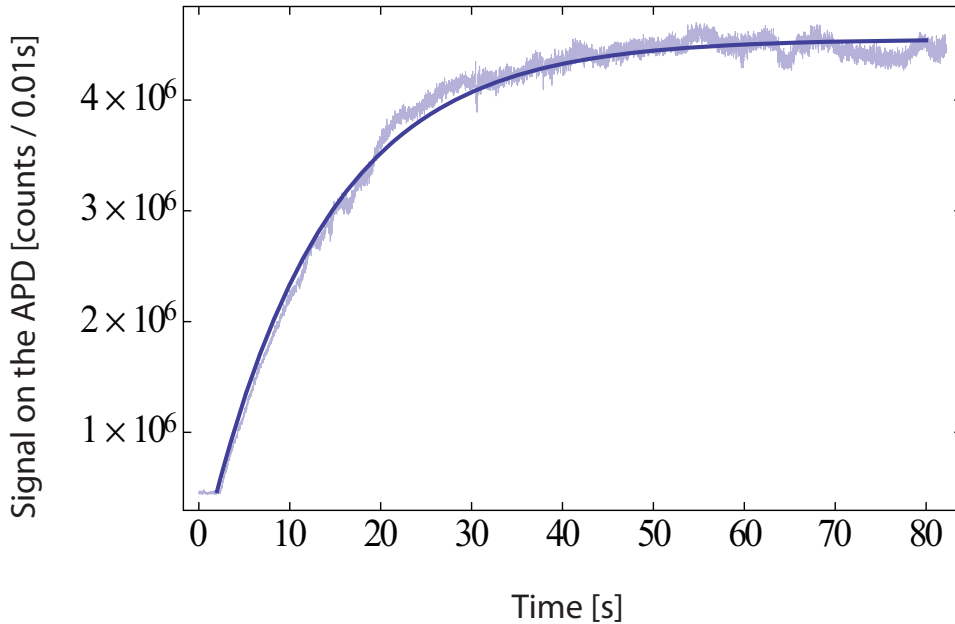


Figure 2.7: Loading process of the MOT. The loading process is observed by collecting the fluorescence emitted by the atoms using an avalanche photo-diode (APD). At time $t = 0$ the trapping beams are turned on. Equation (2.30) is fitted to the signal giving a loading time constant of $\tau = 13$ s.

$$P_{\text{Rb}} = \frac{R \bar{v}^3}{\pi^2 A v_c^4} k_B T. \quad (2.33)$$

For our trap parameters, $d = 2.1$ mm and $v_c = 20$ m/s, resulting in a rubidium pressure of $P_{\text{Rb}} \simeq 1.4 \times 10^{-14}$ mbar. The low rubidium pressure in the vacuum chamber results in a small steady-state atom number N_s , which is helpful for creating a low atom number MOT with the aim to observe low atom numbers down to single atoms.

2.4 Collisional losses in the MOT

2.4.1 Collisions with the background gases

The most significant of the loss procedures in the MOT is elastic collisions with room-temperature background atoms. One hot background atom that collides with a trapped rubidium atom imparts momentum to the atom up. This can lead to the trapped atom being ejected from the trap, thus this loss mechanism results in the loss of one atom for each collision. The background gas collisions, the main loss mechanism in the MOT, has been included in the description of the loading procedure of the MOT in the previous section (Sec. 2.3).

The collision loss rate due to collisions with the background gases is occurring at a rate αn_b (Eq. (2.28)) linear to the background gas density n_b . This expression is often merged into one constant $\gamma = 1/\tau$, where τ is the loading time constant. The background gases consists of residual vacuum gases and of rubidium vapor in the cell at room temperature. The most common residual gases are H and CO , which are the main diffusion products from the grain boundaries in stainless steel, and also N_2 . Helium could diffuse through the steel and glass although the abundance of He in the atmosphere is negligible. The loss rate is proportional to both the density of the residual gases and the density of rubidium in the background gases. However, the pressure of the rubidium vapor (untrapped rubidium in the glass cell) was found several orders of magnitude ($\sim 10^{-14}$ mbar) lower than the overall background pressure ($\sim 10^{-11}$ mbar), thus the residual gases have the major contribution on hot background collisions.

2.4.2 Light-assisted collisions in the trap

The second most significant loss mechanism in the MOT is inelastic collisions between two trapped particles, which occur due to the change of the energy of the internal state of the particles in the presence of a light field. This internal energy in turn can be converted in kinetic energy and result in the two colliding atoms leaving the trap. The light-assisted loss mechanism is induced by the light used for cooling and it is linear in the light intensity for $I \leq I_s$. This loss mechanism is characterized by the loss of two atoms per collision.

Two alkali atoms in close proximity are affected by their molecular potentials. In the case of trapping of ^{87}Rb , the transition used for cooling is $5^2S_{1/2} \rightarrow 5^2P_{3/2}$. Atoms in the trap undergo repeatedly many transition cycles of the cooling transition. Two atoms in the trap in close proximity with each other are likely to undergo an optical transition, that will couple to the $S + P_{3/2}$ quasi-molecule potential curve. The red-detuned light couples with the attracting branch of the $S + P_{3/2}$ potential near the "Condon" point (R_C). The quasi-molecule falls into the attractive part of the curve, and the two atoms are accelerated towards each other. Before the collision occurs though, the atom that was in the P state most likely relaxes back to the S state by spontaneous emission. Since the atom is in the attracting part of the potential curve, the photon that is spontaneously emitted is more red-detuned than the initially absorbed one at R_C . This absorption-emission cycle is repeated several times before the atoms eventually collide. The difference in energy between the absorbed and emitted photons is transferred as kinetic energy to the atoms in the occurring collision, leading to the thermalization of the two atoms. This in turn may result in the two atoms being expelled from the trap. This process is known as *Radiative Escape* (RE), and it is the process that contributes mainly to the two-body collision losses. A second process that contributes to the two-body losses is *Fine-Structure Changing Collisions* (FCC). For two atoms at close range on the $S + P_{3/2}$ potential curve during the collision adiabaticity is not maintained, and the quasi-molecule falls into the lower energy state of $S + P_{1/2}$. The change

of the internal energy is shared as kinetic energy equally among the two atoms. A detailed overview of cold collisions can be found in [30].

The two-body loss rate due to ultracold collisions in each position in the trap is $\beta n^2(\vec{r}, t)$, where β is the two-body loss rate coefficient and $n(\vec{r}, t)$ the density distribution of the trapped atom cloud. Taking into account the loss rate due to two-body collisions in the trap, Eq. (2.27) can be written as [31]

$$\frac{dN(t)}{dt} = R - \gamma N(t) - \beta \int n^2(\vec{r}) d\vec{r}, \quad (2.34)$$

where $\gamma = 1/\tau$ the collision rate with hot background particles. Similar equation to (2.34) can be written for the atom density n . The background collisions term is linear in the atom density $n(\vec{r})$ and the two-body loss term is proportional to $n^2(\vec{r})$.

When the MOT is loaded past the *radiation trapping limit*, there is no further increase in the density occurring [32, 33], because further loading of atoms results in an increase in the volume, so that the density stays constant. Towards the end of the transient, we consider being at the radiation trapping limit; the density of the trapped atoms is approximated by $n(\vec{r}, t) = n_c$, where n_c is the constant atomic density for certain trapping parameters. The loss in atoms due to binary intra-trap collisions is becoming to have an effect at higher atom densities. At small atom numbers, the contribution of the collision rates is small, and the approximation of the density with a constant is still valid [31]. Equation (2.34) simplifies to

$$\frac{dN}{dt} = R - (\gamma + \beta n_c) N. \quad (2.35)$$

The solution of this equation is an exponential given by

$$N = N_0 (1 - e^{-(\gamma + \beta n_c)t}). \quad (2.36)$$

The exponential of the previous equation is fitted to end part of the loading curve of the MOT shown on Fig. 2.7, to extract the total collision rate $\gamma + \beta n_c$.

The density distribution of the atom cloud in the trap follows a Gaussian sphere as expected for the atoms having a Maxwell-Boltzmann velocity distribution in a harmonic potential as

$$n(\vec{r}) = n_0 e^{-(\vec{r}/\sqrt{2}\sigma)^2}. \quad (2.37)$$

The atom cloud having a volume of $V = \int_0^\infty (n(\vec{r})/n(0)) d^3r = \pi^{3/2} \sigma^3$, we find for the trapping parameters of the experiment the constant density at a fully loaded MOT equal to $n_c = 6.1 \times 10^{10} \text{ cm}^{-3}$. Thus, by fitting the end part of the loading curve (> 95% of the transient), we extract the value of the two-body collision rate $\beta \simeq 3.3 \times 10^{-12} \text{ cm}^3/\text{s}$. This measurement of the two-body collision rate is in good agreement with measurements of β in a *Rb* MOT found in [34], where it is $\beta \simeq 2 \times 10^{-12} \text{ cm}^3/\text{s}$ for similar trapping parameters to our experiment.

In this experiments, where the aim is to obtain low atom-number clouds, a fully loaded MOT contains a number of atoms of $\sim 10^3$. The background collisions loss mechanism and the two-body loss mechanism, which depend on the atom density

$n(\vec{r})$ and on the square of the density $n^2(\vec{r})$ respectively, set an upper limit to the achieved density and atom number in the trap [35].

2.4.3 The lifetime of the MOT

The MOT that has been described so far is loaded from a constant background rubidium pressure. As a means to insert rubidium atoms in the experimental cell we are using a getter source. A getter source is a commercially available dispenser (described in Chapter 4), that is enclosed within the vacuum chamber and emits rubidium atoms when run with current. We run the dispenser for a short time, which results in that rubidium atoms are released in the cell. At the same time rubidium is pumped out by the vacuum pumps. This results, after the transient has settled after a few minutes, in a constant rubidium pressure in the cell.

In a fully loaded MOT, the maximum (steady-state) number of atoms N_s depends for given trap parameters on the rubidium partial pressure and the overall background pressure. When the MOT steady-state number of atoms has been reached (Fig. 2.7), there is a balance between capturing atoms and losing atoms to collisions. There is no decaying of the MOT taking place afterwards because the MOT is being loaded constantly from the constant background rubidium pressure.

In order to observe a decaying process in the number of atoms, we increase the rubidium partial pressure for a short time by running the dispensers at a higher current. The increase in rubidium pressure in the cell perturbs the equilibrium of a fully loaded MOT and has as a result a higher capture rate R' than before, leading to an increase in the maximum number of trapped atoms. The MOT in this case is loaded from the additional flux of atoms from the getter source. When the source is turned off, the atomic influx is ceased, and R' is omitted in Eq. 2.34, which becomes

$$\frac{dN(t)}{dt} = -\gamma N(t) - \beta \int n^2(\vec{r}) d\vec{r}. \quad (2.38)$$

The two-body loss mechanism is negligible compared to background gas collisions for relative high background pressures, and it becomes significant over background collision losses for pressures in the range of high-vacuum, which is the case for this experiment. Furthermore, the loading curve of the MOT can be still approximated very well with an exponential (Eq. 2.36), despite the non-linear term of intra-trap two-body collisions [36], while for the decay of the MOT the non-linear term gives decay curves that deviate strongly from being exponential.

In the case of low atom densities in the MOT, the intra-trap two-body losses become less significant compared to background gas collisions, and the decay process from the above equation is simplified to an exponential decay. In that case, the lifetime of the MOT is defined as the inverse of the time constant of the decay process. Furthermore, the time constant of the decay is independent of the steady-state population of the trap [37]. Considering collisions with the residual background gases (mostly H) and with untrapped rubidium atoms to be the most significant loss mechanism, the lifetime of the atoms in the trap is written as

$$\frac{1}{\tau} = n_b \sigma_b \bar{v}_b + n_{\text{Rb}} \sigma_{\text{Rb}} \bar{v}_{\text{Rb}} \quad (2.39)$$

where \bar{v} is the mean thermal velocity associated with the collisions ((240 m/s for ^{87}Rb and 2200 m/s for H at $T = 300$ K), n is the density of the background gas, $\sigma_b = 3.5 \times 10^{-14} \text{ cm}^2$ is the collisional cross section with the background atoms [37] and $\sigma_{\text{Rb}} = 3 \times 10^{-13} \text{ cm}^2$ is the collisional cross section with the untrapped rubidium atoms [37].

In the experiments of low atom number MOTs, where we are able to observe clouds of a few single atoms, we are interested in the time intervals τ_{on} of a single atom in the trap, rather than the lifetime τ of a fully loaded MOT. The time intervals τ_{on} of which a single atom stays in the trap before it is ejected follow an exponential distribution [15], analogously to the exponential decay for a fully loaded MOT. The effect of two-body collisions at the range of low atom numbers has been studied in [38], which results in the loss rate being modified due to two-body collisions as

$$\frac{1}{\tau_{\text{on}}} = n \sigma \bar{v} + \beta \frac{N-1}{V}, \quad (2.40)$$

where β is the two-body collision rate, V is the trapping volume, and $N = 0, 1, 2, \dots$ is the number of the individual atoms trapped in the MOT.

The times τ_c between two successive atoms entering the trap are also expected to follow an exponential distribution, since the loading of a large MOT occurs exponentially. Assuming that all atoms that enter the trapping region with v_c are captured, the mean time between two successive atoms entering the trap can be associated with the capture rate given in Eq. (2.29) as

$$\frac{1}{\tau_c} = R. \quad (2.41)$$

In order to create a low atom number MOT, we start with a fully loaded MOT at a constant background rubidium pressure and, by tuning the trap parameters, we reduce the capture rate R . For a typical low atom number MOT the capture rate R is $\sim 0.1 \text{ s}^{-1}$, which is much smaller than the capture rate of high atom number MOT. One way to reduce the capture rate, apart from having a low background rubidium pressure, is by decreasing the detuning δ . For a decrease in the detuning, the capture velocity $v_c = \pm\delta/k$ also decreases, which results in fewer atoms being, since R varies with v_c^4 . The capture rate can also be reduced by increasing the magnetic field gradient. For a higher magnetic field gradient, the Zeeman shift rises more rapidly from the trap center, and the atoms become resonant at a smaller distance from the center (Eq. (2.23)). The later results in decreasing the stopping distance d , which decreases the capture rate R . For this experiment in low atom number MOT magnetic field gradients of 50 G/cm are used, which is about 3 times larger than the gradients used in MOTs for trapping high atom numbers ($\sim 10^6$).

Chapter 3

Theory on Imaging Techniques

In cold atom experiments the imaging of the atomic sample is a fundamental part of the experiment for extracting information about the cold atomic sample. Absorption imaging has been extensively used in experiments of cold atomic samples and Bose-Einstein condensates (see for example [1]) as a tool to study the sample itself and extract information about its size, its temperature and the atom number [39], as well as for studying the physics involved with cold atoms such as squeezing and entanglement [7] and coherence phenomena of atom-wavepackets [40]. In the same scientific field, several other techniques based on the interaction of a probe beam with the atoms have been developed as an alternative to classical absorption imaging, such as Fourier-filtered imaging among other imaging techniques with two main goals being to image non-destructively and/or increase the sensitivity of the imaging.

In this chapter the theory of classical absorption imaging and Fourier-filtered imaging is discussed. Some other techniques are briefly discussed. The theoretical background of diffractive dark-ground imaging, a Fourier-filtering based technique, is presented.

3.1 Atom-light interactions

Imaging techniques such as absorption imaging and Fourier-filtered imaging involve light from a probe beam interacting with the atom cloud. The resulting light field, which is carrying the information of the atom cloud, is collected with a set of imaging optics and sent to a detector.

In the interaction of light with atoms, the atom cloud can be treated as an optical medium having a complex susceptibility. Thus, the light entering the optical medium will be absorbed and refracted. The absorption of photons and the phase-shift of the light are the main processes used to derive information about the atom cloud in imaging techniques involving a probe beam, such as absorption imaging and Fourier-filtered imaging.

For a weak probe light ($I \ll I_s$) with detuning δ from the optical transition, and for an atom cloud with density $n(x, y, z)$, the complex index of refraction for a two-level system can be written as [41]

$$\tilde{n} = 1 + \frac{\sigma_0 n \lambda}{4\pi} \left[-\frac{\frac{2\delta}{\Gamma}}{1 + \frac{4\delta^2}{\Gamma^2}} + i \frac{1}{1 + \frac{4\delta^2}{\Gamma^2}} \right], \quad (3.1)$$

where $\sigma_0 = 3\lambda^2/2\pi$ is the resonant cross-section, Γ the natural linewidth of the transition and λ the wavelength of the transition. Assuming the thin lens approximation for the atom cloud, we substitute the density of the cloud with the column density $n(x, y) = \int n(x, y, z) dz$. The probe light is attenuated and phase-shifted by the atoms, and the field can be written as

$$E = t E_0 e^{i\phi}. \quad (3.2)$$

The transmission coefficient t and the phase shift ϕ are given by

$$t = \exp\left(-\frac{n\sigma_0}{2} \frac{1}{1 + \frac{4\delta^2}{\Gamma^2}}\right), \quad (3.3)$$

$$\phi = -\frac{n\sigma_0}{2} \frac{\frac{2\delta}{\Gamma}}{1 + \frac{4\delta^2}{\Gamma^2}}. \quad (3.4)$$

The optical density D is given by the exponent of the transmission coefficient of the intensity $I = |E|^2/2$:

$$t^2 = \exp(-D). \quad (3.5)$$

Defining $D_0 = n\sigma_0$ as the resonant optical density, the off-resonant optical density can be written as

$$D = D_0 \frac{1}{1 + \frac{4\delta^2}{\Gamma^2}} = n\sigma, \quad (3.6)$$

where $\sigma = \sigma_0/(1 + (2\delta/\Gamma)^2)$ is the off-resonant cross-section.

3.2 Absorption imaging

Absorption imaging relies on illuminating the atoms with a weak probe beam and measuring the decrease in probe beam intensity on the CCD camera (Fig. (a)). Part of the light of the probe beam is absorbed by the atom cloud with density $n(x, y)$, which results in a decrease in intensity which varies in space. For absorption imaging, the light field E after absorption from the atom cloud is given directly from Eq. 3.2. The image on the CCD will show the spatial variation of the intensity $I(x, y) = |E(x, y)|^2/2$

In the regime of weak probe beam intensities, the intensity distribution $I(x, y)$ of the probe beam after being absorbed by the atoms is given by

$$I = \frac{1}{2}|E|^2 = I_0 t^2 = I_0 e^{-D}, \quad (3.7)$$

where $I_0 = E_0^2/2$ is the initial density profile of the probe beam before being absorbed by the atoms, and t^2 is related to the optical density D through Eq. 3.5.

To extract information about the atom cloud, one is interested in measuring the density $n(x, y)$ of the cloud, which is related to the optical density as

$$D(x, y) = \sigma n(x, y). \quad (3.8)$$

In the absorption imaging procedure, first an image is acquired with the intensity distribution $I(x, y)$ of the probe beam after absorption from the atoms. In order to extract the optical density D from Eq. 3.7, a second image with the initial intensity distribution $I_0(x, y)$ is required. The second image, called the reference image, is taken with the probe beam on in the absence of atoms. The absorption and the reference image need to be corrected for any stray light coming from sources other than the probe beam. For that purpose, a third image of the background light $I_{\text{bg}}(x, y)$ is taken with no atoms and the probe beam off.

$$D = -\ln(t^2) = -\ln \frac{I(x, y)}{I_0(x, y)} = -\ln \frac{I_{\text{atoms}}(x, y) - I_{\text{bg}}(x, y)}{I_{\text{ref}}(x, y) - I_{\text{bg}}(x, y)}. \quad (3.9)$$

The third image of the background light is subtracted from both the image with the absorption from the atoms and the reference image, before using them for the calculation of the optical density.

In experiments with large atom numbers, like for example in [42, 43], the optical density of the cloud for a resonant probe beam is of the order of 300, which is much greater than the maximum optical density ($D \simeq 10$) detectable by the CCD limited by its dynamic range. In order to extract quantitative information of such dense clouds using absorption imaging, one has to detune the probe beam off resonance to reduce the absorption signal. So far, absorption imaging has been treated considering a resonant probe beam. The index of refraction for the atom cloud interacting with a resonant probe beam has only an imaginary part, and thus the probe light is only attenuated by the atoms.

In the presence of an off-resonant probe, the refractive index has a non-zero real part, which is responsible for the phase shift imposed to the probe beam by the atom cloud. The atom cloud due to its curvature is considered to act like a lens [1], which refracts part of the probe light. The refraction of light from the atom cloud is known as the *lensing effect* and can result in systematic errors in the number of atoms measured with absorption imaging. The real part of Eq. 3.1 is given by

$$\text{Re}(\tilde{n}) = 1 - \frac{3n \lambda^3}{8\pi^2} \frac{2\delta/\Gamma}{1 + 4\delta^2/\Gamma^2}. \quad (3.10)$$

The previous equation shows that for $\delta < 0$ (red detuning) the real part of the refractive index is greater than one, and the atoms act as a converging lens. On the other hand, for $\delta > 0$ (blue detuning) the real part is less than one, and the atoms act as a diverging lens. The refracted light, unless it is all collected by the imaging optics, it leads to distortions of the image of the cloud. A spherical cloud with radius R and index of refraction n is acting as a lens with focal length $1/f = 2(\tilde{n} - 1)/R$

[44]. The phase shift ϕ of the light at wavelength λ passing through the center of the lens is $\phi = 4\pi R(\tilde{n} - 1)/\lambda$. By eliminating the term $(\tilde{n} - 1)$ the deflection half-angle due to refraction on the cloud of atoms with radius R and phase shift ϕ is given by

$$\theta = \tan^{-1} \left(\frac{R}{f} \right) \approx \frac{R}{f} = \frac{\phi}{\pi/2} \frac{\lambda}{4R}, \quad (3.11)$$

In the equation above, the second term is equal to the diffraction angle due to the finite size of the optics, and the ratio $\phi/(\pi/2)$ determines whether the deflection angle is greater or smaller than the diffraction limited angle $\lambda/(4R)$. The diffraction limited angle determines the smallest object of R that can be resolved within an imaging system. The diffracted light from the finite object at the diffraction limit is equal to the collection angle of the optics. For the deflection angle due to refraction this means that for phase shifts $\phi < \pi/2$ the refracted light is within the diffraction angle and it is collected by the imaging optics making quantitative absorption imaging possible. For greater phase shifts than $\phi \approx \pi/2$, the refraction angle exceeds the diffraction angle, which leads to deterioration of the images. Therefore, in the presence of refraction, the minimum radius R of an atom cloud that can be detected with quantitative absorption imaging is $\approx \phi/(\pi/2)$ times as large as in the diffraction limit.

That means that large atom clouds can still be measured using quantitative absorption imaging. For small dense clouds, one can use the time-of-flight technique. The atom cloud is released from the trap and left to expand for a some time, thus its density is decreased, before the absorption image is taken. Alternatively, one can apply dispersive imaging techniques, either dispersive dark-ground imaging [45] or phase-contrast imaging [46] (discussed in Section 3.3), which are periodic in the phase shift ϕ and do not saturate at large ϕ . Data processing analysis of a distorted image due to lensing has also been demonstrated [47].

3.3 Fourier-filtering techniques

Due to the interaction of the probe light with the atoms, part of the probe beam light is absorbed and refracted by the atom cloud. Absorption from a small object like the atom cloud causes diffraction in the probe light. Refraction on the atom cloud and diffraction due to absorption can be regarded as the coherent forward scattering of light on the atom cloud. The probe beam after passing through the atoms can be analyzed into two components, one containing the scattered part of the light and one the unscattered part of the light. The Fourier-filtering approach relies on separating spatially the two components of the scattered and the unscattered light. This is achieved by placing a filtering object at the center of the Fourier plane of the first imaging lens (Fig. 3.1(b), (c)). In the lowest order approximation, the unscattered component is considered to be a plane wave. Thus the unscattered component is focused by the first imaging lens at the Fourier plane of the lens, where it interacts with the filtering object. The part of the probe light that has been scattered by the

atom cloud is considered to diverge from a point source and is collimated by the first imaging lens. The collimated scattered component containing all the information about the atoms is not affected by the filtering object and it is focused on the image plane. Imaging methods employing the Fourier-filtering principle are commonly used in microscopy. Fritz Zernike has been awarded the Nobel prize in 1953 for introducing the phase-contrast imaging method in 1934 [2, 3].

3.3.1 Dispersive dark-ground imaging

Fourier-filtered based imaging techniques are performed by placing a filtering object at the Fourier plane of the first imaging lens. In the most simple case, the filtering object is an opaque object, that blocks the unscattered light component (Fig. (b)). The group of Ketterle in MIT, that first implemented this technique [45], have used a thin wire as an opaque object. In this method, the light of an off-resonant probe beam is refracted on the atom cloud. While the unrefracted component is blocked, the refracted light is not affected by the opaque object and forms a bright image on the camera on a darker background. Hence, the names "dispersive imaging" and "dark-ground imaging" were originally adopted. We refer to this method as *dispersive dark-ground imaging* to differentiate it from *diffractive dark-ground imaging*, where the light of a resonant probe beam is diffracted on the atom cloud.

This method was used to measure small dense Bose-Einstein condensates of a resonant optical density of 300. Absorption imaging is difficult to be applied on resonance at such high optical densities. Though the optical density is reduced off-resonance, large detunings result in a strong lensing effect. Deterioration to the images is avoided as long as refraction occurs within the diffraction angle due to the finite size of the object, which limits the smallest detectable size of the atom cloud (discussed in Sec. 3.2). Dispersive dark-ground makes use of the refracted light at an angle greater than the diffraction angle of the cloud to clearly image a small dense condensate.

The off-resonant probe beam after passing through the atoms is attenuated and phase shifted, and its light field can be separated into the two components containing the scattered and unscattered light. The transmitted light field E is given by

$$E = t E_0 e^{i\phi} = E_0 + E_r, \quad (3.12)$$

where E_r is the component of the refracted light, and E_0 is a plane wave that has not interacted with the atom cloud. Blocking the plane wave component results in the signal of the refractive dark-ground imaging:

$$\langle I_{\text{rdg}} \rangle = \frac{1}{2} |E_r|^2 = \frac{1}{2} |E - E_0|^2 = I_0 [1 + t^2 - 2t \cos \phi], \quad (3.13)$$

with $I_0 = |E_0|^2/2$ the intensity of the probe beam before scattering. At small ϕ the refractive dark-ground signal is quadratic in ϕ .

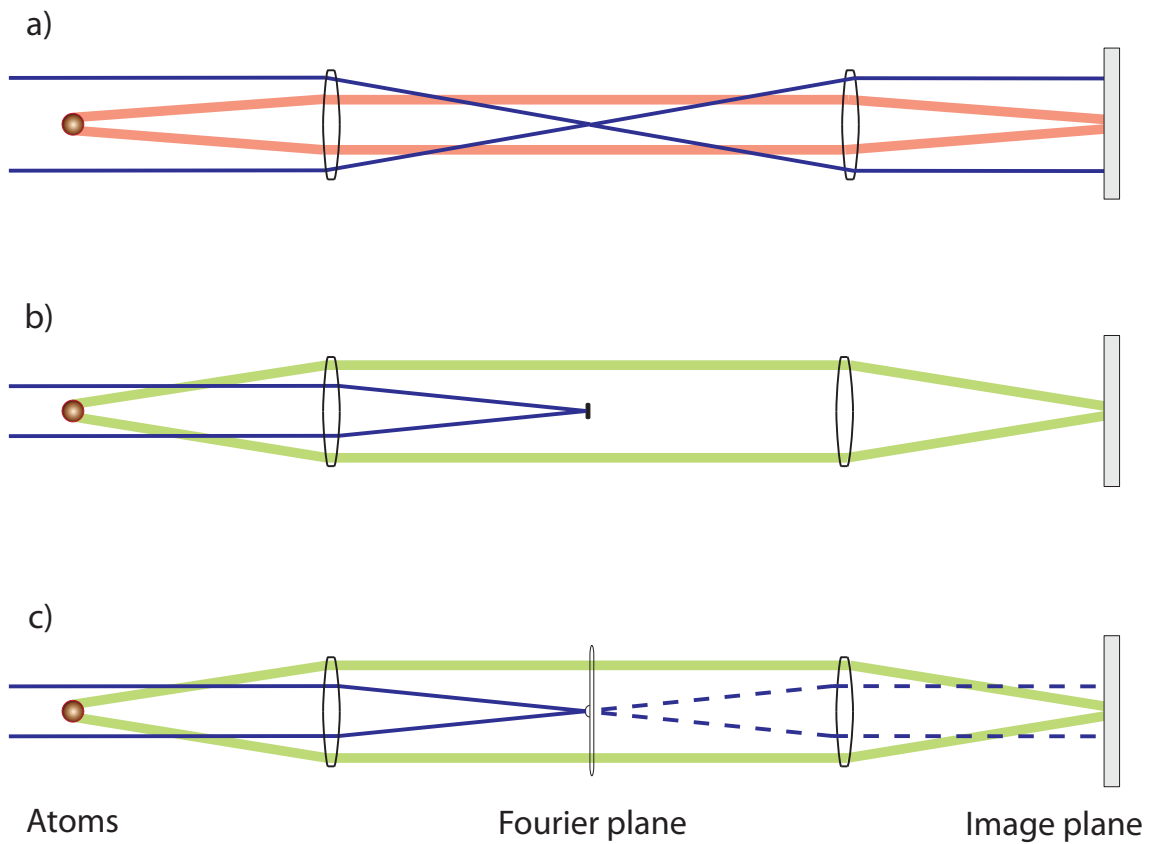


Figure 3.1: Schematics of the optical path for different imaging techniques. (a) *Absorption imaging*: The probe beam (blue) illuminates the atom cloud and the transmitted light is collected by the imaging optics. The absorbed light (pink), that is subtracted from the total field, appears on the image plane as a dimple on a brighter background, where the background originates from the unabsorbed probe light. (b) *Dispersive dark-ground imaging*: An off-resonant probe beam (blue) is phase-shifted by going through the atom cloud, which causes light to refract (green). The unscattered component is blocked with an opaque object at the Fourier plane of the first imaging lens, while the refracted light is focused on the image plane forming a bright spot on a darker background. (c) *Phase-contrast imaging*: Instead of an opaque object, a $\lambda/4$ waveplate is placed at the Fourier plane of the first imaging lens, which shifts the unscattered light E_0 by $\pm\pi/2$. The phase shifted unscattered light E_0 by 90° interferes with the refracted light E_r at the image plane forming a phase-contrast image.

3.3.2 Phase-contrast imaging

Phase-contrast imaging is based on the interference of the scattered and unscattered light components. The scattered light is due to refraction of an off-resonant imaging beam on the atom cloud, as in the refractive dark-ground imaging. Instead of blocking the unscattered component though, the unscattered light E_0 is phase shifted by $\pm\pi/2$ by a "phase plate", placed at the Fourier plane of the first imaging lens. The "phase plate" has a small bump or dip at the center resulting in a phase shift of $\pm\pi/2$, whereas it is elsewhere optically flat, so that the collimated refracted light passes through unaffected (Fig. 3.1(c)). The two light fields, the refracted light field E_r and the shifted unscattered light $E_0 e^{\pm i\pi/2}$ interfere at the image plane forming a phase-contrast image [1, 48].

By the interference of the two light fields, $E_r = E - E_0$ and $E_0 e^{\pm i\pi/2}$, the intensity at the image plane is

$$\begin{aligned} \langle I_{\text{pc}} \rangle &= \frac{1}{2} |E_r + E_0 e^{\pm i\pi/2}|^2 = \frac{1}{2} |E + E_0 (e^{\pm i\pi/2} - 1)|^2 \\ &= I_0 \left[t^2 + 2 - 2\sqrt{2}t \sin\left(\phi \pm \frac{\pi}{4}\right) \right], \end{aligned} \quad (3.14)$$

and for $\phi \ll 1$, the intensity

$$\langle I_{\text{pc}} \rangle \simeq I_0 [t^2 + 2 - 2t \pm 2t\phi] \quad (3.15)$$

is linear in ϕ .

Phase-contrast imaging was first introduced by M. R. Andrews and collaborators and was used to perform successive non-destructive measurements of Bose-Einstein condensates [49, 50].

A polarization phase-contrast technique has also been implemented for the detection of a Lithium BEC of atom number of 600 atoms [46]. The probe beam is linearly polarized with respect to a magnetic field. As it passes through the atoms, one component of the probe beam couples to the σ^+ optical transition and acquires a phase shift, while the other does not. The two components recombine and interfere with the use of a linear polarizer. The technique is performed far off-resonance where absorption on the atoms is negligible.

3.3.3 Other imaging techniques

Several other techniques have been developed that make use of scattering of light from an imaging beam onto the atom cloud, and detect either the change in intensity or in the phase.

Diffraction-contrast imaging

Diffraction-contrast imaging introduced in [51] solves the inverse problem of retrieving the structure of a cold atom cloud from a single diffraction image. An

off-resonant imaging beam is used to illuminate the atom cloud non-destructively, and a single diffraction pattern is recorded without the use of any optics. The optical density of the atom cloud is retrieved from the intensity of the diffraction pattern by solving the inverse problem of a propagating wave that has been attenuated and phase-shifted by the atom cloud.

Non-destructive spatial heterodyne imaging

While phase-contrast imaging can be considered as homodyne detection, where the unscattered light interferes with the scattered light, a heterodyne detection imaging technique has been demonstrated [52], where the imaging beam, that is phase shifted by the atoms, interferes with a second laser beam that has not interacted with the atoms. The interference of the imaging beam with the reference beam produces an interference pattern on the CCD, where the position of the fringes depends on the relative phase between the two laser beams and is distorted by the phase shift due to the atoms. The interference pattern is processed in software in order to retrieve the phase shift due to the atom cloud.

3.4 Diffractive dark-ground imaging

In our experiments of imaging small atom numbers at low optical densities we have applied a Fourier-filtering based method, which relies on the diffraction caused to a resonant probe beam by an atom cloud, called *Diffractive dark-ground imaging*. The imaging beam is tuned into resonance to have minimal phase shift by the atom cloud and to maximize the absorption, since we are interested in the detection of small signals. The atom cloud is strongly absorbing light from the resonant probe beam and can be considered as an opaque object much smaller in diameter than the profile of the beam. Figure 3.2 shows the principle of diffractive dark-ground imaging, which is similar to the principles of the Fourier-filtered techniques described elsewhere in this chapter.

3.4.1 The light field in diffraction dark-ground imaging

In diffractive dark-ground imaging (DDGI), the unscattered component of the imaging light is separated from the scattered component, where the scattering occurs due to diffraction of the light on an absorbing target. The unscattered component, that is focused by the first imaging lens, is blocked by an opaque disk (called a "dark spot") placed at the Fourier plane of the first imaging lens. The diffracted component of the light due to absorption by the atom cloud is transformed by the lens into a plane wave and remains unaffected by the dark spot. The diffracted component, which is essentially the light that contains the information from the atoms, is collected onto the CCD forming a bright spot on a darker background.

In the case of normal absorption imaging, the part of the imaging beam that has not been absorbed by the atoms is what mainly contributes to the background of the

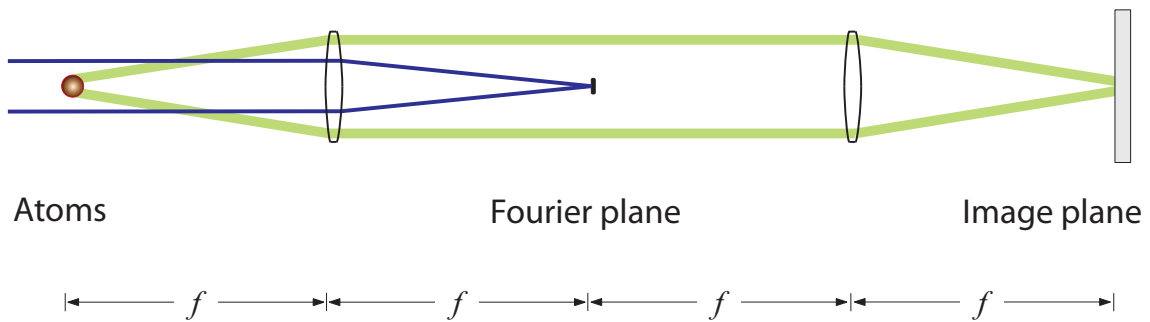


Figure 3.2: Schematic of the optical path for the *Diffractive dark-ground imaging* technique: A resonant probe beam (blue) is partially absorbed by the atom cloud, which causes light to diffract (green). The unscattered component is blocked with an opaque object ("dark spot") placed at the Fourier plane of the first imaging lens, while the diffracted light remains unaffected by the dark spot and it is focused on the image plane forming a bright spot on a darker background.

images. In the diffraction dark-ground imaging technique, the unaffected part of the imaging beam is blocked by the dark spot, which results in a low background level on the diffractive dark-ground images. The suppression of the background reduces the noise on the images and increases the sensitivity of the technique at low optical densities. To test the sensitivity of the technique, we have applied diffraction dark-ground imaging on a MOT and on a BEC setup at optical densities in the range of $D \simeq 10^{-2}$.

The intensity on the image plane for the diffraction dark-ground imaging can be derived in analogy to the refractive dark-ground imaging treatment of the light field in Sec. 3.3.1. The light field of the resonant probe beam after being absorbed by the atoms can be decomposed into an unscattered plane wave component E_0 and a light field component due to the absorption E_{abs} . The transmitted light field E follows a similar equation to Eq. 3.12 and it is given by

$$E = t E_0 = E_0 + E_{\text{abs}}, \quad (3.16)$$

where there is no phase shift ($\phi = 0$) to the light from the atoms, since the imaging beam is in resonance ($\text{Re}[\tilde{n}] \rightarrow 0$ for $\delta \rightarrow 0$). Blocking the plane wave component results in the signal of the diffractive dark-ground imaging:

$$\langle I_{\text{ddg}} \rangle = \frac{1}{2} |E_{\text{abs}}|^2 = \frac{1}{2} |E - E_0|^2 = I_0 (1 - t)^2, \quad (3.17)$$

with $I_0 = |E_0|^2/2$ the intensity of the probe beam before the absorption.

From Eq. 3.17 the CCD image intensity of diffractive dark-ground imaging is related to the transmission coefficient t , and thus the optical density of the atom cloud is derived from the images as

$$D = -\ln(t^2) = -\ln \left[\left(1 - \sqrt{\frac{I_{\text{ddg}}}{I_0}} \right)^2 \right], \quad (3.18)$$

The atom density (Eq. 3.6) is given by

$$n = -\frac{1}{\sigma} \ln \left[\left(1 - \sqrt{\frac{I_{\text{ddg}}}{I_0}} \right)^2 \right], \quad (3.19)$$

with $\sigma = \sigma_0 / (1 + (2\delta/\Gamma)^2)$ being the off-resonant cross-section for saturation parameter $s_0 = I/I_s \ll 1$. In our experiments, where we measure small atom clouds at low optical densities and we expect to have a small signal, we opt for in-resonance imaging ($\delta = 0$) and saturation intensities of $s_0 \geq 1$. In the general case taking saturation into account, the cross section is given by [53]

$$\sigma = \frac{\sigma_0}{(1 + s_0 + (2\delta/\Gamma)^2)}. \quad (3.20)$$

3.4.2 Fourier treatment of diffractive dark-ground imaging

In this section diffraction dark-ground imaging is analyzed using Fourier transform arguments. After the probe light has been absorbed by the atoms, the transmitted light field is collected by the first lens, which acts as a Fourier transformer, thus one can treat the effect of the filter on the light by taking the spatial Fourier transform at the Fourier plane of the first lens.

A general solution to the homogeneous electromagnetic wave equation in rectangular coordinates is formed as a superposition of all possible elementary plane wave solutions as [54]

$$E(x, y, z) = \iint E(k_x, k_y) e^{i(k_x x + k_y y)} e^{\pm iz \sqrt{k^2 - k_x^2 - k_y^2}} dk_x dk_y, \quad (3.21)$$

where each individual plane wave components is described explicitly by the exponentials, which are functions of the spatial wavenumbers (k_x, k_y) .

In the far-field the above equation may be evaluated as

$$E(r, \theta, \phi) = 2\pi i (k \cos \theta) \frac{e^{-ikr}}{r} E(k \sin \theta \cos \phi, k \sin \theta \sin \phi), \quad (3.22)$$

which shows that the field at a point (x, y, z) far from the source is proportional to the plane wave component (k_x, k_y, k_z) propagating in the direction of (x, y, z) with its plane tangent at the wavefront. Equivalently, the radiation pattern at a plane far from the source is the Fourier transform of the distribution of the source.

An input function $f(x, y)$ at the front focal plane of a lens can be described with a spectrum of plane waves corresponding to the Fourier transform $F(k_x, k_y)$ according to Eq. 3.22. For each plane wave propagating with a small angular deviation from the optical axis (paraxial approximation) the lens transforms each plane wave ideally

into a δ -function at the origin of the back focal plane (Fourier plane). Due to the finite size of the lens (diffraction), the image at the back focal plane is formed as a Point-spread function (PSF) characteristic of the impulse response of the system. For a circular aperture like the lens, the characteristic PSF is the *Airy function*, characterized by a central lobe at the origin of the Fourier plane and the higher frequency concentric rings originating from the fast transition at the edges of the aperture. For a point source (far field approximation) placed at the front focal plane of the lens the transformed field will have a single plane wave component in its spectral distribution and a spherical wavefront.

The optical setup used for diffractive dark-ground imaging (Fig. 3.2) is known as the $4f$ -correlator. Its principle is based on the fact that, an input function $f(x, y)$ placed on the left focal plane (input plane) of the first lens is correlated with the transmittance function $h(x, y)$ of the filter placed at the Fourier plane. The Fourier transform $F(k_x, k_y)$ of the input function formed at the Fourier plane is multiplied with the Fourier of the transmittance function of the filter giving a total transmission of $H(k_x, k_y) \cdot F(k_x, k_y)$. This product is Fourier transformed by the second lens, which gives at the focal plane on the right (output plane) the convolution of the two function $h * f$ according to the *convolution theorem* of the Fourier transform theory.

The total transmission t of the optical system with a filter with transmission function H is written in the Fourier domain as [55]

$$T(\nu_x, \nu_y) = H(\nu_x, \nu_y) \cdot F(\nu_x, \nu_y), \quad (3.23)$$

where $F(\nu_x, \nu_y)$ is the Fourier of the input function f , and the variables ν_x and ν_y are the spatial frequencies given in terms of the focal length f and the wavelength λ as

$$\nu_x = \frac{x}{\lambda f}, \quad \nu_y = \frac{y}{\lambda f}. \quad (3.24)$$

The Fourier transform of Eq. 3.23 results in the transmission of the light field on the image plane after the second lens. According to the convolution theorem the Fourier of a product of two functions is the convolution of their Fourier transforms, thus the transmission on the image plane is given by

$$t = F[H] * f. \quad (3.25)$$

In the case of diffractive dark-ground imaging, the transmitted light after the interaction with the atom cloud, is analyzed into a plane wave component E_0 (unscattered part of the probe light) and a field from the diffraction on the cloud. The Fourier transform of the light field E on the Fourier plane will consist of low spatial frequencies (frequency components close to the origin of the plane) originating mostly from the unscattered light E_0 being focused in the center, and of higher spatial frequencies (frequency components further from the origin) originating from the diffracted light collimated by the first lens. The filter placed at the center of the Fourier plane blocks the low frequencies without affecting the higher ones that

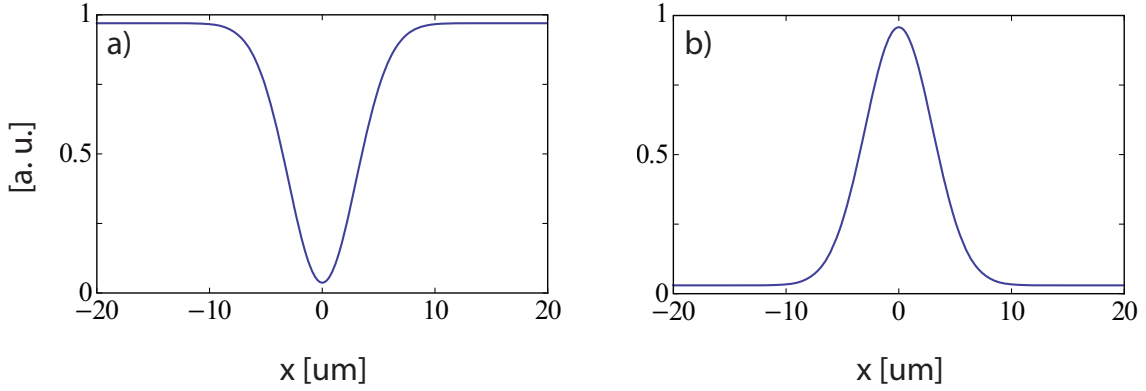


Figure 3.3: (a) Absorption profile from a probe beam on a Gaussian atom cloud described by Eq. 3.26 for a Gaussian shaped absorption coefficient $k(x)$. (b) Schematic representation of the profile of the image formed at the image plane using a filter at the Fourier plane of the first lens. The profile of the absorption is preserved on the image plane and appears positive on a suppressed background.

contain the information from the atoms. After the inverse transform is applied by the second lens, the shape of absorption from the atom cloud will appear on the image plane reversed (positive) on a suppressed background (Fig. 3.3).

The incident plane wave of the probe beam illuminating a small object (atom cloud) placed at the focal plane of the first lens (input plane) is modulated according to the transmission function of that object, which gives the input function f for the system. The atom cloud can be treated as a partially transmitting object due to the absorption of photon by the atoms with transmission coefficient $E/E_0 = 1 - k$. The transmission function in one dimension is given by

$$f(x) = \begin{cases} 1 - k & , |x| < a/2 \\ 1 & , \text{otherwise} \end{cases} , \quad (3.26)$$

where a is the diameter of the atom cloud, and k is the absorption coefficient. The amplitude of the incident wave E_0 is chosen equal to unity. Since the atom cloud has a Gaussian density, the absorption also has a Gaussian profile $k(x)$. In Eq. 3.26, the Gaussian profile is replaced by a flattop function for simplicity without affecting the argument at the end. The Gaussian absorption profile $k(x)$ is preserved on the image plane and it appears positive on a suppressed background [42].

In the case of an opaque disk, as it is used in the diffraction dark-ground imaging, the transmission function of the filter can be written in one dimension as

$$H(\nu_x) = \begin{cases} 0 & , |\nu_x| < b/(2\lambda f) \\ 1 & , \text{otherwise} \end{cases} , \quad (3.27)$$

where b is the diameter of the opaque disk aligned with the x -axis with its center at the origin, which is equivalent to a single slit in one dimension. The inverse Fourier for the transmission function of the filter is calculated as

$$F[H](x) = \delta(x) - \frac{\sin(bx/2\lambda f)}{\pi x}. \quad (3.28)$$

The total transmission of the optical system can be calculated from Eq. 3.25 using the above expression and the expression for the transmission of the object (Eq. 3.26) as

$$t = \begin{cases} -k + \frac{k}{\pi} \left[\text{Si} \left(\frac{b(2x+a)}{4\lambda f} \right) - \text{Si} \left(\frac{b(2x-a)}{4\lambda f} \right) \right] & , |x| < a/2 \\ \frac{k}{\pi} \left[\text{Si} \left(\frac{b(2x+a)}{4\lambda f} \right) - \text{Si} \left(\frac{b(2x-a)}{4\lambda f} \right) \right] & , \text{otherwise} \end{cases}, \quad (3.29)$$

where the sine integral function Si is defined as

$$\text{Si}(u) = \int_0^u \frac{\sin(t)}{t} dt. \quad (3.30)$$

The quantity $ab/\lambda f$ that appears in the arguments of the sine integral functions in Eq. 3.29 is much smaller than unity ($ab/\lambda f \ll 1$) for the set of parameters used in our experiment. When this inequality is fulfilled, it means equivalently that the dark spot of size b doesn't cut significantly on the low frequencies that contain the information of the object of size a , i.e. the filter is sufficiently smaller than the object. When $ab/\lambda f \ll 1$ applies, the argument of the sine integral functions is

$$u = \frac{b(2x+a)}{4\lambda f} \ll 1 \quad \text{for } |x| < a/2, \quad (3.31)$$

and for the sine integral function applies

$$\text{Si}(u) \simeq u \quad \text{for } u \ll 1. \quad (3.32)$$

Equation 3.29 in the region $|x| < a/2$ can be approximated in that case by

$$t_{\text{tot}} \simeq -k + \frac{k}{\pi} \frac{ab}{2\lambda f} \quad \text{for } |x| < a/2. \quad (3.33)$$

The intensity of the image of the atom cloud of diameter a is given by

$$I_{\text{im}} = |t_{\text{tot}}(x)|^2 \simeq \left[k \left(1 - \frac{1}{\pi} \frac{ab}{2\lambda f} \right) \right]^2 \approx k^2 \quad \text{for } |x| < a/2. \quad (3.34)$$

By means of numerical analysis, the second term in Eq. 3.29 is found to be $< 10^{-4}$ for $|x| > a/2$ and $ab/\lambda f \ll 1$, thus the background around the image is suppressed. In the general case, where a Gaussian absorption profile $k(x)$ is considered, the absorption profile is preserved on the image plane with peak intensity $\approx k^2$.

In the case where $ab/\lambda f \geq 1$, the image of the cloud is degraded, since the dark spot is cutting some of the lower frequencies that belong to the absorption image and contain information of the atoms.

3.4.3 Background level on the images

The dark spot is blocking the low frequencies of the focused probe beam at the Fourier plane, and, in the ideal case, this means the probe beam is blocked completely, and the background on the image plane is suppressed to zero. However, some of the rapidly varying components of the probe beam, which are caused by the interference from the imaging optics and the windows of the vacuum, or by the diffraction on speckles on the windows, are not blocked by the dark spot. Therefore there is a residual background light from the probe light that reaches the image plane, and appears as a finite background intensity level on the images. We define the ratio of extinction r_{ext} of the dark spot on the probe light as the reciprocal of the transmission coefficient of the filtered probe light on the image plane to the unfiltered probe light:

$$r_{\text{ext}} = \left(\frac{I_{\text{ref}}}{I_0} \right)^{-1}, \quad (3.35)$$

where I_{ref} is the intensity on the image plane of the background light from a filtered probe beam, and I_0 is the initial intensity of the probe beam.

The residual light E_{bg} of the attenuated probe beam reaches the image plane, where it interferes with the light field E_{abs} containing the information from the atoms as $|E_{\text{bg}} - e^{-i\phi} E_{\text{abs}}|^2$ with ϕ being the phase difference between the background and the light from the atoms. Assuming that there is not any further phase shift added to the light, the two fields interfere destructively, i.e. $\phi = \pi$. In the presence of a non-zero background on the image plane the shape of the images changes as shown in Fig. 3.4.

In the case where the background light field is greater than the light field from the absorption on the atoms ($E_{\text{bg}} > E_{\text{abs}}$) the image appears as a dip in a higher background level (Fig. 3.4(a)) similar to the images taken with a non-dark-ground method (such as in absorption imaging). In such a case, one is still able to extract the column density from the shape of the image and do quantitative measurements. In the case where the background level from the probe light is comparable to the light from the absorption ($E_{\text{bg}} \sim E_{\text{abs}}$) the number of atoms cannot be deduced due to ambiguity in the resulting image (Fig. 3.4(b)). Finally, in the case of a smaller background than the light from absorption ($E_{\text{bg}} < E_{\text{abs}}$), a dark-ground image is formed with its peak intensity decreased (Fig. 3.4(c)) as compared to a pure dark-ground image with zero background. The decrease in the intensity is due to the interference of the residual background with the light from the absorption. For measuring atom numbers, the effect of the background level can be neglected, when it is much smaller than the absorption light, and it is taken into account for small signals comparable to the background.

3.4.4 Dark spot size

The size of the dark spot is chosen so that the probe light is sufficiently attenuated without significantly reducing the light containing the information from the atoms.

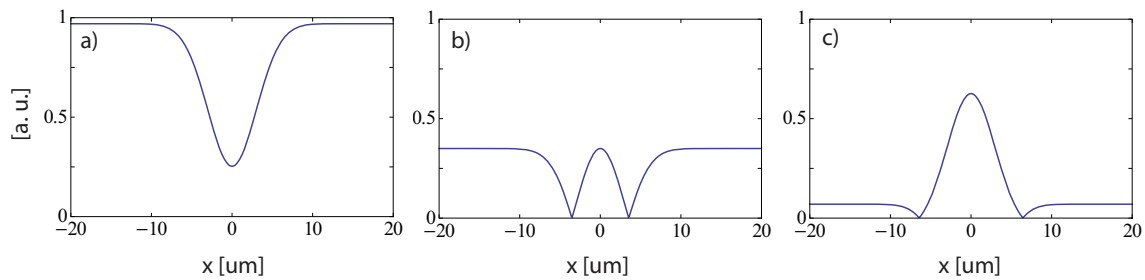


Figure 3.4: Image profiles at the presence of residual background level from the filtered probe beam. (a) The image appears as a negative dip in a higher level of background ($E_{\text{bg}} > E_{\text{abs}}$). (b) Effect on the image of a background comparable to the absorption light ($E_{\text{bg}} \sim E_{\text{abs}}$) (c) Dark-ground image at the presence of a smaller background ($E_{\text{bg}} < E_{\text{abs}}$). The peak intensity is reduced due to the interference of the residual background with the light from the absorption.

From the perspective of the Fourier analysis, the dark spot placed at the origin on the Fourier plane is chosen so that it is blocking most of the low frequencies of the focused probe beam without affecting significantly the lower frequencies of the light from the atoms. The diffraction of the light on the atom cloud can be treated as the diffraction on a circular aperture with diameter a equal to the diameter of the cloud. The radiation pattern of a source in the far-field is the Fourier transform of the light distribution of the source. For uniform illumination on a circular aperture, the zeroth-order Fraunhofer diffraction pattern is given by the Airy disk with diameter $2r_{\text{Airy}} = 2.44\lambda f/a$ [54].

The diffraction pattern obtained by an aperture whose transmission has a Gaussian variation, for example a Gaussian filter placed in front of a circular aperture, is also a Gaussian function. The output profile of single mode beam has a Gaussian intensity profile, and according to the diffraction equation it maintains that profile as it propagates away from the source [44].

The atom cloud at low optical densities has a Gaussian density distribution and a Gaussian transmission function, therefore the light from diffraction on clouds of low optical densities will also have a Gaussian profile. By replacing the central lobe of the Airy pattern with a Gaussian of the same volume as the Airy pattern, the $1/e$ diameter of the diffraction pattern from an aperture of diameter a with Gaussian transmission function is given by

$$w = 1.24 \frac{\lambda f}{a}. \quad (3.36)$$

In order for the light diffracted on an atom cloud of diameter a to be transmitted without being reduced significantly, the diameter b of the dark spot has to be much smaller than the diffraction pattern w , which is equivalent to the $ab/\lambda f \ll 1$ argument discussed in Sec. 3.4.2. Figure 3.5(a) shows the transmission coefficient over the ratio b/w of the light containing the information after passing the dark spot using the Gaussian profile for the pattern of diffraction. For the parameters of

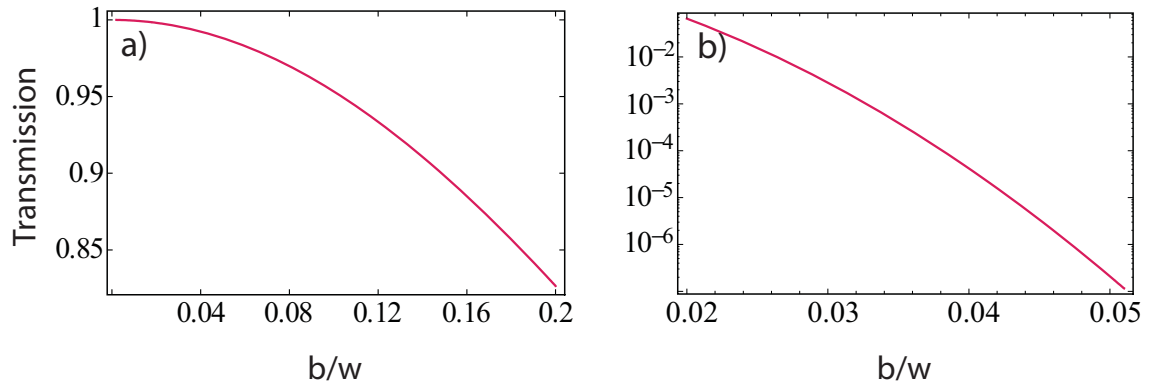


Figure 3.5: Transmission curves for a dark spot of diameter b assuming a Gaussian profile for the light. (a) Transmission curve of the light containing the information after passing the dark spot. The curve is plotted over the ratio b/w for an atom cloud of $1/e$ diameter of $30 \mu\text{m}$ and for the parameters of our experiment ($\lambda = 780 \text{ nm}$ and $f = 95.5 \text{ mm}$). (b) Transmission curve for the probe light plotted over the ratio b/w of the dark spot size to the diffraction pattern of the atoms for a probe beam with a diameter of 1 mm .

the experiment ($\lambda = 780 \text{ nm}$, $f = 95.5 \text{ mm}$) and for a typical $1/e$ diameter of the cloud of $30 \mu\text{m}$ using a dark spot of $200 \mu\text{m}$ results in a b/w ratio of 0.06 , which is sufficiently smaller than unity and does not cut down significantly ($< 3\%$) on the light from the atoms.

The size of the dark spot is also relevant to determine the ratio of extinction (Eq. 3.35) for the light of the probe beam. The size of the dark spot b has to be greater than the diffraction pattern w_d for a probe beam of diameter d , which sets a lower limit to the size of the dark spot. The extinction curve is plotted on Fig. 3.5(b) over the ratio b/w of the dark spot size to the diffraction pattern of the atoms for a probe beam with a diameter of $d = 1 \text{ mm}$. For $b/w = 0.06$, the predicted ratio of extinction is already very high. The higher spatial frequencies though, caused by interference between the vacuum windows or by diffraction on dust particles, are not cut by the dark spot resulting in a measured extinction of $r_{\text{ext}}^{-1} \sim 10^{-3}$. Some of the higher spatial frequencies can be suppressed by increasing the diameter b of the dark spot, thus a dark spot of a bigger size would account for a greater measured coefficient of extinction, although it would start to have an effect on the transmission of the light from the atoms. For a constant size of the dark spot, the above limitations can be bypassed by having an atom cloud of smaller diameter a ; the later can be achieved by decreasing the number of atoms in the trap or by having a stronger confining magnetic field. Smaller atom clouds also require a higher optical resolution for the imaging system.

3.4.5 Diffusion and expansion of the atom cloud during the imaging time

In diffractive dark-ground imaging, the atomic sample that has been prepared in the MOT is released from the trap and imaged in free space. At the moment of the trap switch-off, the atoms fly towards a random direction according to their initial velocity associated with their temperature at that moment. The temperature of the atoms in the MOT is expected at least one order of magnitude lower than the Doppler limit (140 μK for rubidium), as discussed in Sec. 2.1.1. The atoms have a thermal velocity given by $v_T = \sqrt{2k_B T/M}$, which for the Doppler temperature is $v_{T_D} = 0.16\text{m/s}$. For times shortly after the switch-off, the acceleration due to gravity has not yet become significant, and the cloud in free space expands isotropically.

During the imaging time, diffusion of the atoms due to spontaneous emission also results in the expansion of the atom cloud. When the atom cloud is illuminated by the probe beam, the photons that are absorbed by the atoms are spontaneously re-emitted towards a random direction. As discussed in Sec. 2.1.1, the spontaneous re-emission of photons leads to heating up of the sample and to the increase of the momentum of the atoms towards a random direction for each photon that is re-emitted. As a result, the atom undergoes a random-walk process both in velocity space and in position. The cumulative effect of N vector displacements at random direction of equal magnitude results in a total displacement with a magnitude given by [56]

$$r = \sqrt{N}\Delta r, \quad (3.37)$$

where Δr is the magnitude of an individual vector displacement. Similarly, in velocity space the magnitude of the total velocity displacement assuming N individual velocity displacements at random direction of equal magnitude is given by

$$v = \sqrt{N}\Delta v, \quad (3.38)$$

where the magnitude Δv is the velocity displacement from an individual spontaneous emission and is in our case equal the recoil velocity v_{rec} .

Due to the effect of spontaneous emission during the imaging time, the atom will travel a total distance of r towards a random direction, which leads to an average expansion of the radius of the cloud of

$$w_{\text{ave}} = \sqrt{w_0^2 + r^2}, \quad (3.39)$$

with w_0 the initial $1/e$ radius of the cloud. Equations 3.37 and 3.38 hold for any direction in space, although in imaging the plane perpendicular to the probe beam (imaging plane) is of interest.

An increase in the cloud size during the imaging time, either due to diffusion or because of an expanding cloud in free space, affects the transmission of the diffracted light, since an increase in a leads to an increase in the ratio $ab/\lambda f$ (Fig. 3.5). In order to keep the expansion of the cloud and therefore the change in the transmission low,

we require that the mean distance of expansion to be lower than the initial radius of the cloud and the resolution of the optics.

Another effect of the expansion of the cloud during the imaging time, is the decrease in the peak intensity I_{peak} of the image, since the light is spread on a larger area. The light intensity $I(x, y)$ on the image plane can be described by a two-dimensional Gaussian distribution with peak intensity I_{peak} and variance σ_x^2 and σ_y^2 . The total power is given by the integration of $I(x, y)$ as

$$P = \int_{-\infty}^{+\infty} \int_{-\infty}^{+\infty} I_{\text{peak}} e^{-\frac{x^2}{2\sigma_x^2}} e^{-\frac{y^2}{2\sigma_y^2}} dx dy = 2\pi I_{\text{peak}} \sigma_x \sigma_y, \quad (3.40)$$

thus, when the size of the cloud is increased by a factor of $\alpha = \sigma'/\sigma$ on the transverse plane, the peak intensity is decreased by a factor of α^2 , i.e. $I'_{\text{peak}} = I_{\text{peak}}/\alpha^2$, in order for the total power to maintain the same value.

The increase in the size of the cloud and the corresponding decrease in intensity have an effect on the estimated number of atoms from the images. From Eq. 3.19, the atom column density $n'(x, y)$ estimated from an image, where the initial intensity $I(x, y)$ has dropped by a factor of α^2 , scales as

$$n'(x, y) \sim -\ln \left[\left(1 - \sqrt{\frac{I(x, y)}{\alpha^2 I_0}} \right)^2 \right] \approx \frac{2}{\alpha} \sqrt{\frac{I(x, y)}{I_0}} \sim \alpha^{-1}, \quad (3.41)$$

where the approximation $-\ln[(1-x)^2] \approx 2x$ for $x \ll 1$ has been used valid at low optical densities ($D \ll 1$). From the above equation, at low optical densities, one can derive that the σ_n of the atom density distribution $n(x, y)$ are given by $(\sigma_{n,x}, \sigma_{n,y}) = \sqrt{2}(\sigma_x, \sigma_y)$, therefore $(\sigma_{n,x}, \sigma_{n,y})$ scales the same as (σ_x, σ_y) with respect to α :

$$\sigma'_n \sim \sigma' \sim \alpha, \quad (3.42)$$

for both directions of the imaging plane. The atom number that is estimated from the column density $n(x, y)$ over the whole image of a cloud that has expanded by a factor of α scales as

$$N' \sim n'_{\text{peak}} \sigma'_{n,x} \sigma'_{n,y} \sim \alpha. \quad (3.43)$$

The expansion of the cloud sets an upper limit to the illumination time τ of the probe beam, in order to keep the error of a to the atom number estimation small.

Apart from the motion of atoms towards all directions induced by diffusion from spontaneous emission, there is also motion induced by the absorbed photons along the imaging axis (z -axis). The photons that are absorbed by the atoms from the imaging beam during the imaging time impart momentum to the atoms in the cloud. This effect causes the atoms to move along the z -axis with a velocity v_{rec} for each absorbed photon, and the distance that the atoms have traveled during a certain time will be proportional to the scattering rate R_{sc} . The distance traveled by the atoms along the z -axis during the illumination time τ is

$$\Delta z = R_{\text{sc}} v_{\text{rec}} \tau^2, \quad (3.44)$$

which has to be much smaller than the focal depth of the optics to avoid having the atom cloud pushed out of focus during the imaging time. Assuming a Gaussian beam being focused by a lens, the depth of focus of the beam is $2z_{\text{R}} = 2\pi w_0^2/\lambda$, where z_{R} is the Rayleigh range and w_0 is the (minimum) beam waist at the position of the focus. At a distance z away from the focus, the beam spot size is given by

$$w(z) = w_0 \sqrt{1 + \left(\frac{z}{z_{\text{R}}}\right)^2}, \quad (3.45)$$

where $z = 0$ coincides with the position of the focus. For a distance equal to the Rayleigh range z_{R} away from the focus, the beam spot size is $\sqrt{2}w_0$.

Chapter 4

The Experimental Setup

In this chapter, the composing parts of the experimental setup are presented. The setup is a typical setup for cold atom experiments, which enables for the trapping of rubidium atoms in a MOT and for the application of the diffraction dark-ground imaging technique. The core of the experiment is the octagonal glass cell, in the center of which the atom trap is formed in ultra-high vacuum (UHV). The small compact vacuum system is kept in UHV ($\sim 10^{-11}$ mbar) using an ion-pump. Around the cell, collimated laser light is delivered by optical fibers in all three directions in space forming the MOT beams. The laser system, that is providing the light used for trapping and imaging of the atoms, is described throughout this chapter. The master laser, the slave laser, and all the other parts of the laser system are all constructed on separate optical boards. The optical boards are connected with optical fibers, which decouples each part of the laser system from the others in terms of optical alignment. The imaging system is a typical imaging system using standard optics. Our intention was to demonstrate the high sensitivity of the diffraction dark-ground imaging method on standard optics.

4.1 Lasers system

In the setup, the laser light (master laser) is generated by an external cavity laser diode operated at 780 nm. By use of optical feedback from a diffraction grating the frequency excursions of the diode laser are reduced to lower than 1 MHz suitable for laser cooling. The frequency of the diode laser is locked in order to stabilize it against mechanical vibrations and fluctuations in temperature and injection current. To meet the requirements in laser power for the experiment we make use of the master-slave arrangement, where the light from the master laser is injected in a second temperature stabilized diode laser (slave laser) to boost the output power. The light is then split in two parts. According to their task for the experiment, i.e. either for trapping or imaging, each part of the light undergoes a different frequency shift using acousto-optic modulators (AOMs).

In this section, the properties of the cooling transition of ^{87}Rb used in the experiments are discussed, and the different parts of the laser system are described,

that provide the light used for cooling and trapping in the MOT and the probe light used for imaging.

4.1.1 Hyperfine structure of ^{87}Rb

The electronic configuration for the ground state of ^{87}Rb is $5^2S_{1/2}$. The first excited state $5P$ is split due to spin-orbit coupling into two levels, $5^2P_{1/2}$ and $5^2P_{3/2}$, according to the angular momentum quantum number $J = L + S$. The hyperfine structure is occurring from the interaction of the magnetic moment of the electrons orbiting around the nucleus with the nuclear magnetic moment proportional to $\vec{\mathbf{I}}$. The magnetic moment of the electrons arising from their relative motion to the nucleus is proportional to the electron total angular momentum $\vec{\mathbf{J}}$. The conserved quantum quantity is the total angular momentum $\vec{\mathbf{F}} = \vec{\mathbf{I}} + \vec{\mathbf{J}}$. For the alkali elements, there is one valence electron in the outer shell. In the ground state the single valence electron has zero orbital angular momentum and spin angular momentum of $S = 1/2$. Thus the total angular momentum is $F = I \pm 1/2$. The hyperfine level splitting in the ground state for rubidium having nuclear spin of $I = 3/2$ results into two hyperfine levels with quantum numbers $F = 1$ and $F = 2$ respectively. The $5^2P_{1/2}$ excited level also splits into two hyperfine levels, and the $5^2P_{3/2}$ excited state splits into four levels as $F = I \pm 1/2, \pm 3/2$. The hyperfine energy level structure of ^{87}Rb is shown on Fig. 4.1.

The transition to the $5^2P_{1/2}$ excited state is referred to as the D_1 line and the transition to $5^2P_{3/2}$ as the D_2 line of rubidium. For the laser cooling we use the hyperfine transition $F = 2 \rightarrow F' = 3$ of the D_2 line at wavelength $\lambda = 780$ nm, where the unprimed F refers to the $5^2P_{1/2}$ and the primed F' refers to the $5^2P_{3/2}$ manifold. This transition has been chosen for laser cooling because it is a cyclic transition according to the electric-dipole selection rule $\Delta F = 0, \pm 1$. Our laser frequency is tuned to excite the $F = 2 \rightarrow F' = 3$, however the laser also excites with small probability the non-resonant transition of $F = 2 \rightarrow F' = 2$. From the $F' = 2$ state, the atoms may decay to the $F = 1$ lower hyperfine state of the ground state, which is a dark state, i.e. the cooling light cannot excite the atoms to $F' = 3$. For that reason, a second frequency is needed to drive the $F = 1 \rightarrow F' = 2$ transition, from where they can decay back to either the $F = 2$ or the $F = 1$ states. This second frequency, termed as the repumper frequency, is embedded in the laser system by the AM modulation of the laser used for cooling. The amplitude modulation on the main laser produces sidebands at the repumper frequency, that drives the $F = 1 \rightarrow F' = 2$ transition.

4.1.2 Extended cavity master laser

For the cold atom experiments, it is required that the laser linewidth is small compared to the natural linewidth $\Gamma = 2\pi \times 6$ MHz of the transition used for cooling. Furthermore, stabilization of the laser's frequency over temperature and current drifts is required.

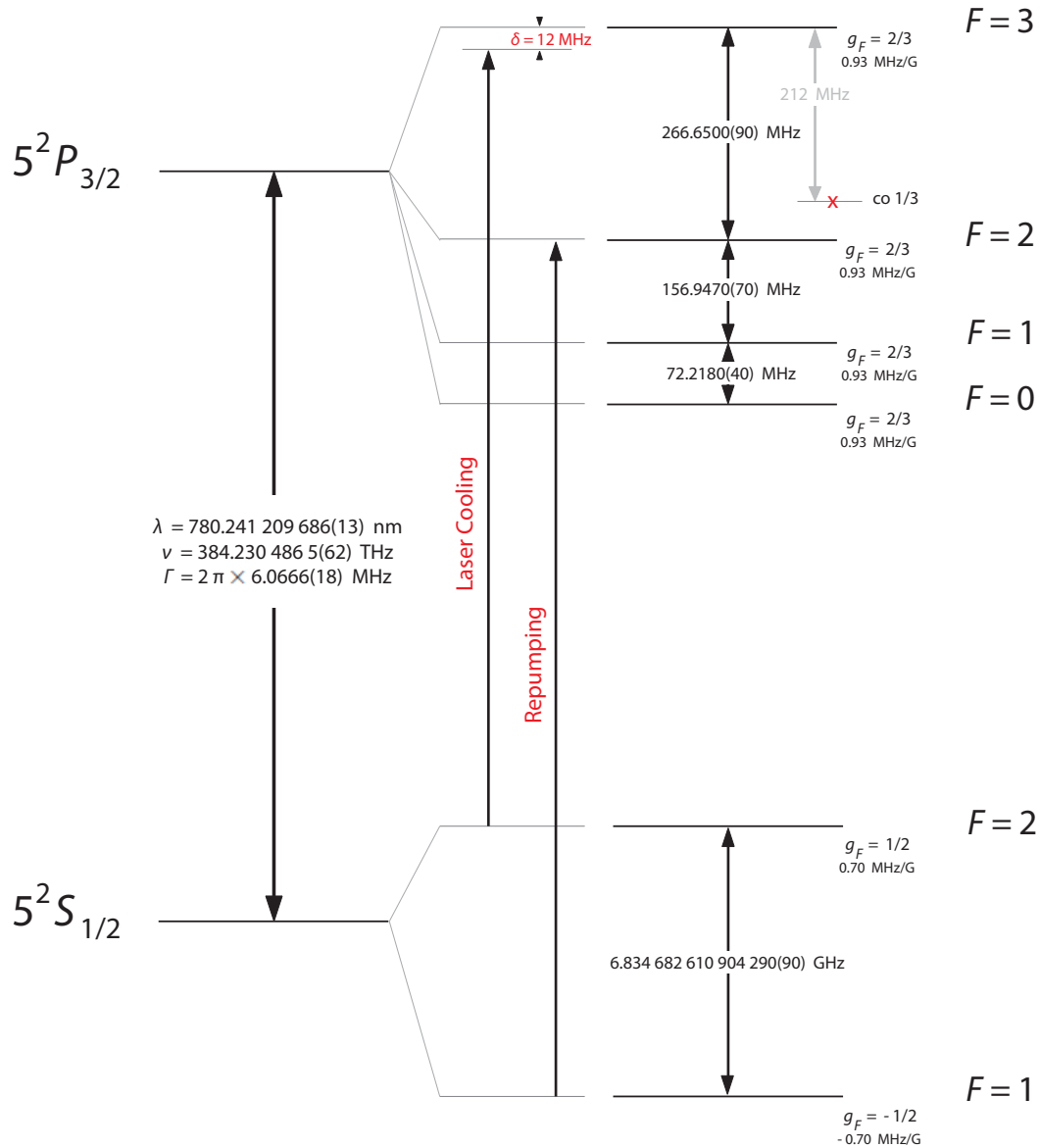


Figure 4.1: Hyperfine level structure of the D_2 line of ^{87}Rb [57, 58]. The hyperfine level spacing is shown to scale within each manifold, but is not to scale between the ground state and the excited state manifolds. The approximate Landé g -factors are given for each hyperfine level together with the Zeeman splitting between the magnetic sublevels to the corresponding hyperfine level. The cooling laser drives the $F = 2 \rightarrow F' = 3$ cyclic transition with its frequency red-detuned by $\delta = 12$ MHz below the resonance. The repumper frequency drives the $F = 1 \rightarrow F' = 2$ transition putting atoms back to the upper hyperfine level of the ground state. To stabilize the frequency of the laser, the laser is locked to the $F = 1 / F = 3$ crossover line (red cross) using Doppler-free spectroscopy. The laser's frequency is then shifted by use of an AOM to the appropriate frequency for the cooling transition.

For our master laser, we use an extended cavity diode laser configuration [59–61] operating at 780 nm. The extended cavity is made by an optical grating placed in front of the diode laser. The first order of the diffracted beam on the grating is fed back to the diode, while the zeroth order is decoupled and used as the laser source. The optical feedback to the laser reduces the current threshold and narrows the linewidth to less than 1 MHz. The length and the tilt angle of the external cavity are controlled by piezo-electric crystals (PZT) attached to the back of the grating. The use of PZTs achieves a wide range (of several GHz) in tuning the frequency, and it also enables the electronic locking of the frequency via the application of a feedback signal.

The temperature is stabilized by a Peltier element attached to the mount of the laser. The Peltier element is controlled by a temperature controller (THORLABS TED 200). The injection current of the diode laser is controlled by a home made current control driver designed for low noise operation. The same signal that is used as feedback for frequency stabilization is applied both to the current driver and to the piezo crystals driver. The diode and the grating are enclosed within a metal box to seal off any air current disturbances. The whole setup of the metal box and the rest of the external optics used for the Doppler-free spectroscopy are placed on a marble slab to reduce mechanical vibrations.

Laser frequency stabilization

The laser frequency stabilization is achieved with Doppler-free saturation spectroscopy. The saturated absorption spectrum is obtained from a rubidium vapor cell. A strong pump beam and a weak probe beam propagating in the opposite direction are crossing with a small angle at the region of the vapor cell. The absorption profile from a sole probe beam results in a broadened profile due to the relative velocities of the atoms with respect to the probe beam. The broadened profile known as the Doppler profile has a linewidth of the order of ~ 100 MHz. The presence of the strong probe beam depletes the number of atoms in the ground state with zero velocity. This results in a drop in absorption at the resonance of the transition, and appears as a sharp dip of ~ 1 MHz on the much broader Doppler profile. The substitution of the two signals results in a Doppler-free signal, where only the sharp peak of the transition is observed.

By scanning the frequency of the laser, the full hyperfine spectrum is obtained where each of the hyperfine levels is discerned as a separate sharp peak. In the spectrum there are also other lines present in between the hyperfine lines known as crossover lines. A crossover peak appears in the middle between two transitions that have the same lower level and different excited levels. When the laser is tuned in the middle of the two transitions, because of the Doppler effect, atoms from a certain velocity class moving for example towards the pump beam see the pump beam in resonance with the higher frequency transition. At the same time, they see the probe beam in resonance with the lower frequency transition. As a result, saturated absorption occurs also in the middle of these two transitions, which appears as an additional peak on the saturated absorption spectrum.

The frequency is locked to the $F = 2 \rightarrow F' = 1$ and $F = 2 \rightarrow F' = 3$ crossover line of the saturated absorption spectrum. A photo-diode is used to collect the fluorescence from the vapor cell which is proportional to absorption. For the frequency locking we use the dichroic laser locking technique [62, 63]. At the presence of a weak external magnetic field created by a coil around the vapor cell, the saturated absorption spectrum is shifted in frequency due to the Zeeman effect. The linearly polarized probe beam, that propagates longitudinally to the magnetic field, can be considered as being composed of the two σ^+ and σ^- polarization states. This shifts the signal in frequency into two opposite directions.

The two antisymmetric components are differentiated to generate a signal with zero crossings (dispersion-like signal), which is used as the error signal. The resulting error signal is used as feedback control to both the laser current and the PZT array.

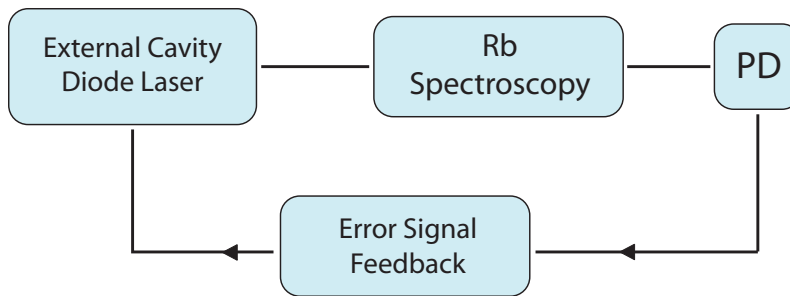


Figure 4.2: Schematic of the frequency stabilization electronic feedback loop to the master laser. The fluorescence signal from the Rb cell, which is proportional to the Doppler-free saturated absorption signal, is collected with a photodiode (PD). A weak magnetic field around the Rb cell splits the signal into two identical components shifted in frequency towards opposite directions. The two components are separated with a waveplate and recombined to give a dispersion-like signal, which is used as error feedback control to the master laser.

4.1.3 Slave laser

The output of the master laser has a good quality spectral characteristics, that is a narrow linewidth as compared to the natural linewidth of the cooling transition and it is frequency locked. The output power though is low of about 2 mW, whereas for the experiment, a total laser power of $\simeq 20$ mW is required for the MOT of small atom numbers. To amplify the output laser power, we use a second diode laser in the master-slave configuration. The slave diode laser is a high output power (80 mW) laser diode operating in a very broad frequency band. The output beam of the slave diode is collimated by an objective and the diode is temperature stabilized by a Peltier element and a temperature controller (THORLABS TED 200). The light from the master laser is directly injected into the slave diode laser transferring all its good quality spectral characteristics to it. The slave laser, after the injection from the master laser, has the same linewidth with the master, a locked frequency

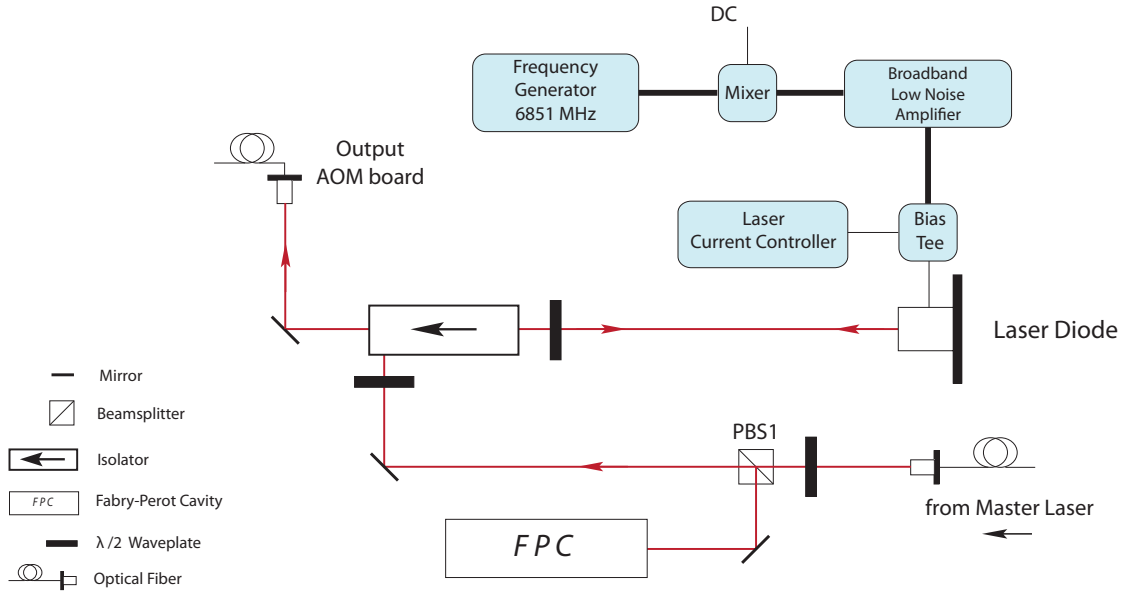


Figure 4.3: Schematic of the slave laser layout. The light from the master laser is injected into the slave diode laser. The slave diode laser has a high output power (~ 60 mW) and the same linewidth with the master laser. An optical isolator is blocking the back-injection with reflected light from the high power slave laser, that would disturb the laser frequency stability. A microwave waveform at the repumper frequency (6850 MHz) is modulating the injection current of the diode laser. A small part of the light is injected into a Fabry-Pérot cavity for monitoring the spectrum.

and an output power of ~ 60 mW. In Fig. 4.3 the optical setup for the injection of the slave laser is depicted.

Repumper frequency

The light of the slave laser is tuned to drive the $F = 2 \rightarrow F' = 3$ cyclic transition, whereas, for the trapping to occur, a repumping of the atoms that have decayed in a dark state is required. The repumper frequency driving the $F = 1 \rightarrow F' = 2$ repumping transition is embedded in the laser system via the AM modulation of the frequency of the light of the slave laser. A small percentage of the slave laser power is modulated into sidebands at a fixed distance around the center frequency. The modulation is achieved by directly modulating the diode laser current. By having a small percentage of the power on a sideband at a distance equal the repumper frequency trapping of atoms is achieved [64].

The light is frequency locked to the $F = 2 \rightarrow F' = 3$ transition of 780 nm, which is in the order of THz. It can be described by a sine wave as $c(t) = \sin(\omega_c t)$, where the frequency $\omega_c/2\pi$ is driving the $F = 2 \rightarrow F' = 3$ transition and is the carrier frequency. To drive the $F = 1 \rightarrow F' = 2$ transition, we form the frequency $(\omega_c + \omega_m)/2\pi$ with

$$\omega_m/(2\pi) = 6834.68 - (266.65 + \delta) \quad (\text{MHz}), \quad (4.1)$$

where the 6835 MHz is the difference between the $F = 1$ and $F = 2$ levels of the ground state and the 267 MHz is the difference between the $F = 2$ and $F = 3$ levels of the excited state (Fig. 4.1). For a typical detuning of $\delta = 12$ MHz, this results in a modulation frequency of $\omega_m/(2\pi) = 6850$ MHz. The modulating waveform can be written as $m(t) = M \cdot \cos(\omega_m t + \phi)$ with $\omega_m \ll \omega_c$. The amplitude modulation is created by the product

$$y(t) = [A + M \cdot \cos(\omega_m t + \phi)] \cdot \sin(\omega_c t), \quad (4.2)$$

where A represents the amplitude of the center frequency waveform $c(t)$ controlled by the current controller of the laser diode. The modulated waveform is written as

$$y(t) = A \cdot \sin(\omega_c t) + \frac{M}{2} [\sin((\omega_c + \omega_m)t + \phi) + \sin((\omega_c - \omega_m)t + \phi)]. \quad (4.3)$$

The modulated light has, apart from the central component, two components at the frequencies $(\omega_c - \omega_m)/2\pi$ and $(\omega_c + \omega_m)/2\pi$, where the later is the repumper frequency for our experiment. The Fourier of Eq. 4.3 is

$$Y = \pi A \cdot \delta(\omega - \omega_c) + \frac{i\pi}{2} [\delta(\omega - (\omega_c - \omega_m)) - \delta(\omega - (\omega_c + \omega_m))], \quad (4.4)$$

where only the one-sided spectrum for positive frequencies is written. In Eq. 4.4 the presence of the two sidebands around the central frequency ω_c becomes more apparent. In Fig. 4.4 is shown a typical spectrum of the cooling laser light taken with the Fabry-Pérot cavity. The power in the sidebands is 5% with respect to the central component.

The frequency of 6850 MHz is generated by a microwave frequency generator and it is amplified by a low noise 7dBm output microwave amplifier (Fig. 4.3). For the modulation of the injection current of the diode laser the microwave is combined with the DC current from the injection current controller via a bias tee module (Minicircuits ZFBT-4R2GW) connected close to the end connection of the coaxial cable delivering the microwave. The microwave is also combined with a small DC voltage on a mixer (MiniCircuits ZMX-8GLH) in order to control the output microwave power. The output microwave power determines the size of the sidebands with respect to the center frequency (modulation index).

4.1.4 The AOM board

After the light has been amplified at the slave laser, it enters the AOM board (Fig. 4.5), where it is split into two parts. Each part of the light is driven through a separate acousto-optic modulator (AOM), where it undergoes a slight shift in frequency according to the task it is fulfilling in the experiment.

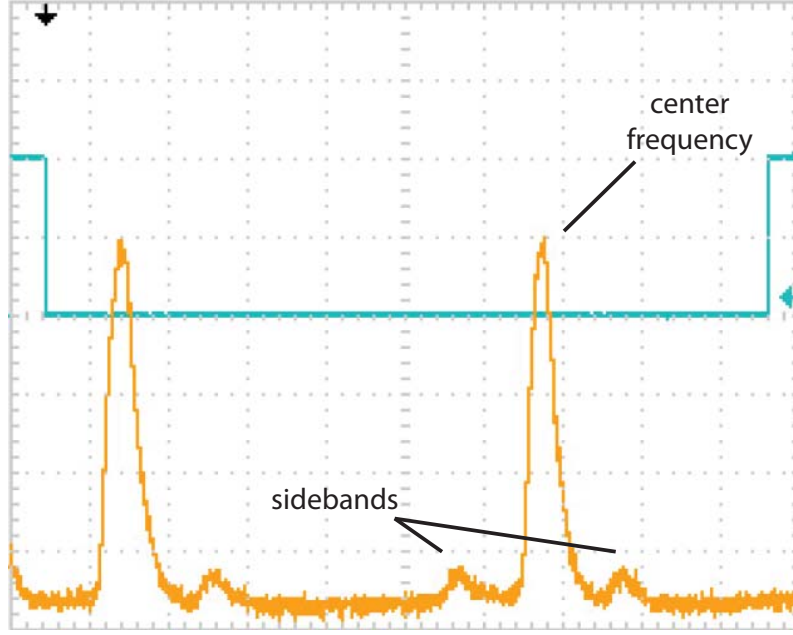


Figure 4.4: Spectrum of the slave laser light taken with the Fabry-Pérot cavity. The central frequency and the sidebands are depicted. The power in the sidebands is 5% with respect to the central component. On the left, a mirror image is visible from the triggering pulse of the oscilloscope.

The laser light is initially frequency locked to the $F = 1 / F = 3$ crossover line, that lies 212 MHz below the resonance of the cooling transition. The part of the light that is used for cooling in the MOT is sent through AOM1, where it is shifted by 200 MHz resulting in a detuning of 12 MHz below resonance. The other part of the light going through AOM2 is shifted by 212 MHz into resonance, and is used as resonant probe light in the diffractive dark-ground imaging technique.

The AOM consists of an optical medium (TeO_2) with a piezo-electric transducer attached to it. An RF generator is driving the transducer with an RF waveform, and the vibrations from the transducer gives rise to traveling sound waves in the optical medium. The contractions from the sound wave are causing the index of refraction of the medium to change periodically creating a Bragg diffraction grating. The light passing through the optical medium is diffracted and the light frequency is shifted due to the interaction with the propagating sound wave (Fig. 4.6) with the 1st order of diffraction having a frequency shift of Ω , the 2nd order a shift of 2Ω etc. By tuning the RF oscillation frequency, one is able to change the wavelength of the sound wave and hence the frequency shift Ω . The diffraction angle changes with the wavelength of the sound wave as

$$\sin \theta_B = m\lambda/2\Lambda , \quad (4.5)$$

where $m = 0, \pm 1, \dots$ the order of diffraction, λ the wavelength of the incident light and Λ the wavelength of the acoustic wave. By changing the angle of incidence, the

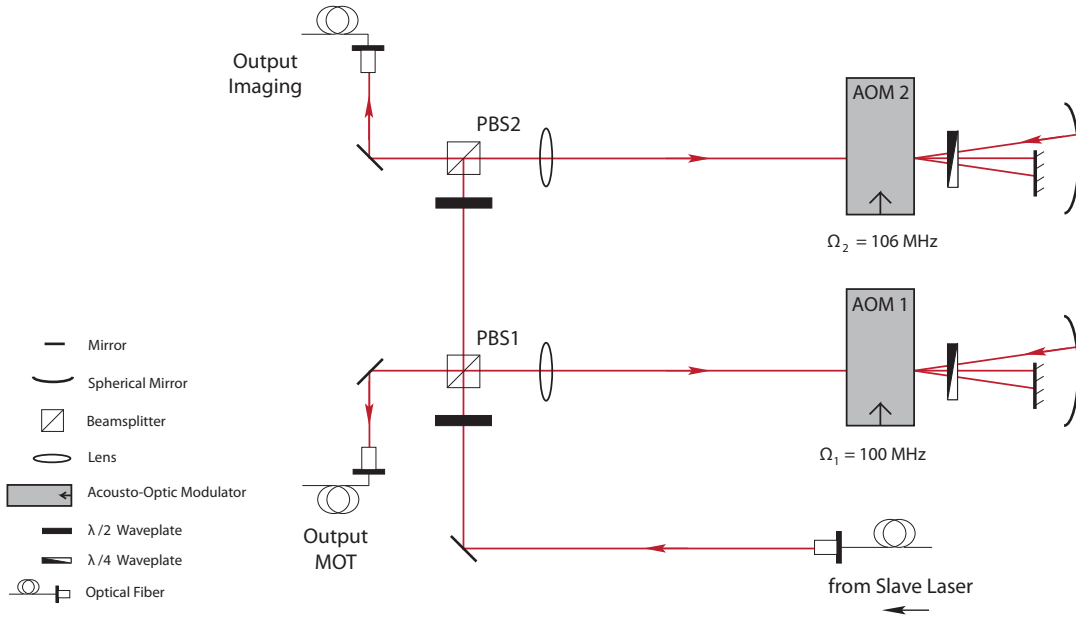


Figure 4.5: Schematic of the AOM board. The light is split into two parts, and each part is driven through AOM1 and AOM2 respectively. Both AOMs are in the double-pass configuration. The lens before each AOM focuses the beam to the center of the AOM, which coincides with the center of a spherical mirror. The +1 order is reflected by the spherical mirror back to the center and passes through the AOM a second time. The rest of the orders are blocked after the first pass. AOM1 and AOM2 are operated at frequencies $\Omega_1 = 100$ MHz and $\Omega_2 = 106$ MHz respectively, where the total frequency shift to the first order is 2Ω in the double-pass configuration. The light that passes through AOM1 is used as trapping light in the MOT and the light that passes through AOM2 is used for imaging.

power distribution of the incident light to the different orders of diffraction changes. We observed about 75% of the incident light being diffracted in the first order.

In the setup we use two AOMs (IntraAction, ATM-1101A2) both with center frequency of 110 MHz. The drivers (IntraAction, DE-110) for the AOMS consist of an RF generator, a broadband RF amplifier, a power supply, and enable for the tuning of the frequency and the amplitude of the diffraction, either manually or through computer control. Both AOMs are in the double-pass configuration. In the double-pass configuration the 1st order is reflected back to the AOM by a spherical mirror, where it undergoes a second frequency shift. The center of the AOM is positioned at the center of the curvature of the spherical lens; thus the diffracted beam is always reflected back to the center of the lens through the same point where it originally came from. In the single-pass configuration, any change in frequency means also a change in the diffraction angle. In the double-pass configuration, the beam is always reflected back through the center, which enables for a wide range of frequency tuning without displacing the beam.

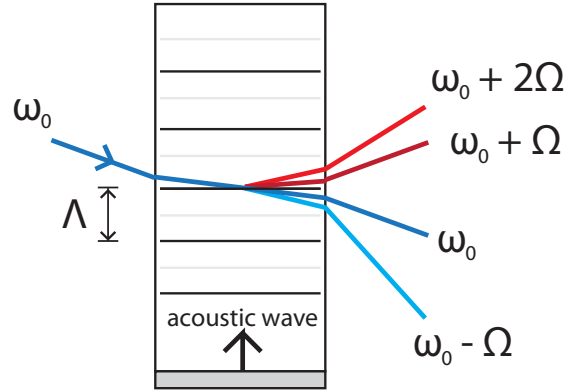


Figure 4.6: The operation of the AOM is based on Bragg diffraction on a propagating sound wave that creates periodic changes on the index of refraction of an optical medium. The frequency of the diffracted beam is shifted according to the order of the diffraction as $m\Omega$, where $m = 0, \pm 1, \dots$ is the diffraction order. The transducer (bottom) driven with RF induces sound waves through the optical medium, that propagate upwards. The positive orders $m > 0$ are diffracted upwards along the direction of the sound wave, and the negative orders $m < 0$ are diffracted downwards opposite to the direction of the sound wave.

4.2 The vacuum system

Experiments on cold atoms require a very high vacuum ($> 10^{-8}$ mbar) to reduce background gas collisions and to achieve a prolonged time of the cold atoms staying in the trap. In our system we opt for ultra high vacuum (UHV) corresponding to pressures of the order of $> 10^{-10}$ mbar, which results in long loading times for the MOT of greater than 10 s. For our low atom number experiments a long loading time and a low pressure is important, since it also decides the lifetime of single atoms in a low atom number MOT (Section 2.4.3).

Our vacuum system (Fig. 4.7), is a small compact vacuum system suitable for a simple MOT setup. The connection tubes are stainless steel. The experiments in the MOT are conducted in the vacuum octagon glass cell, which is pumped by an 25 l/s ion pump (Gamma Vacuum - TiTan 25S). The small volume and the small interior surface of our vacuum system enables us to reach UHV and pressures below 10^{-10} mbar. The pressure is monitored by an ionization gauge. The ion pump was kept at a distance of 60 cm from the location of the MOT in the glass cell to reduce interference from the magnetic field of the ion pump. In all other cases the volume has been kept as small as possible. The vacuum system is initially brought to a pressure of $\sim 10^{-6}$ mbar with a turbo-molecular pump (TPU 55 Pfeifer Balzers). At that pressure, the ion-pump is switched on, and the valve connecting the turbo pump to the system is closed. With the ion pump running, we perform a bakeout up to 180°C to clear the interior from water and other gases that could outgas from the materials and to remove any heavy particles stuck on the walls. After cooling the system down to room temperature, we are able to reach a pressure of $\sim 10^{-11}$ mbar.

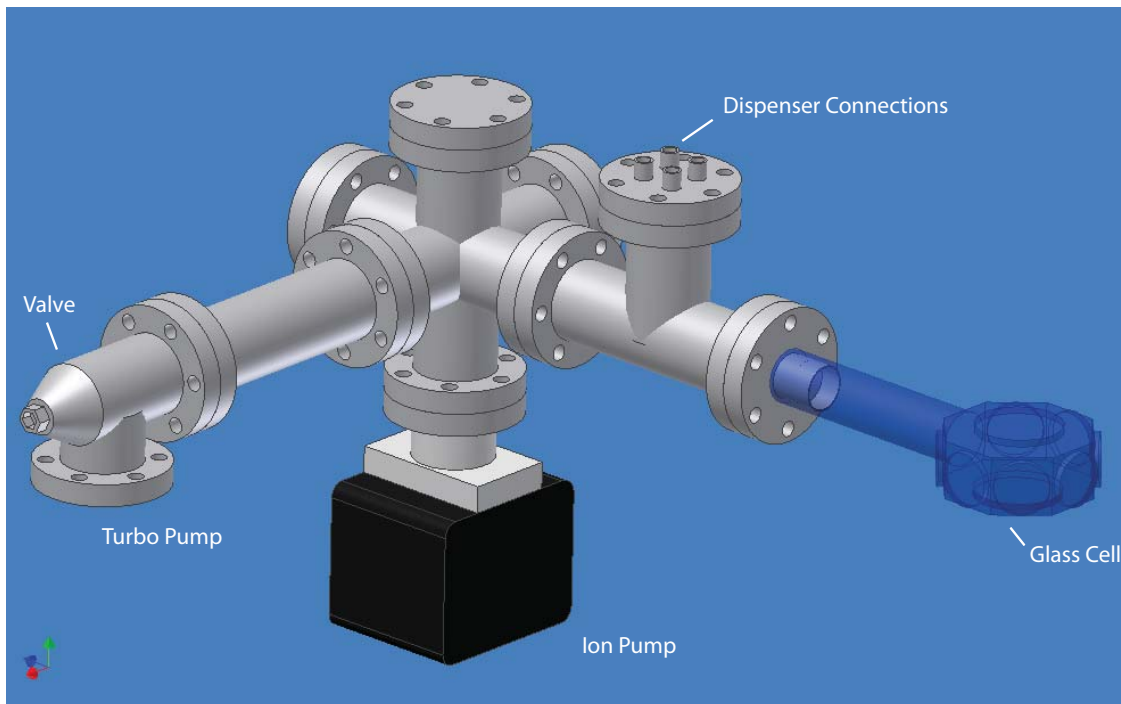


Figure 4.7: The vacuum system composed of the glass cell, the dispenser rubidium source and the ion pump. A turbo-molecular pump is used to bring the system down to $\sim 10^{-6}$ mbar. At that point, the ion pump is turned on. The ion pump brings the system down to the pressure of $\sim 10^{-10}$ mbar. After the ion pump is switched on, the valve of the turbo pump is closed. The ion pump is always in use maintaining the ultra-high vacuum.

4.2.1 The getter source

As the rubidium source we use a set of two dispensers (SAES Getters) located on the top flange of the intersection tube adjacent to the cell (Fig. 4.8). Each one of the dispensers is connected to the DC power supply with a high current feedthrough attached to the top flange and can be operated separately. The dispensers, also referred to as the getter source, are designed to deposit large amounts of Rb when run with a few A of current. The current passing through the dispenser is causing the temperature to rise to over 300 °C. At that temperature, the rubidium undergoes a reduction reaction, and atomic Rb vapour is released from the dispenser. The reduction reaction is occurring above a certain threshold of operating current, which for our case was found to be 2.8 A

Before being used in the experiment, the dispensers were degassed along the rest of the vacuum system by running them below the threshold current during the bakeout of the vacuum system. To get the dispensers started, one needs to give the dispenser several high current pulses (about 8 A for 5 s) to get rid of the dirt deposited on the dispenser preventing Rb vapor atoms from being released. After this process of several pulses is completed, the dispenser is operated at currents of

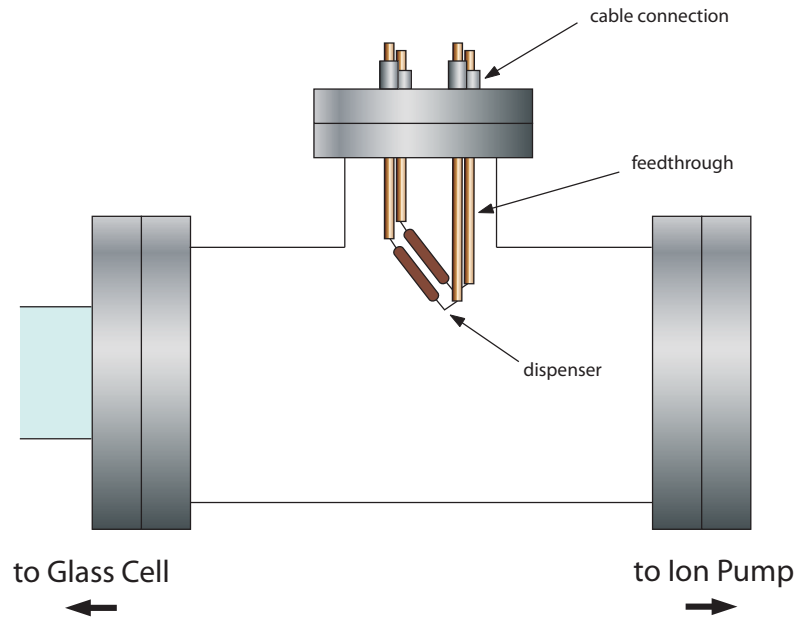


Figure 4.8: Closeup of the location of the dispensers inside the vacuum system. The dispensers are attached to the top flange of the tube that is connecting the glass cell to the vacuum system. Copper rods are used as feedthroughs.

3 to 3.3 A. For a constant current on the dispenser, there is constant Rb pressure in the vacuum cell and a uniform loading rate during the experiments.

4.2.2 The octagon glass cell

At the center of the vacuum cell is where the low atom number MOT is formed that is used as an object for our diffractive dark-ground imaging technique. Optical access from several direction is required, therefore, an octagon shape was adopted for the glass cell. This provides us with enough view ports for the three pairs of the MOT beams and a clear optical path for the probe beam for imaging. The octagon cell is made of fused silica (Technical Glass Inc.), and has a diameter of 80 mm. The windows are made of quartz and are antireflection coated. The windows have a diameter of 24.5 mm, except for the two windows on the top and the bottom edge of the cell, which have a diameter of 36.75 mm. The cell is connected to a 100 mm glass tube, which is fused to a stainless steel CF flange compatible with the rest of the vacuum system.

4.3 The magnetic coils

To produce the quadrupole magnetic field for the MOT we use a set of two identical circular coils placed in anti-Helmholtz configuration. The two coils are made from Coertz Audio (Alphacore, 4.9 mH) and are wound from thin copper foil. The coils have an outer diameter of 100 cm, an inner diameter of 10 cm, and a width of

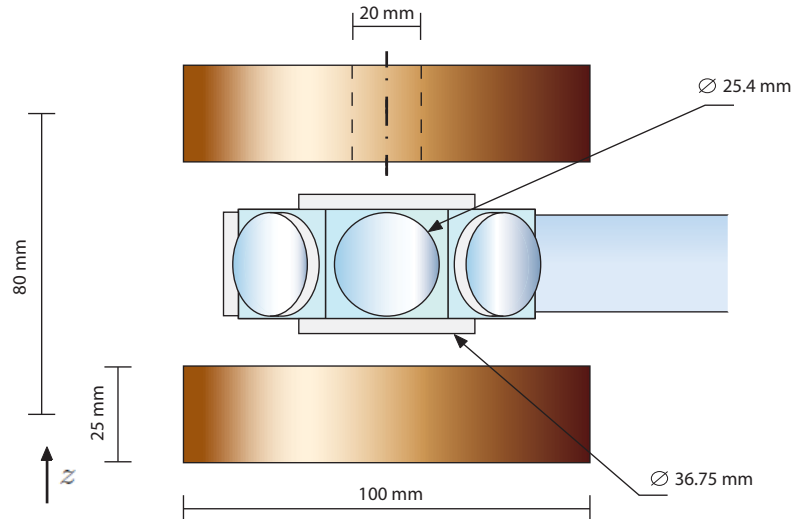


Figure 4.9: Closeup of the vacuum glass cell with the two coils placed on both sides. The coils were placed at a distance of 80 mm apart. The separation distance of the coils was limited by the mechanical construction supporting the coils.

25.4 cm. The thickness of the copper foil is 0.125 mm plus an insulating film of 0.06 mm, which results in about 320 turns. The advantage of thin copper foil is that it give a high number of turns and a packed geometry, though at the cost of high resistance. A small packed geometry for the coils interferes less with the mechanical parts of the vacuum system and enables the coils to be placed closer to the cell and to each other. Smaller separation distances between the coils result in higher gradients. (Eq. 2.19)

The coils are placed on the two sides of the cell along the top and the bottom windows (Fig. 4.9) at a distance of 80 mm apart. Before installation, the magnetic field of the coils was measured with a Hall-probe along the z -axis ($\rho = 0$), and it is plotted in Fig. 4.10. This process of measuring the gradient was repeated for various currents through the coils, and we were able to extract the current dependence of the magnetic field gradient as $b = 13.5 \text{ G/cm/A}$ [65]. At an operating current of 5.5 A, the gradient used for the experiment was 75 G/cm with the temperature from heating up of the coils being the limiting factor. The level of the current, as well as the switching on and off of the coils, was controlled by an analog signal send to the power supply of the coils.

Compensation coils

The compensation coils are used to cancel the effects of external magnetic fields, with the main contribution coming from the earth's magnetic field (0.5 G) and from the ion pump's magnets. The required compensating magnetic field is of the order of a Gauss, and can be achieved with distant coils of a large geometry, and a few amps of current per coil. The coils on the x and y axis have dimensions of $47 \times 58 \text{ cm}$ and $47 \times 47 \text{ cm}$ on the z axis, and they are sitting 47 cm apart. This geometry is

large enough so that it doesn't interfere with any of the mechanical parts of the vacuum. Each coil pair on each of the three axis is in Helmholtz configuration, i.e. the two coils are run by parallel currents. The Helmholtz configuration creates a homogeneous field at the center with the homogeneity region spanning over a few centimeters for the geometry of our coils. With 2-3 amps of current and about 90 turns for each coil, we are able to create a magnetic field of ≈ 1 G, which is enough to cancel the external magnetic field. In order to tune the current of the coils to nullify the external magnetic field, a high sensitivity (\sim mG) fluxgate sensor (Stefan Mayer Instruments, FLC 100) was utilized.

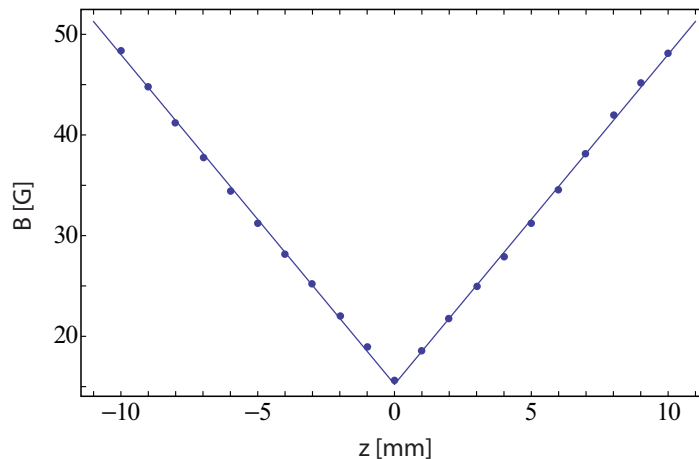


Figure 4.10: Measured B-field along the z -axis for the coils used in our setup. The current of the coils for this measurement was 2.4 A resulting in a field gradient of ~ 32 G/cm

4.4 The MOT

After it has been shifted in the appropriate frequency on the AOM board, the trapping light is split into three parts on a distribution board. The distribution board has one input and three outputs, and splits the light into three parts of equal power using polarizing beamsplitters. The light is delivered to the MOT by use of polarization maintaining optical fibers, one for each axis of the MOT (Fig. 4.12). The light that is delivered with the fibers is collimated by a lens on each axis forming a beam of 6 mm diameter. For our low atom number experiments, the beam size is reduced further by the use of irises, which results in a smaller trapping volume of the MOT. The linear polarization of the beam is turned into circular by the use of a quarter-waveplate. As described in Section 2, the beams on the xy -plane have an opposite circular polarization than the beam on the z -axis, and the absolute direction of circular polarization is determined according to the direction of the magnetic field lines. For example, if the magnetic field lines are pointing towards

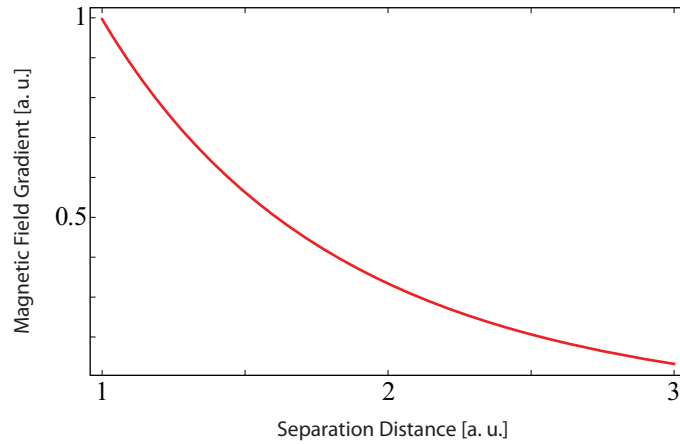


Figure 4.11: Variation of the magnetic field gradient with the separation distance of the quadrupole coils. The curve is a result of a simulation of the magnetic field for the coil geometry we use for the experiments. The field gradient is reduced with increasing separation distance of the coils.

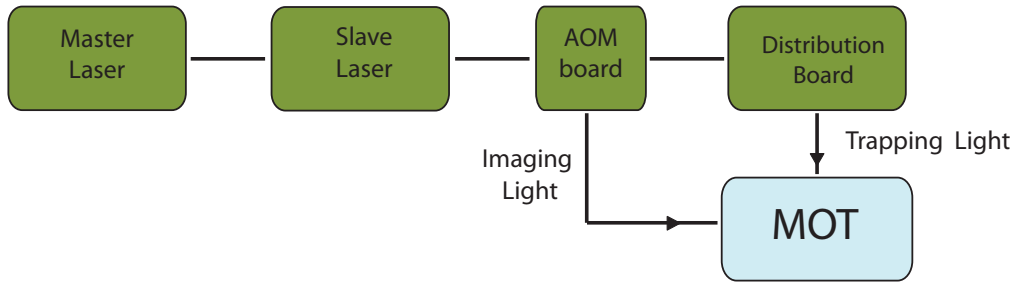
the origin on the xy -plane and away from the origin along the z -axis, the beams on the xy -plane have polarization σ^- with respect to the frame of an atom moving opposite to the light, and the beams on the z -axis have polarization σ^- with respect to the same frame.

The light that is delivered by the fibers is reflected back to its origin by a mirror on each axis. A quarter-waveplate before each mirror maintains the correct circular polarization for the reflected beam. The original beam together with the reflected one form a pair of counter-propagating beams on each axis. This particular configuration, which uses three beams reflected back by mirrors, is known as a "retro-reflected" MOT. The three beam retro-reflected MOT due to the reflection of the beams on each axis results in a factor of 2 gain in the total light power for atom clouds of low density. In the setup, for a typical experiment, the power of the MOT beams is 16 mW in total, which results in a saturation parameter of $s = I/I_{sat} \simeq 5$ per beam.

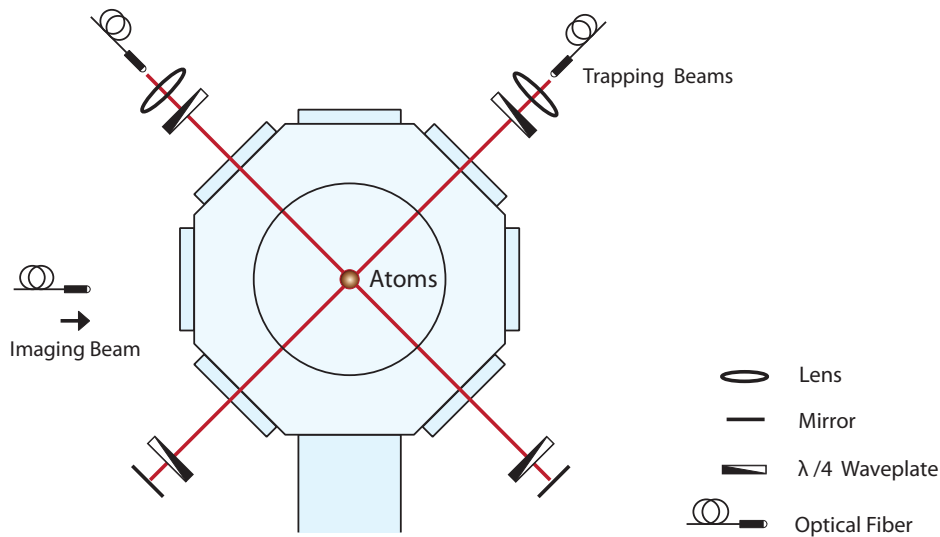
4.5 The imaging system

4.5.1 The CCD camera

The charge coupled device (CCD) used for imaging in our experiments is an Andor iKon-M (DU934N-BR-DD) Low-Noise CCD camera. The square CCD-chip on the detector consists of an array of 1024×1024 pixels with each pixel having a pixel size of $13 \times 13 \mu\text{m}$. The overall size of the chip is $13.3 \times 13.3 \text{ mm}$. Photons that fall on the CCD chip during the exposure time stimulate the accumulation of electrons on each pixel. The maximum number of electrons that can be accumulated, termed



(a)



(b)

Figure 4.12: (a) Block diagram of the light used in the experiment. Each part of the experiment represented by a block is connected to the other parts by optical fibers. In the AOM board the light is split into the light for trapping and the light for imaging. Each part of the light undergoes different frequency shift. Before being delivered to the MOT, the trapping light is split into three equal parts, one for each axis of the retro-reflected MOT. (b) Schematic of the retro-reflected MOT. The trapping light is delivered to the MOT by use of fibers, one on each axis (the light on the z -axis is not shown). Each beam is reflected by a mirror to create the counter-propagating beam on each axis. A quarter waveplate before each mirror maintains the right circular polarization for the counter-propagating beam.

as the well depth, is 1×10^5 electrons/pixel. The quantum efficiency (QE) of the camera, the efficiency of which photons that fall on the CCD are registered as counts, is 95% at the wavelength of 780 nm. The high QE of the camera is achieved with back-illumination technology. In a back-illuminated CCD, the CCD device has been thinned down with etching techniques to 10-15 μm thickness, and the light falls directly onto the photosensitive area of the CCD (depletion region), where there is no gate structure. The camera has a 16-bit digitalization of the signal, which gives a dynamic range of 65,535 : 1 or 96 dB.

The camera exhibits very low noise characteristics. Random electron excitation registered as counts is called the dark current. The iKon camera has a dark current of $0.017 e^-/\text{pixel}/\text{s}$ at -80°C , which for a typical exposure time of 100 μs and an operation temperature of -80°C accounts for $10^{-6} e^-/\text{pixel}$. Digitization noise is introduced when the analog signal on the detector is rounded off to the nearby integer value of the available discrete steps. The error introduced by digitization thus depends on the number of available discrete steps. Usually, digitization noise is negligible compared to Poisson noise. The iKon camera has a 16-bit analog-to-digital with $2^{16} = 65,535$ discrete steps available. If we use that to convert a full well ($100,000e^-$), each step corresponds to $1.5e^-$ at the full well scale (maximum scale). For a typical operation, where we allow a 50% filling of each well, the Poisson noise is $\sqrt{50,000} = 223 e^-$ exceeding the digitization noise by far.

4.5.2 The imaging system

The imaging system has a typical layout of a system used for absorption imaging with the addition of a Fourier filter in the Fourier plane of the first collection lens. Fourier filtering techniques are discussed in Chapter 3. The Fourier filter in our case is an opaque spot called "dark spot", which blocks the unabsorbed light from the probe beam. Diffractive dark-ground imaging, the imaging technique used in our setup, is a special case of Fourier filtering imaging that uses resonant probe light and an opaque filter.

The imaging system is illustrated in Figure. The probe light is tuned to the $|F = 2\rangle \rightarrow |F' = 3\rangle$ transition and it is spatially filtered and delivered by means of a single-mode polarization-preserving optical fiber. The light from the fiber is collimated by a fiber collimator (Schäfter & Kirchoff FC60-4-M5-10), and the collimated beam has an $1/e^2$ diameter of 1.08 mm. The intensity of the imaging beam is $70 \mu\text{W}/\text{cm}^2$. The collimated beam illuminates the cloud of the trapped atoms of a typical diameter of 20 μm . The imaging beam is sent for a short pulse 100 μs , and during that time some part of the light is absorbed by the atoms, thus diffraction of the imaging beam occurs. After the probe beam has been diffracted on the atom cloud, the light is collected by the relay objective. The relay objective consists of two identical sets of lenses with identical focal length f ($4f$ -configuration). The $4f$ -configuration allows us to have the Fourier transform of the image in the center of the $4f$ -configuration (Fourier plane of the first lens), where we place the dark spot. The dark spot blocks the unabsorbed part of the light of the imaging beam without affecting the image of

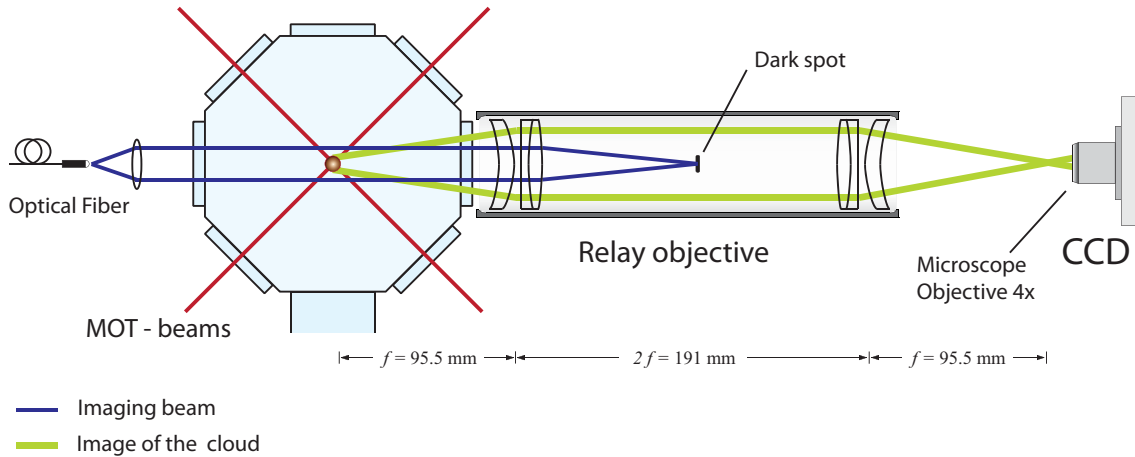


Figure 4.13: Imaging system layout for diffractive dark-ground imaging. The imaging beam is collimated to an $1/e^2$ diameter of 1.08 mm and illuminates the trapped atom cloud of a typical diameter of $30 \mu\text{m}$. After diffraction of the imaging beam on the atom cloud, the light is collected by the relay objective. The lower spatial frequencies of the imaging beam are blocked by the dark spot at the Fourier plane of the first lens. The higher spatial frequencies created by the diffraction of the imaging beam on the atom cloud are unaffected by the dark spot filter, thus an image of the atom cloud is formed onto the CCD camera. The image of the cloud is magnified by 4x using a standard microscope objective.

the atom cloud. The relayed image of the atom cloud is magnified by a standard 4x microscope objective (Edmund Optics) and focused onto the CCD. Since the pixel size of the CCD is $13 \mu\text{m}$, a magnification of 4x means that each pixel corresponds to $3.25 \mu\text{m}$ at the plane of the atoms.

Each of the two identical sets of lenses that make up the relay objective consists of an achromatic doublet with a companion meniscus forming a triplet [42]. The triplet set has a focal length of $f = 95.5 \text{ mm}$ and an effective diameter of 29 mm giving a numerical aperture of $NA = 0.15$. The lenses are anti-reflection coated at 780 nm and are made by Melles-Griot.

The dark spot is a thin opaque disk made of Chrome-LRC with a diameter of $200 \mu\text{m}$. It has an optical density of $D > 4$ and a reflectivity of $R < 15\%$. The dark spot sits in the center of a 30 mm diameter glass disk, which is anti-reflection coated at 780 nm. The glass disk has a thickness of 2 mm and the dark spot a thickness of $\approx 0.2 \text{ mm}$. The glass disk is used as a means to hold the dark spot onto the plastic housing used for the optics of the relay objective.

The two triplet sets of the relay objective and the glass disk with the dark spot on it are encased inside a plastic housing [42]. The housing consists of three sections, with the two end-sections each holding one of the triplets and the middle-section holding the dark spot. The three sections can be screwed together to adjust the relative position of the triplets. The focusing of the internal parts of the relay

objective is carried out independently of the rest of the imaging system. Once the internal parts have been focused, the relay objective can be integrated as a solid unit to the rest of the imaging system.

The relay objective is then focused to the microscope objective and the camera, and the whole imaging system is mounted on a small separate optical board. The optical board is mounted on XYZ translation stages. This allows us to focus the whole imaging system with respect to atoms, and also move the imaging system in the transverse direction to place the image of the atom cloud on a certain region on the CCD chip. The optical fiber and the collimating lens for the imaging beam also sit on XY translation stages, which allows movement in the transverse direction to align the imaging beam with the atom cloud and the dark spot at the same time.

The optical resolution of the imaging system was measured by a positive resolution target USAF 1951. The resolution of the relay objective was found to be $6.2 \mu\text{m}$. The presence of the microscope objective though limits the optical resolution to $9 \mu\text{m}$, and also results in an overall numerical aperture of the imaging system of $NA = 0.1$.

Fluorescence Imaging

In our experiments we also employ fluorescence imaging as a means to detect the atoms and measure the atom number. For fluorescence imaging, the same optical setup with the relay objective and the CCD camera is used. The fluorescence emitted by the trapped atoms is collected by the relay objective and a relayed image is formed. The relayed image is magnified by the microscope objective and focused onto the CCD. The probe beam is switched off during fluorescence imaging. From the fluorescence emitted by the atom in a 4π solid angle only a fraction of is collected according to the solid angle subtended to the first collection lens $\pi(d/2)^2/f^2$, where d is the diameter and f the focal length of the lens. The fluorescence collected by the relay objective is collimated by the first lens with a diameter of 29 mm, thus the dark spot having a diameter of $200 \mu\text{m}$ has a negligible effect on the collected fluorescence.

4.5.3 Auxiliary detection system

In our setup we have included an auxiliary detection system using a single-photon counting module (SPCM). The main purpose of the auxiliary detection system is to provide us with continuous monitoring of the MOT at all times, while we were performing the low-atom imaging experiments using fluorescence imaging and diffractive dark-ground imaging.

The single-photon counting module (PerkinElmer, SPCM-AQR-14) utilizes an avalanche photodiode with 50% detection efficiency at 780 nm and $0.1 \mu\text{s}$ time resolution. The diode is thermoelectrically cooled and temperature stabilized. The SPCM has a dark count rate of < 100 counts/s. The photon counts collected within the gate time are added up and the output signal is integrated over time using

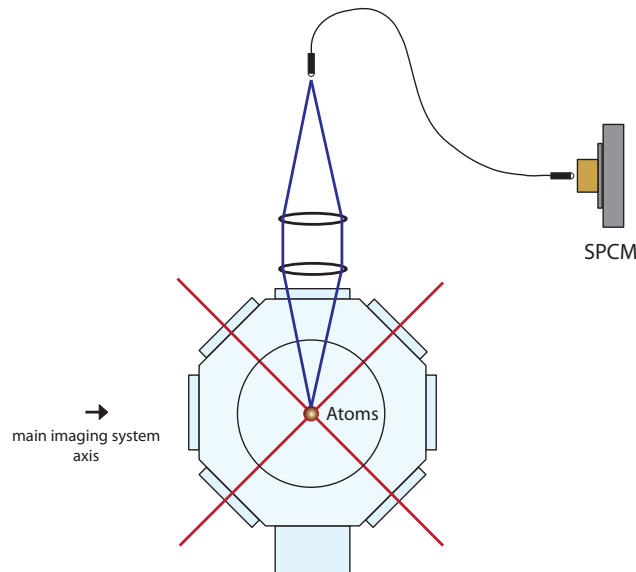


Figure 4.14: Auxiliary detection system. Fluorescence light from the atoms is collected with a set of standard lenses and coupled onto a fiber. The output of the fiber is coupled to the photodiode of a single-photon counting module.

Labview. We use a gating time of 10 ms, which is enough for having a good time resolution of the MOT.

The fluorescence of the atoms is used for monitoring the MOT with the SPCM. The fluorescence is collected by an objective of two identical lenses, coupled into a fiber and send to the detector. The optical axis of the objective lies perpendicular to the optical axis of the optics and the camera of the main imaging system. The two lenses have a diameter of 25.4 mm and a focal length of 40 mm. The fluorescence light collected by the solid angle of the first lens is collimated and coupled by the second lens to a multi-mode 100 μm core optical fiber. The other end of the fiber is coupled to the SPCM detector. The diameter of the fiber core was chosen so that to avoid any losses due to mismatch of the fiber core with the active area of the photodiode.

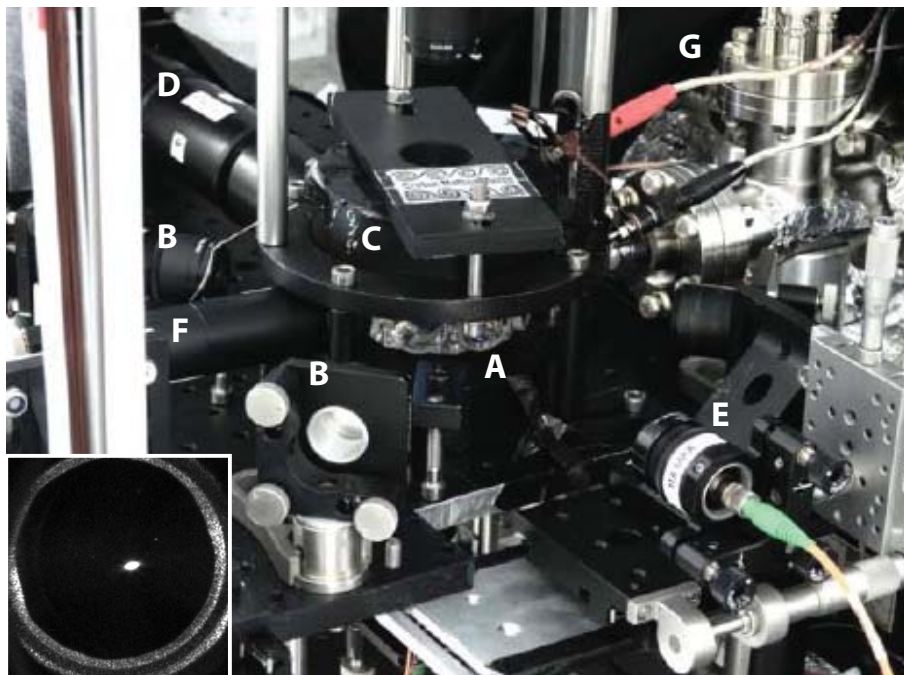


Figure 4.15: Picture of the setup. On the picture one can see the glass cell (A), the trapping beams (B), the coils (C), the relay objective (D), the imaging beam (E), the auxiliary optics (F) and part of the vacuum system (G). In the insert to the bottom left there is a picture of the MOT.

Chapter 5

Fluorescence Imaging of a Single Atom

The high localization of cold single atoms in tightly confining traps has been of increasing interest in the last few years. Considerable work has been achieved on the quantum interaction of single particles ranging from triggered single photon source [8] and single photon –single atom entanglement [9, 10] to single atom strings in a lattice as a quantum register [66].

Since the observation of the fluorescence emitted by a single atom in a MOT [15], fluorescence detection has been used as a useful detection tool at low atom numbers. Fluorescence imaging down to single atom levels has been implemented as a means for monitoring the presence of single atoms in a tightly focused dipole trap [67], and on individual sites of an optical lattice [66, 68]. Fluorescence imaging of atoms falling through a light sheet has been implemented with single atom resolution [69].

In this chapter, we implement fluorescence imaging on a high-gradient MOT to observe atom clouds of very low atom numbers down to a single atom. The collected fluorescence is observed in time, where steps in the level of the fluorescence are recorded denoting the entry and exit of individual atoms in the trap. The statistics of the collected fluorescence are also observed, where the presence of individual atoms is denoted by discrete peaks on the corresponding histogram of the collected counts.

The recording of the counts for a single atom enables us to calibrate the count level of a single atom and extract atom number directly from fluorescence images of larger atom numbers. The fluorescence images are then used as a reference for the atom number measured by the diffractive dark-ground imaging technique in the next chapter (Chapter 6).

5.1 Fluorescence imaging of trapped single atoms with the CCD

We employ fluorescence imaging using the CCD camera and the setup on Fig. 4.13 to image trapped atom clouds of a few atoms down to a single atom.

The imaging beam is switched off during fluorescence imaging. The fluorescence emitted by the trapped atom cloud is collected by the relay objective, magnified by a 4x microscope objective and refocused onto the CCD. To observe the fluctuations of atoms in a low-atom number trap, a series of images is taken over a large period of time with the CCD operated at a fast readout rate (2.5 kHz) at an exposure time of $\tau_{\text{exp}} = 0.5$ s.

The fluorescence emitted by a single atom within a time interval τ is $R_{\text{sc}}\tau$, where R_{sc} is the photon scattering rate given in Eq. 2.2. The photons are spontaneously emitted within a solid angle of 4π , whereas the photons collected are those within the solid angle Ω of the cone defined by the first collection lens given by

$$\Omega = 2\pi(1 - \cos \theta), \quad (5.1)$$

where $2\theta = 2 \tan^{-1}(d/(2f))$ is the apparent angle of the lens with focal length f and diameter d . Therefore, the collection efficiency is $\Omega/(4\pi)$, which for the relay objective with $d = 29$ mm and $f = 95.5$ mm is 0.6%. The presence of the microscope objective results in an overall numerical aperture of $NA = 0.1$, which gives ($NA = \sin \theta$) an overall collection efficiency of 0.25%. The quantum efficiency of the camera is 95% at the 780 nm wavelength.

The trapping beams of the MOT have an $1/e^2$ diameter of 3 mm. The saturation parameter for each beam is $s = 5$ for an overall power in the MOT of 8 mW. The small diameter of the beams reduces the light scattering on the vacuum glass cell. It also results in a smaller trapping area A and a smaller capture rate (Eq. 2.29) suitable for having low atom number clouds in the MOT.

In order to have low atom number clouds, a low rubidium pressure n_{Rb} is required. The getter source is switched on for a short time (about 5 s) to insert rubidium atoms in the cell. After several seconds the transient expires, and the result is a low constant rubidium pressure in the cell. The fluorescence of the untrapped rubidium atoms is monitored by the avalanche photo diode, which provides us with an indication to the presence of rubidium atoms in the cell at all times.

Having a low rubidium pressure and a small diameter for the trapping beams already results in low-atom number clouds. To further reduce the atom number down to a few atoms, we decrease the detuning from $\delta = -2\Gamma$ typically used for a large atom number MOT down to $\delta = -\Gamma$, i.e. we bring the trapping light closer to the resonance of the transition. The detuning affects the capture velocity $v_c = \pm\delta/k$, thus a smaller detuning results in a reduced capture rate $R \propto v_c^4$ (Eq. 2.29), which cuts down significantly on the number of atoms in the trap.

We also use a high magnetic field of 75 G/cm, which affects the effective detuning (Eq. 2.23) and results in a smaller capturing area and a reduced capture rate. A high magnetic field gradient also results in a tighter confinement of the atoms in the

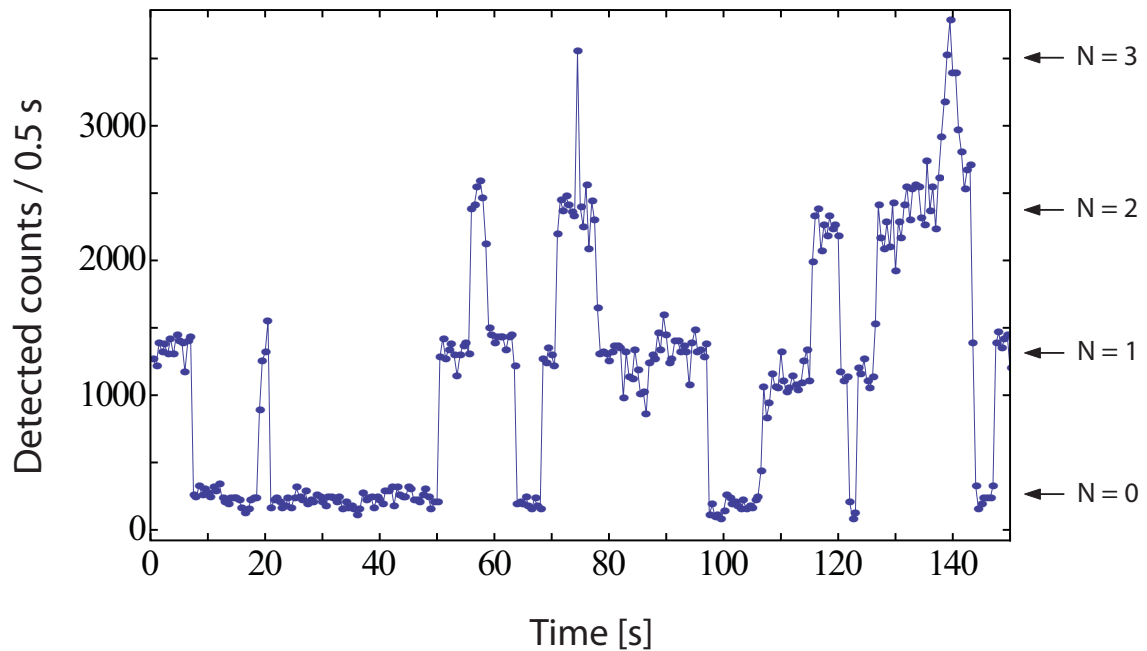


Figure 5.1: Fluorescence level fluctuations over time in a low-atom number MOT with the CCD Camera. Each point corresponds to the total counts from a single fluorescence image taken with the CCD at 0.5 s exposure time. The fluorescence images are fitted with a Gaussian and integrated to extract the total number of counts. The fluorescence emitted by the trapped atoms over time exhibits discrete steps. The first step above the background level ($N=0$) is associated with a single atom ($N=1$) present in the trap.

trap and in atom clouds of smaller sizes. Having tightly confining traps is favorable for imaging of low signals, since the imaged light is concentrated within fewer pixels on the CCD thus increasing the signal to noise ratio (SNR).

By adjusting the parameters of the trap described above we are able to reduce the number of trapped atoms in the MOT and detect with fluorescence imaging the presence of a few atoms in the trap down to a single atom. Fluorescence images are taken with the CCD with an exposure time of 0.5 s. Each of the images is fitted with a Gaussian with an offset to account for the background. The Gaussian fit above the offset is integrated to extract the total number of counts. The total counts is proportional to the fluorescence emitted by the atoms and thus to the number of atoms in the trap. Therefore, the observation of the fluorescence level over time reveals the changes in the atom number in the trap. To observe the fluorescence of the trap over time, a large number of successive fluorescence images are taken over a period of time with an interval of 0.5 s between the images, and the total counts of each image is plotted over time (Fig. 5.1).

For a low atom number MOT, the fluorescence exhibits discrete steps, which is associated with individual atoms being captured or lost from the trap [15]. The

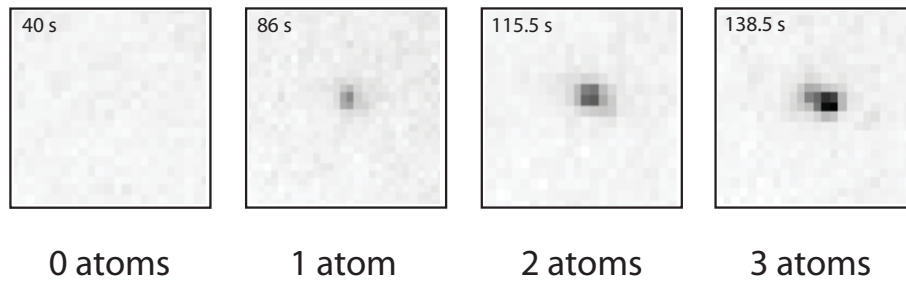


Figure 5.2: Fluorescence images of a MOT of very low atoms numbers. The pictures are time frames of the data set in Fig. 5.1. On the top left corner the time is noted at which the frames were taken.

steps appear above a certain background level, which is associated with the scattered light on the vacuum cell and the optics. The background level is identified at the absence of atoms by having the trap switched off. The level of the first step above the background is associated with the presence of a single atom in the MOT.

Figure 5.2 shows a small sample of fluorescence images that constitute the bigger sample of Fig. 5.1. The atom density in a fully loaded MOT (below the radiation limit) follows a Gaussian distribution. For a low atom number MOT, due to the atoms motion within the trapping region, the average position of an atom is imaged. The mean $1/e$ diameter of the images of low atom numbers in the MOT is found $10 \mu\text{m}$, greater than the resolution of the optics of $9 \mu\text{m}$.

In the histogram of Fig. 5.3 the total counts extracted from each of the fluorescence images is plotted against the frequency of occurrence of each value within the total sample. The occurrence of the values for the total counts exhibits discrete peaks, which correspond to the discrete levels of fluorescence emitted by individual atoms in the trap. The first peak of the histogram corresponds to the background level ($N=0$), the second peak corresponds to a single atom ($N=1$) in the trap, the next peak to two atoms ($N=2$) in the trap and so on.

The peaks corresponding to one ($N=1$) and two ($N=2$) atoms are fitted with a Gaussian each. The mean value of the fit for each peak is taken as the mean total detected counts for the corresponding number of atoms. The mean values of the peaks (also taking into account the mean of the peak of the background ($N=0$) equal to zero) have equal distances denoting that each individual atom emits the same amount of fluorescence, and each additional atom in the trap increases the detected fluorescence level by equal amount for a low-atom number MOT.

The mean of the fit to the peak corresponding to a single atom ($N=1$) is taken to be the count level for a single atom, which is used for the normalization of the fluorescence images. The detected number of counts for a single atom is found to be 2200 counts/atom/s with a standard deviation of $\pm 12\%$ (taken from the histogram for an exposure 0.5 s). The photons emitted spontaneously by an atom follow Poissonian statistics, which for a mean value of 1100 counts/atom/0.5 s corresponds to $\pm 3\%$ error. The extra broadening of the peak that is visible on the histogram is due

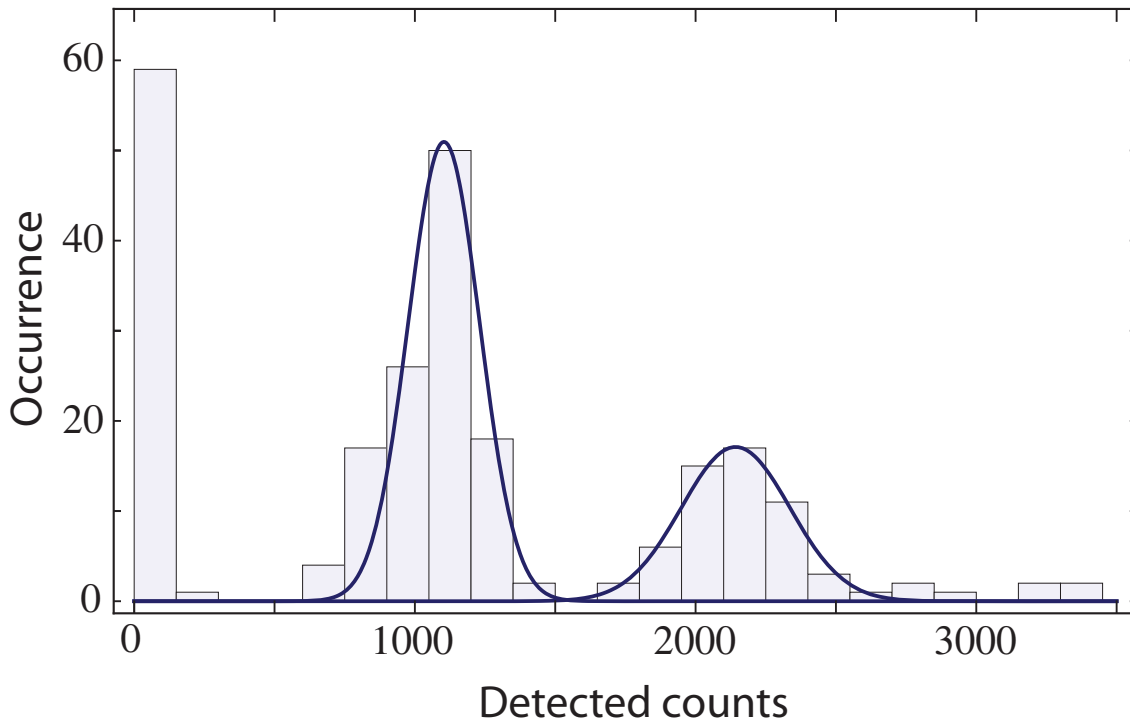


Figure 5.3: Histogram of the frequency of occurrence of total counts from a series of successive fluorescence images of a low-atom number MOT. The sample consists of 300 images at 0.5 s exposure time each. The first peak of the histogram corresponds to the background level ($N=0$), the second peak corresponds to a single atom ($N=1$), the next peak to two atoms ($N=2$). The mean of the fit with a Gaussian to the peak of $N=1$, which coincides with the most probable value of the peak, is taken to be the count level for a single atom, which is used for the normalization of the fluorescence images. The standard deviation is $\pm 12\%$.

to fluctuations in the emitted fluorescence from fluctuations in the laser power, and due to the temporal resolution of 0.5 s of the images.

The normalization of the fluorescence images with the single atom level of counts enables us to extract the atom number directly, for fluorescence images of higher atom numbers with a standard error of $\pm 12\%$. Fluorescence images with the atom number extracted in that way are used as a reference to compare the atom number measured with the diffractive dark-ground technique in Chapter 6.

5.2 Lifetime of single atoms in the MOT

The losses due to elastic collisions with background particles discussed in Sec. 2.4 is the prime loss mechanism in the MOT and results in the ejection from the trap of one atom per collision. The background collision loss rate determines the lifetime of individual atoms, which is expected to be in the same order of magnitude with the time constant $\tau = 14$ s extracted from the loading curve in Sec. 2.3. The capture rate

R determines the mean time between two successive jumps in the fluorescence, i.e. between two atoms being captured successively (Eq. 2.41). For the low-atom number MOT of the experiment with a magnetic field gradient of 75 G/cm, a detuning of $\delta = -\Gamma$ and a pressure of $P_{\text{Rb}} \approx 10^{-14}$ mbar the capture rate (Eq. 2.29) is estimated equal to $R = 0.15$ at./s .

The fact that the capture rate of the MOT at the regime of low-atom numbers is of the order of 0.1 at./s is in accordance with the fact that the fluorescence of single atom loaded in the trap exhibits discrete steps. At higher capture rates typical for a high atom number MOT the atoms are loaded much faster in time resulting in a smooth loading curve for the fluorescence. Since the prime loss mechanism results in one lost atom per collision, one step down in the fluorescence corresponds to one individual atom being lost from the trap. Two-atom recombination losses have also been observed as a decrease in the fluorescence level of twice the size of a single step.

In order to have a measurement for the lifetime of single atoms, we observe series of fluorescence steps for a long period of time. From these long data sets, we do a statistical analysis of all the duration times of individual steps τ'_{on} , which follow an exponential distribution. We take the mean value of the distribution τ_{on} as the measured lifetime for individual atoms in the trap.

The fluorescence level of the MOT is directly observed with the avalanche photo-diode (referred to as single-photon counting module in Sec. 4.5.3), which provides with a reading of the fluorescence signal versus time immediately and is suitable for long time measurements. The collection optics for the photo-diode have a numerical aperture of $NA = 0.3$, which accounts for a collection efficiency of 2.3%. The quantum efficiency of the photo-diode is 60% at 780 nm. A typical reading of low-atom number steps with the avalanche photo-diode is shown on Fig. 5.4. The frame depicted there is part of a much larger measurement. The level of detected counts for a single atom was found 4000 counts/atom/s.

From the long data sets taken with the avalanche photo diode, all the duration times τ'_{on} of the individual steps are plotted on a histogram (Fig. 5.5). The distribution of the duration times of the steps is expected to be exponential since the decay process for a large atom number MOT (Eq. 2.38) is exponential. The histogram is fitted with an exponential distribution curve, and the mean of the curve $\tau_{\text{on}} = 9.5$ s is the measured lifetime for individual atoms in the trap. The measured lifetime for single atoms is of the same order of magnitude with the time constant $\tau = 14$ s extracted from the loading curve of a high capacity MOT (Sec. 2.3). The theoretical estimation of the lifetime of single atoms using Eq. 2.39 for a rubidium partial pressure of 10^{-14} mbar (Eq. 2.33) and an overall background pressure of 2×10^{-11} mbar results in an estimated lifetime of the order of ~ 200 s. The much lower lifetime measured in the trap is attributed to two-body light-assisted collisions limiting the lifetime to the order of 10 s. Taking two-body losses into account, Eq. 2.40 with $\beta \simeq 3.3 \times 10^{-12}$ cm³/s (Sec. 2.4.2), a constant volume $V = \pi^{3/2}\sigma^3$ in the range of single atoms, and σ the radius of the cloud (Fig. 5.2) results in a lifetime of $\simeq 50$ s for $N = 2$ atoms in the trap and in a lifetime of 15 s for $N = 5$ atoms in the trap. The later estimations for the lifetime are in better agreement with the measured

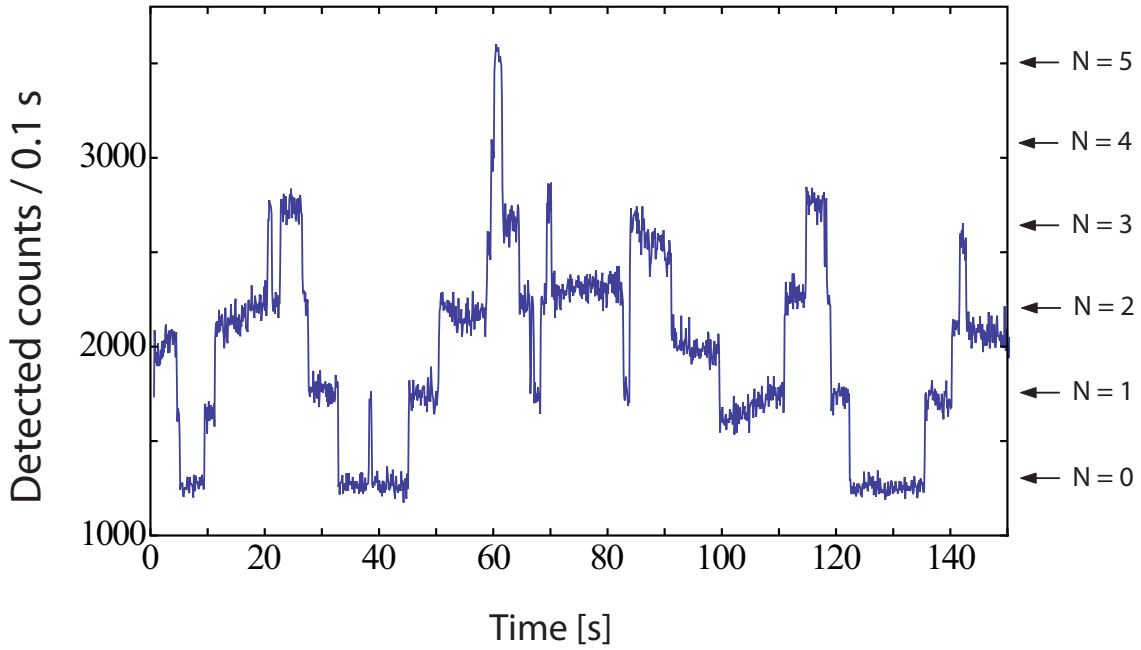


Figure 5.4: Fluorescence level fluctuations over time in a low-atom number MOT using the avalanche photo-diode (SPCM). The measurement is performed at a gate time of 100 ms. Atom numbers of up to five atoms ($N=5$) can be observed. This figure shows a frame of a much larger measurement.

lifetime $\tau_{\text{on}} = 9.5$ s for a MOT of an atom number between $N = 0$ and $N = 5$ atoms.

In an analogous fashion, a histogram is constructed with all the times τ'_c between a capturing of an individual atom event to the next. The histogram (Fig. 5.6) is fitted with an exponential distribution curve. The capture rate deduced from the mean of the curve is $R=0.21$ at./s, which is in agreement with the theoretical estimation for a rubidium partial pressure of 10^{-14} mbar equal to 0.15 at./s.

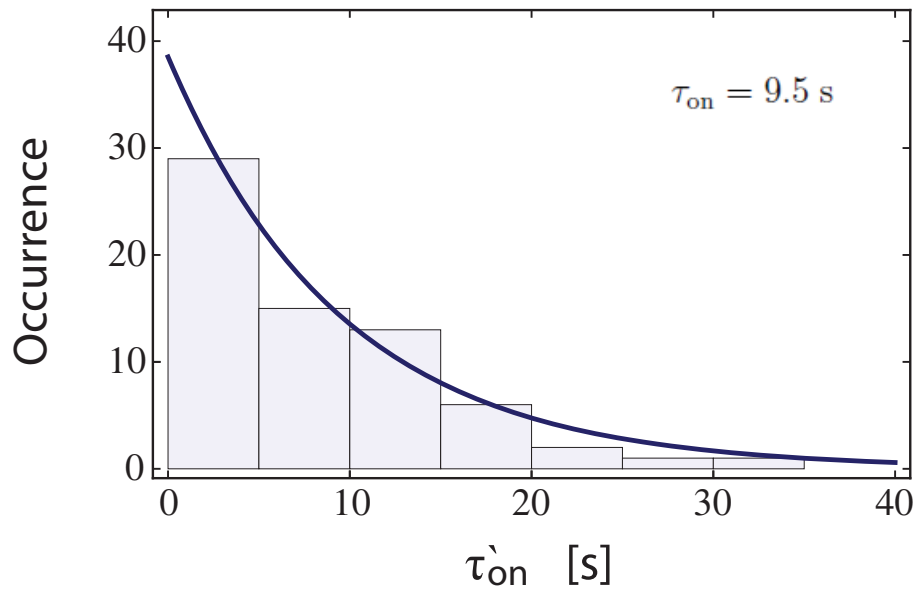


Figure 5.5: Histogram of the duration times τ'_{on} of individual steps. The histogram is fitted with an exponential distribution curve. The mean of the curve $\tau_{on} = 9.5 \text{ s}$ is the lifetime for individual atoms.

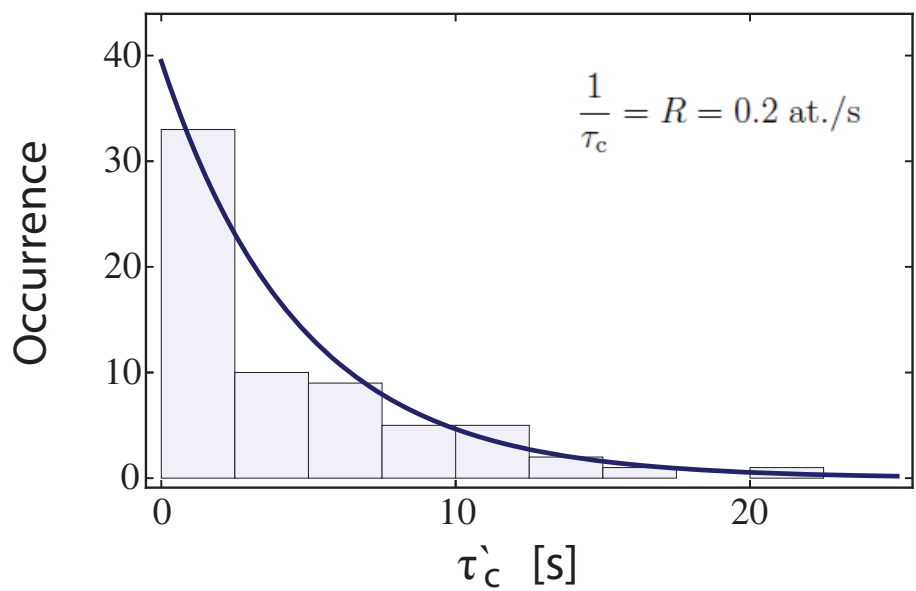


Figure 5.6: Histogram of the times τ'_c between a capturing of an individual atom event to the next. The histogram is fitted with an exponential distribution curve. The capture rate deduced from the mean is $R=0.21 \text{ at./s}$.

Chapter 6

Diffractive Dark-Ground Imaging of Low-Atom Clouds

Absorption imaging is the main tool for extracting information about a cold atomic sample. Diffractive dark-ground or "dark-field" imaging is based on resonant absorption imaging with the addition of the opaque Fourier-filter (dark spot) with the aim to achieve high sensitivity by suppressing the background of the probe light. Resonant absorption imaging with an opaque Fourier-filter has been cited in [70], where it has been implemented to image a BEC of 100 atoms. In this work we have implemented diffractive dark-ground imaging as a sensitive technique to image atom clouds of very low optical densities. With this method we have been able to resolve optical densities of the order of 0.01 down to 100 atoms for a freely expanding atom cloud prepared in a MOT [71], and down to 7 atoms for a tightly confined ultra-cold atomic sample in a BEC setup [72].

Post processing in absorption imaging involving fringe-removal algorithm and most probable estimation of atom number has also been demonstrated as a means to increase the sensitivity of classical absorption imaging with a resolution down to a few tens of atoms [73].

6.1 Alignment of the imaging optics

We use the setup on Fig. 4.13 for diffractive dark-ground imaging. The relay objective is brought into focus with the rest of the imaging system, the microscope objective and the CCD camera, by illuminating a resolution target with a laser beam. We use a USAF resolution target (Fig. 6.1) for measuring the resolution of the imaging system, as well as a target for focusing the relay objective to the camera-microscope and for checking the magnification. The resolution of the imaging system was found $8.5 \mu\text{m}$.

The whole imaging system mounted on XYZ translation stages, is focused as a whole to the location of the atom cloud by observing the fluorescence of the atom cloud with the CCD. The imaging beam, which also in mounted on XY translation stages, is observed with the CCD (Fig. 6.2(a)) and is aligned for its center to

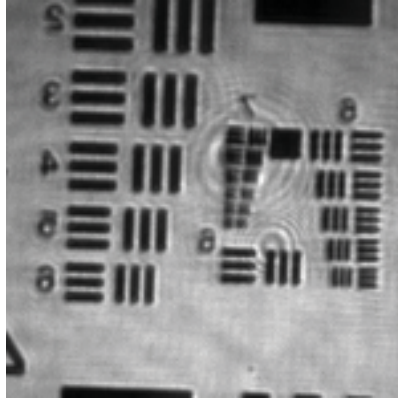


Figure 6.1: Resolution target used to test the resolution of the imaging system. The overall resolution of the system was found $8.5 \mu\text{m}$.

coincide with the atom cloud. The imaging beam is aligned to the $200 \mu\text{m}$ dark spot by tilting slightly the relay objective. Even by having a coarse alignment of the imaging beam to the dark spot, there is a significant drop in the observed intensity of the imaging beam. To fine tune the alignment with the dark spot, we replace temporarily the microscope objective at the CCD with a custom made objective that has its focus on the plane of the dark spot (Fig. 6.2(b)). Since the focus of the imaging beam is very intense, in order to be able to observe the filtering plane, the focus of the beam has to be at least partially covered by the dark spot. By performing small adjustments to the position of the focus of the imaging beam with respect to the dark spot, we further improve the extinction of the imaging light.

We switch back to the plane of the camera to observe the residual background from the blocked beam (Fig. 6.2(c)). The structure in the background is caused by the diffraction of the imaging light on small dust particles and by the interference between various optical components. The fluctuations between the minima and maxima in the structured background display a standard deviation of 30% from the mean of the background over a large area (almost the entire imaging area). The typical size of the atom cloud is about $30 \mu\text{m}$ in diameter, therefore the images in the experiment are taken within an $80 \times 80 \mu\text{m}$ window at the position of the atoms. The reference images are taken within the same window. For the background in the $80 \times 80 \mu\text{m}$ window of the images we find a standard deviation of 36%, which is an indication that the fluctuations in the structure in the small window are distributed similarly to the entire area.

The ratio of extinction is measured by taking a reference image at the position of the atoms with a $80 \times 80 \mu\text{m}$ window. By tilting the relay objective slightly, the imaging beam is uncovered from the dark spot, and we are able to take an image of the unblocked beam at the same position. The mean of the reference image and the mean of the image of the unblocked beam are used to measure the ratio of extinction (Eq. 3.35), which for our setup is found to be about 800.

The position of the fluctuations in the background are also moving with time due to mechanical vibrations, which causes a fluctuation in the mean value extracted

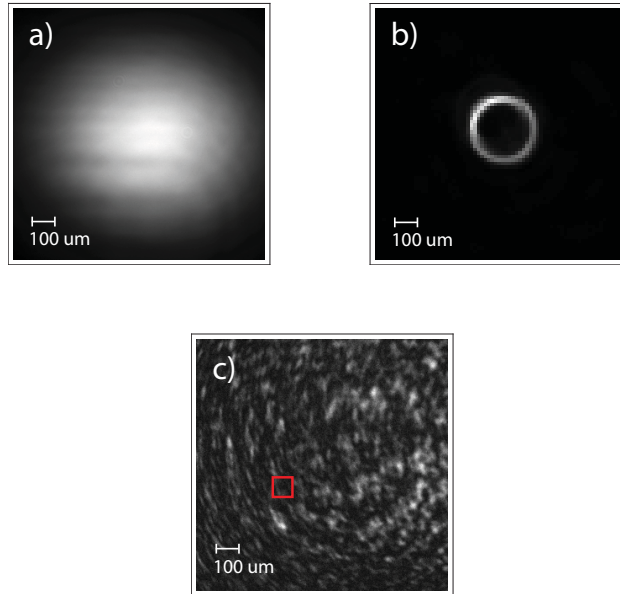


Figure 6.2: (a) Imaging beam profile at the plane of the CCD. The beam size is $2w_0 = 1$ mm. (b) Image of the $200 \mu\text{m}$ dark spot at the plane of the Fourier filtering. The focus of the imaging beam is blocked by the dark spot. (c) Image of the residual background at the plane of the camera with the imaging beam blocked. The red square is showing the typical area ($80 \times 80 \mu\text{m}$) used for the images of atoms and the reference images. The typical size of the atom cloud is about $30 \mu\text{m}$ in diameter.

using only a small window from the imaging area like that of $80 \times 80 \mu\text{m}$. From a large number of background images taken of an $80 \times 80 \mu\text{m}$ window at the same spot of the CCD at the position of the atoms, we observe fluctuations in the mean background of the images with a standard deviation of 18%. This results through Eq. 3.19 in an uncertainty of $\simeq \pm 9\%$ for the atom number measured with diffractive dark-ground imaging.

6.2 Sequence of the experiment

The procedure for the dark-ground imaging experiment commences by first taking a fluorescence image of the trap with an exposure time of 0.5 s. During the fluorescence imaging the imaging beam is switched off. Directly after the fluorescence image, the trap is switched off, and at the same time the imaging beam is switched on in order to take a dark-ground image with an illumination time of $\tau = 100 \mu\text{s}$. The switching of the trapping beams and the imaging beam is controlled by AOMs, which have a switching time of $5 \mu\text{s}$. A reference image is acquired in the absence of atoms $400 \mu\text{s}$ after the dark-ground image.

In order to remove the structure of the background from the dark-ground images with the atoms, we subtract the reference image from the corresponding dark-ground

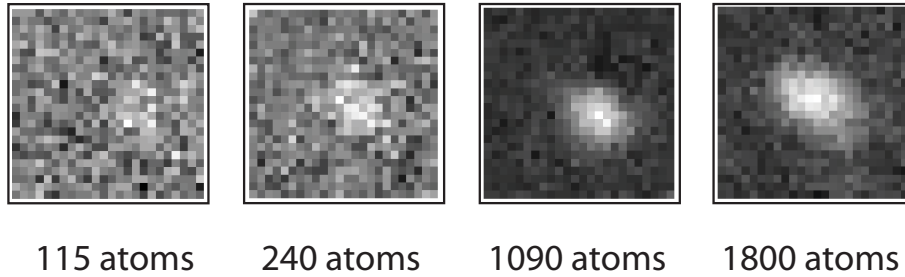


Figure 6.3: Diffractive dark-ground images for various atom numbers, where the reference image has been subtracted from the raw CCD image. The window of the images corresponds to an $80 \times 80 \mu\text{m}$ area at the plane of the atoms. The images were taken with an illumination time of $100 \mu\text{s}$.

image. To reduce the effect of the structure of the background moving in time, we choose a small interval of $400 \mu\text{s}$ between the reference and the main image. For that purpose fast-kinetics mode of the camera was implemented enabling for a time of $400 \mu\text{s}$ between the reference and the main image. In fast-kinetics mode, only a small portion of the CCD chip is used for imaging, while the rest of the rows of the chip are used for storing the acquired data. The part of the CCD used for storing the data is covered with a $200 \mu\text{m}$ width slit, which accounts for an active area of about 60 rows on the CCD chip. During a series of images taken at fast-kinetics mode, the data of each of the images are shifted successively in rows to the part of the CCD not used for imaging, where they are stored. The data is read-out once at the end when the CCD chip is full, which reduces the minimum required time between two successive images. The time between two images is limited by the shift speed ($5.775 \mu\text{s}$ per row) and the width of the active area of the CCD. The interval of $400 \mu\text{s}$ was also limited by the requirement that there should be enough time for the atom cloud to dissipate after the trap has been switched off before taking the reference image.

6.3 Imaging atom clouds with diffractive dark-ground imaging

Each run of the experiment consists of taking three images, a fluorescence image, the diffractive image with the atoms and a reference image. The fluorescence image is used separately from the diffractive image as a secondary method for measuring atom numbers. The fluorescence image is fitted with a Gaussian and integrated in order to extract the total counts. The calibrated number of counts for the single atom level extracted from a histogram like the one shown on Fig. 5.3 is used to directly extract the atom number from the fluorescence image. We use the atom number from the fluorescence imaging to compare it with atom number extracted using diffractive dark-ground imaging.

For the dark-ground images, the residual background from the imaging beam,

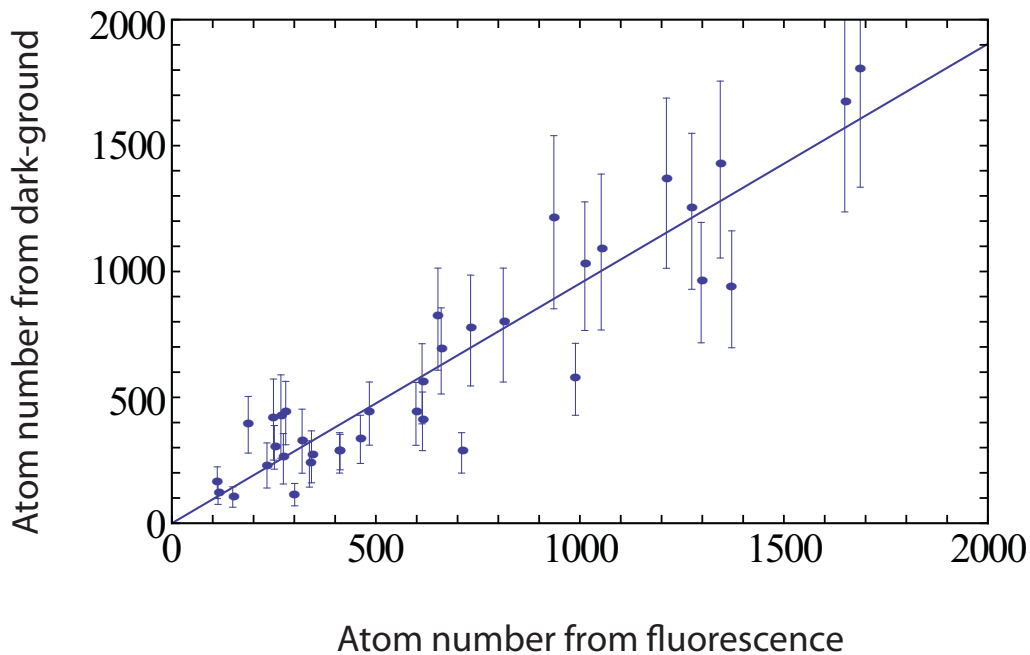


Figure 6.4: Atom number measured with the diffractive dark-ground imaging technique. Each data point is plotted against the atom number of the corresponding fluorescence image taken in the same experimental run. The fitted straight line has a slope of 0.95 and a standard error of $\pm 12\%$ due to an overall uncertainty in the atom number determination using fluorescence imaging. The error bars in the atom number determination using dark-ground imaging include the uncertainty due to the fluctuations in the mean level of the reference image, and the fluctuations in the size of the trapped cloud. The data points display a dispersion around the fitted line of $\pm 35\%$.

caused by diffraction on dust particles and by the interference between various optical components, adds non-coherently to the detected light from the diffraction on the atoms. That means that the two light fields, the background and the light from the atoms, have an arbitrary relative phase ϕ . Thus, we treat each of the diffractive images by subtracting their corresponding reference image as $I_{\text{dg}} = I_{\text{atoms}} - I_{\text{ref}}$. Figure 6.3 shows a selection of diffractive dark-ground images for various atom numbers, where the reference image has been subtracted from the raw CCD image.

$$n = -\frac{1}{\sigma} \ln \left[\left(1 - \sqrt{\frac{I_{\text{dg}}}{I_0}} \right)^2 \right], \quad (6.1)$$

From the subtracted images I_{dg} we calculate the atom number using Eq. 3.19, which is written here for convenience (Eq. 6.1). The equation is applied to the whole image I_{dg} , which transforms the initial image of the intensity to an image of the atom density. The transformed image is fitted with a Gaussian and integrated to extract

the total number of atoms. The intensity I_0 of the unblocked beam is extracted from the mean value of the corresponding reference image multiplied by the extinction ratio. For the scattering cross-section σ we use Eq. 3.20, which is general for strong saturation imaging ($s > 1$). The saturation parameter of the imaging beam for the experiment is $s = 2.5$.

The atom number measured from the diffractive dark-ground images is compared to the atom number from the fluorescence images, which has been extracted using the single atom level calibration. For each diffractive dark-ground image the atom number is compared to the atom number of the corresponding fluorescence image taken in the same experimental run. Figure 6.4 shows a series of experimental runs comparing the atom number from the corresponding fluorescence-diffractive image pairs for an increasing number of atoms [71].

In order to test the linearity of the atom number estimation between the two methods, a straight line is fitted to the data. The slope of the fitted line is 0.95 with a standard error of $\pm 12\%$. The uncertainty in the slope originates from the fact that the fit on the histogram used to derive the single atom level (Fig. 5.3) displays a standard deviation of $\pm 12\%$, which gives an overall uncertainty of $\pm 12\%$ in the atom number measured with fluorescence imaging. The mean values of the reference images used to measure the beam intensity $I_0 = I_{\text{ref}} \cdot r_{\text{ext}}$ display a standard deviation of $\pm 18\%$ (as discussed in Sec. 6.1), which translates through Eq. 6.1 into an uncertainty of $\simeq \pm 9\%$ for the atom number measured with diffractive dark-ground imaging. Due to the motion of the atoms in the trap and due to fluctuations in the power of the trapping beams, there are fluctuations in the size of the trapped cloud that are transferred on the images. The imaged size of the cloud displays an uncertainty of $\simeq \pm 20\%$ in the data set, which through Eq. 3.43 results in an error of $\simeq \pm 20\%$ to the estimated atom number with diffractive dark-ground imaging. The error bars in Fig. 6.4 result from the uncertainty due to the fluctuations in the reference image, and from the fluctuations in the size of the cloud. The data points display a dispersion around the fitted line of $\pm 35\%$.

When the trap is switched off, the atoms fly isotropically with the velocity they have at the time of the switch-off. The thermal velocity for the temperature T_D at the Doppler cooling limit (Eq. 2.17) for rubidium is $v_D = \sqrt{2k_B T_D / M} = 0.16$ m/s. Within the molasses technique lower temperatures are achievable at least one order of magnitude lower than the Doppler limit, which corresponds to a thermal velocity of 0.05 m/s. Within the 100 μs of the imaging time, an atom in the center of the trap moving with the Doppler velocity v_D will travel about 16 μm towards a random direction.

The average $1/e$ radius from the data set of Fig. 6.4 measured with dark-ground imaging is 14 μm . From the fluorescence images taken before each dark-ground image, the average size of a trapped cloud is 15 μm . The slightly greater average size in the fluorescence images possible originates from the motion of the trap center being averaged out within the imaging time of 0.5 s for fluorescence imaging. For the atoms having velocities in the range of v_D , it is possible that the highest velocities occur close to the center of the trap resulting in a free cloud of $\simeq 14$ μm after the

100 μs of dark-ground imaging.

The absorption of photons from the imaging beam during the imaging time causes the atoms to move along the z -axis a distance equal to (Eq. 3.44) $R_{\text{sc}} v_{\text{rec}} \tau^2 = 0.8$ mm. For a cloud with $1/e$ radius of $w_0 = 14$ μm with a Gaussian diffraction pattern when illuminated, the distance induced by the push of the imaging beam is equal to one Rayleigh range $z_{\text{R}} = \pi w_0^2 / \lambda = 0.8$ mm. At distance of one Rayleigh range z_{R} away from its initial position, the cloud is imaged with a size of (Eq. 3.45) $\sqrt{2}w_0$. Therefore, for an initial size of w_0 and a final size of $\sqrt{2}w_0$ after a time of $\tau = 100$ μs , the cloud is imaged with an average size of $(1 + \sqrt{2})/2w_0$, which is a factor of 1.2 increase from the initial size at the focus. The expansion of the cloud size during the imaging time results in an underestimation error in the evaluation of the number of atoms according to Eq. 3.43. Although longer illumination times τ would result in more photons being absorbed giving a higher signal, the push of the imaging beam along the z -axis results in higher deviations of the cloud size from its value at the focus. For example, for $\tau = 150$ μs the cloud moves a distance about $2.1z_{\text{R}}$, which gives a factor of 1.7 increase in the imaged cloud radius.

During the imaging time $\tau = 100$ μs the imaging beam causes additional thermalization to the cloud due to spontaneous emission. From Equation 3.38 $v = \sqrt{N}\Delta v$ with $N = R_{\text{sc}}\tau$ and $\Delta v = v_{\text{rec}}$, the atoms will have a velocity at the end of the imaging time of $\simeq 0.21$ m/s, comparable to the Doppler velocity, and the atoms will move at that range of velocities after that point in time. At the end of each dark-ground image, there is a 400 μs pause for the atom cloud to dissipate before taking the reference image. After 400 μs the atoms will have moved about 85 μm , which for an initial cloud radius of 14 μm , accounts for an increase of a factor of 6 in the radius of the cloud. This results in the peak intensity being reduced by a factor of 36 (Eq. 3.40) down to $\approx 2.5\%$ of its initial value, when the reference image is taken giving an overestimation error of 1.3% in the measured atom number.

Figure 6.5(a) shows the total detected counts per atom for a varying illumination time up to 150 μs . The signal per atom is increasing linearly with the illumination time at low illumination times with a slope of 0.73. The increase in the signal with illumination time is limited by the dissipation of the atom cloud in free space and by the push of the probe beam along the z -direction, which presumably makes the signal saturate at higher illumination times. Figure 6.5(b) shows the detected counts per atom for varying saturation parameter of the imaging beam. The diffracted light on the absorbing atom cloud is equal in intensity to the absorption (Eq. 3.34), the fitted curve on Fig. 6.5(b), therefore, has the shape of the saturation curve (Eq. 2.2) for absorption and spontaneous emission.

The expansion of the cloud during the imaging time in the transverse plane due to spontaneous emission can be calculated as $r = \sqrt{N}\Delta r$ (Eq. 3.37). Each spontaneous emission event causes a displacement towards a random direction of $\Delta r = v_{\text{rec}} \Delta t$, where $\Delta t = R_{\text{sc}}^{-1}$ is the time between two successive spontaneous emission events. After $N = R_{\text{sc}}\tau$ photon scattering events within the illumination time τ and for each event causing a displacement of magnitude Δr , the total displacement is $\simeq 15$ nm, which is much smaller than the size of the cloud and the resolution of the optics.

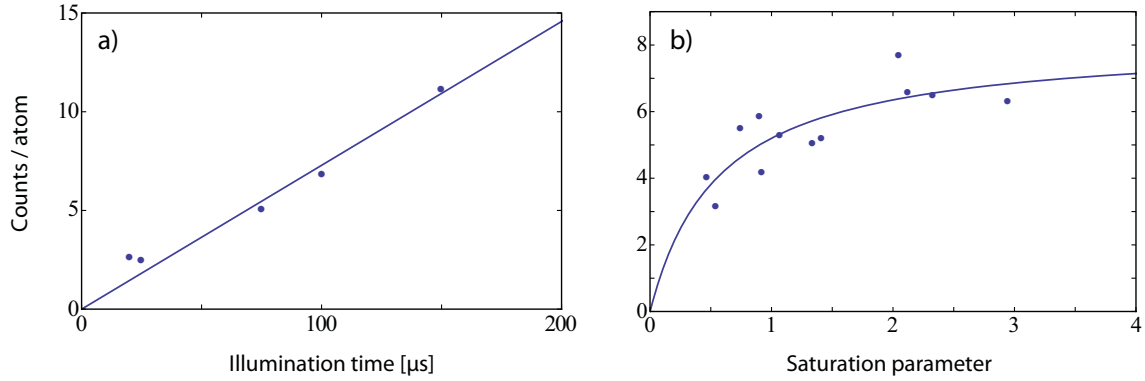


Figure 6.5: The plots are cuts on the imaging parameters space, where the parameters of beam intensity and illumination time have been scanned. (a) Detected counts per atom for a varying illumination time up to $150 \mu\text{s}$. The imaging beam has a saturation parameter of $s=1.25$. (b) Detected counts per atom for a varying intensity of the imaging beam. The illumination time is $75 \mu\text{s}$. The shape of the fitted curve is that of the scattering rate R_{sc} with $\delta = 0$.

The remitted photons from absorption of the imaging light are detected as fluorescence light, which adds non-coherently to the signal from the diffracted light at the plane of the camera. The fluorescence light is emitted towards all directions and is collected with a collection efficiency of 0.25% according to the numerical aperture of $NA = 0.1$ of the optics, whereas, nearly all of the diffractive light due to absorption with $NA_{\text{d}} = \sin \theta_{\text{d}} = 1.22\lambda/d_{\text{Airy}} = 0.015$ is collected by the optics, where θ_{rd} is the diffraction half-angle of the Airy disk, and $d_{\text{Airy}} \simeq 4w_0$ is the Airy disk diameter matched to the $1/e$ radius w_0 of the Gaussian diffraction pattern.

Within this data set (Fig. 6.4), we were able to resolve down to 105 atoms corresponding to an optical density of $D = 0.016$. The lowest resolvable cloud is limited by the Poissonian noise of the residual background on the images of the atoms. The residual background light from the probe beam gives rise to a structured pattern on the image plane similar to that on Fig. 6.2(c). Subtracting the reference image from the image of the atoms results in removing the structure from the images. The resulting images (Fig. 6.3) have a flat background with an mean value averaged throughout the data set of 0.18 counts/pixel and an averaged standard deviation of 6.2 counts/pixel. The noise of 6.2 counts/pixel comes from the Poissonian noise of the residual background, which is not eliminated after subtracting the reference image. The background on the images before subtracting the reference has a mean of 81 counts/pixel corresponding to a Poissonian noise of 9 counts/pixel. The disagreement with the measured standard deviation of 6.2 counts/pixel is attributed to the fact that a structured background is replaced with its mean value for predicting a Poissonian noise of 9 counts/pixel. The average measured standard deviation on the images of 6.2 counts/pixel corresponds to an minimum (SNR=1) detectable optical density of $D = 0.019$, thus the lowest detected signal is limited by the Poissonian noise of the residual background.

For a free expanding atom cloud originally trapped in a MOT, the optical density is low, which limits the lowest resolvable atom number. Having atom clouds of smaller size by using stronger magnetic confinement, and cooling the sample below the temperatures typical for a MOT results in an increase in the density of the atom cloud and in an increase in the signal to noise.

By using the same method and optics in a BEC setup on strongly confined atom clouds cooled down with evaporative cooling we were able to resolve down to 7 atoms at an optical density of $D = 0.02$ [72]. In this experiment, magnetic fields are used to split the atomic sample into three wells with each well having an $1/e$ radius of $\sim 5 \mu\text{m}$. The atom number on the wells measured with the diffraction dark-ground technique is compared to classical absorption imaging, and very good agreement is found between the two methods. In addition, diffractive dark-ground imaging displays 10 times higher SNR as compared to absorption imaging.

Higher optical resolution of the imaging system will enable the detection of even smaller more compact atom clouds with an increased signal to noise. Considerable work has been done by the post-doc fellow worker on the experiment on the development on a high resolution objective based on the objective in [74] achieving a measured resolution of $1.2 \mu\text{m}$. Resolving cloud radii of this range would result in an increase in the SNR by a factor of greater than 10.

6.4 Conclusions

We have used diffractive dark-ground imaging, a Fourier-filtering technique with resonant probe beam, as a sensitive imaging technique to image atom clouds of $14 \mu\text{m}$ $1/e$ radius trapped in a MOT of atom numbers down to 100 atoms. We have been able to resolve very low optical densities of the order of 0.01 limited by the background. The atoms originally trapped in a MOT were imaged in free space at an exposure time of $100 \mu\text{s}$. The background was suppressed with an extinction ratio of 800 using a $200 \mu\text{m}$ dark spot. Dark spots of larger diameter result in higher background suppression, though they reduce the transmission of the light from the atoms. The latter can be avoided by having more compact atom clouds of smaller size. The size of the atom clouds imaged from a MOT limits the lowest resolvable atom number. We have been able to resolve down to 7 atoms at the same range of optical densities using the same technique and optics in a BEC setup on tightly confined ultra-cold clouds in wells of $10 \mu\text{m}$ $1/e$ diameter each. We have used moderate optics with $NA = 0.1$ and a resolution of $9 \mu\text{m}$. Using optics with higher resolution (for example [7, 74]) will enable the observation of even lower atom numbers at smaller more compact atom clouds with an increased signal to noise.

Appendix A

Constants and Rb Properties

Table A.1: Fundamental Physical Constants (2006 CODATA [75]).

Speed of Light	c	$2.997\,924\,58 \times 10^8$ m/s
Permeability of Vacuum	μ_o	$4\pi \times 10^{-7}$ N/A ²
Permittivity of Vacuum	ϵ_o	$8.854\,187\,817\dots \times 10^{-12}$ F/m
Planck's Constant	h	$6.626\,068\,96(33) \times 10^{-34}$ J · s
		$4.135\,667\,33(10) \times 10^{-15}$ eV · s
Boltzmann's Constant	\hbar	$1.054\,571\,628(53) \times 10^{-34}$ J · s
		$6.582\,118\,99(16) \times 10^{-15}$ eV · s
Boltzmann's Constant	k_B	$1.380\,6504(24) \times 10^{-23}$ J/K
Electron Charge	e	$1.602\,176\,487(40) \times 10^{-19}$ C
Electron Mass	m_e	$9.109\,382\,15(45) \times 10^{-31}$ kg
Atomic Mass Unit	u	$1.660\,538\,782(83)^{-27}$ kg
Bohr Magneton	μ_B	$9.274\,009\,15(23) \times 10^{-24}$ J/T
Bohr Radius	a_o	$0.529\,177\,208\,59(36) \times 10^{-10}$ m
Fine Structure Constant	α	1/137.036

Table A.2: Rubidium 87 Physical Properties [76–78]

Atomic Mass	m	86.909 180 520(15) u
Atomic Number	Z	37
Atomic Nucleons	$Z + N$	87
Relative Natural Abundance	$\eta(^{87}\text{Rb})$	27.83(2)%
Nuclear Lifetime	τ_n	4.88×10^{10} yr
Density at 25°C	ρ_m	1.53 g/cm ³
Vapor pressure at 25°C	P_v	$3.92(20) \times 10^{-7}$ torr
Specific Heat Capacity	c_p	0.363 J/g · K
Nuclear Spin	I	3/2
Ionization Limit	E_I	4.177 127 06(10) eV

Table A.3: Rubidium 87 D₂ ($5^2\text{S}_{1/2} \rightarrow 5^2\text{P}_{3/2}$) Optical Properties [57, 79, 80]

Frequency	ω_0	$2\pi \cdot 384.230\,484\,468\,5(62)$ THz
Transition Energy	$\hbar\omega_0$	1.589 049 462(38) eV
Wavelength	λ	780.241 209 686(13) nm
Lifetime	τ	26.2348(77) ns
Natural Line Width (FWHM)	Γ	$2\pi \cdot 6.0666(18)$ MHz
Saturation Intensity (σ^\pm -polarized light)	I_{sat}	1.669 33(35) mW/cm ²
Saturation Intensity (π -polarized light)		2.503 99(52) mW/cm ²
Absorption Cross Section	σ_o	$2.907\,692\,937\,721(66) \times 10^{-15}$ m ²
Recoil Velocity	v_r	5.8845 mm/s
Recoil Energy	ω_r	$2\pi \cdot 3.7710$ kHz
Recoil Temperature	T_r	361.96 nK
Doppler Temperature	T_D	145.57 μ K

Table A.4: ^{87}Rb D Transition Magnetic and Electric Field Interaction Parameters [75, 81, 82].

Electron spin g -factor	g_S	2.002 319 304 3622(15)
Electron orbital g -factor	g_L	0.999 993 69
Fine structure Landé g -factor	$g_J(5^2S_{1/2})$	2.002 331 13(20)
	$g_J(5^2P_{3/2})$	1.3362(13)
Nuclear g -factor	g_I	−0.000 995 1414(10)
Ground-state polarizability	$a_0(5^2P_{1/2})$	$h \cdot 0.0794(16) \text{ Hz}/(\text{V}/\text{cm})^2$
D_2 scalar polarizability	$a_0(5^2P_{3/2}) - a_0(5^2S^{1/2})$	$h \cdot 0.1340(8) \text{ Hz}/(\text{V}/\text{cm})^2$
D_2 tensor polarizability	$a_2(5^2P_{3/2})$	$h \cdot -0.0406(8) \text{ Hz}/(\text{V}/\text{cm})^2$

Bibliography

- [1] W. Ketterle, D. S. Durfee, and D. M. Stamper-Kurn. *Making, Probing and understanding Bose-Einstein Condensates. Bose-Einstein Condensation in Atomic Gases, International School of Physics "Enrico Fermi" 1998, Varenna.* IOS Press, 1999.
- [2] Frits Zernike. Phase contrast, A new method for the microscopic observation of transparent objects, Part I. *Physica*, 9:7:686, 1942.
- [3] Frits Zernike. Phase contrast, A new method for the microscopic observation of transparent objects, Part II. *Physica*, 9:10:974, 1942.
- [4] M. R. Andrews, C. G. Townsend, H.-J. Miesner, D. S. Durfee, D. M. Kurn, and W. Ketterle. Observation of interference between two bose condensates. *Science*, 275:637, 1997.
- [5] J. R. Abo-Shaeer, C. Raman, J. M. Vogels, and W. Ketterle. Observation of vortex lattices in Bose-Einstein condensates. *Science*, 292:476, 2001.
- [6] M. Albiez, R. Gati, Jonas Fölling, S. Hunsmann, M. Cristiani, and M. K. Oberthaler. Direct observation of tunneling and nonlinear self-trapping in a single bosonic Josephson junction. *Phys. Rev. Lett.*, 95:010402, 2005.
- [7] J. Estève, C. Gross, A. Weller, S. Giovanazzi, and M. K. Oberthaler. Squeezing and entanglement in a Bose-Einstein condensate. *Nature*, 455:1216, 2008.
- [8] B. Darquié, M. P. A. Jones, J. Dingjan, J. Beugnon, S. Bergamini, Y. Sortais, G. Messin, A. Browaeys, and P. Grangier. Controlled single-photon emission from a single trapped two-level atom. *Science*, 309:454, 2005.
- [9] T. Wilk, S. C. Webster, A. Kuhn, and G. Rempe. Single-atom single-photon quantum interface. *Science*, 317:488, 2007.
- [10] J. Volz, M. Weber, D. Schlenk, W. Rosenfeld, J. Vrana, K. Saucke, C. Kurtsiefer, and H. Weinfurter. Observation of entanglement of a single photon with a trapped atom. *Phys. Rev. Lett.*, 96:030404, 2006.
- [11] E. Raab, M. Prentiss, A. Cable, S. Chu, and D. Pritchard. Trapping of neutral sodium atoms with radiation pressure. *Phys. Rev. Lett.*, 59:2631, 1987.

- [12] W.D. Phillips. Nobel lecture: Laser cooling and trapping of neutral atoms. *Rev. Mod. Phys.*, 70:721, 1998.
- [13] S. Chu. Nobel lecture: The manipulation of neutral particles. *Rev. Mod. Phys.*, 70:685, 1998.
- [14] C. Cohen-Tannoudji. Nobel lecture: Manipulating atoms with photons. *Rev. Mod. Phys.*, 70:707, 1998.
- [15] Z. Hu and H. J. Kimble. Observation of a single atom in a magneto-optical trap. *Opt. Lett.*, 19:1888, 1994.
- [16] W.D. Phillips and H.J. Metcalf. Laser deceleration of an atomic beam. *Phys. Rev. Lett.*, 48:596, 1982.
- [17] S. Chu, L. Hollberg, J. Bjorkholm, A. Cable, and A. Ashkin. Three dimensional viscous confinement and cooling of atoms by resonance radiation pressure. *Phys. Rev. Lett.*, 55:48, 1985.
- [18] J. Dalibard and C. Cohen-Tannoudji. Laser cooling below the doppler limit by polarization gradient: simple theoretical models. *J. Opt. Soc. Am. B*, 6:2023, 1989.
- [19] P. J. Ungar, D. S. Weiss, E. Riis, and S. Chu. Optical molasses and multilevel atoms: theory. *J. Opt. Soc. Am. B*, 6:2058, 1989.
- [20] H. J. Metcalf and P. van der Straten. *Laser Cooling and Trapping*. Springer Verlag, New York, 1999.
- [21] C. Adams and E. Riis. Laser cooling and trapping of neutral atoms. *Prog. Quant. Electron*, 21:1, 1997.
- [22] S. Stenholm. The semiclassical theory of laser cooling. *Rev. Mod. Phys.*, 58:699, 1988.
- [23] Christopher J. Foot. *Atomic Physics*. Oxford University Press, 2005.
- [24] K.-J. Kugler, W. Paul, and U. Trinks. A magnetic storage ring for neutrons. *Phys. Lett.*, 72B:422, 1978.
- [25] C. Cohen-Tannoudji. Atomic and molecular physics lectures in collége de France. 1996/97.
- [26] T. P. Meyrath. Electromagnet design basics for cold atom experiments. 2003.
- [27] C. Monroe, W. Swann, H. Robinson, and C. Wieman. Very cold trapped atoms in a vapour cell. *Phys. Rev. Lett.*, 65:1571, 1990.
- [28] F. Reif. *Fundamentals of Statistical and Thermal Physics*. McGraw-Hill, New York, 1965.

- [29] K. E. Gibble, S. Kasapi, and S. Chu. Improved magneto-optic trapping in a vapour cell. *Opt. Lett.*, 17:526, 1992.
- [30] J. Weiner, V. Bagnato, S. Zilio, and P. Julienne. Experiments and theory in cold and ultracold collisions. *Rev. Mod. Phys.*, 71:1, 1999.
- [31] D. Hoffmann, S. Bali, and T.G. Walker. Trap-depth measurements using ultracold collisions. *Phys. Rev. A*, 54:R1030, 1996.
- [32] L.G. Marcassa, V.S. Bagnato, Y. Wang, C. Tsao, J. Weiner, O. Dulieu, Y.B. Band, and P.S. Julienne. Collisional loss rate in a magneto-optical trap for sodium atoms: Light-intensity dependence. *Phys. Rev. A*, 47:R4563, 1993.
- [33] T. Walker, D. Sesko, and C. Wieman. Collective behaviour of optically trapped neutral atoms. *Phys. Rev. Lett.*, 64:408, 1990.
- [34] C.D. Wallace, T.P. Dinneen, K.N. Tan, T.T. Grove, and P.L. Gould. Isotopic difference in trap loss collisions of laser cooled rubidium atoms. *Phys. Rev. Lett.*, 69:897, 1992.
- [35] M. Prentiss, A. Cable, J.E. Bjorkholm, S. Chu, E. Raab, and D. Pritchard. Atomic density-dependent losses in an optical trap. *Opt. Lett.*, 13:452, 1988.
- [36] M. H. Anderson, W. Petrich, J. R. Enscher, and E. A. Cornell. Reduction of light-assisted collisional loss rate from a low-pressure vapor cell trap. *Phys. Rev. A*, 50:R3597, 1994.
- [37] U. D. Rapol, A. Wasan, and V. Natarajan. Loading of a Rb magneto-optic trap from a getter source. *Phys. Rev. A*, 64:023402, 2001.
- [38] B. Ueberholz, S. Kuhr, D. Frese, V. Gomer, and D. Meschede. Cold collisions in a high-gradient magneto-optical trap. *J. Phys. B: At.Mol. Opt. Phys.*, 35:4899, 2002.
- [39] B. P. Anderson and M. A. Kasevitch. Spatial observation of Bose-Einstein condensation of ^{87}Rb in a confining potential. *Phys. Rev. A*, 59:938, 1999.
- [40] O. Mandel, M. Greiner, A. Widera, T. Rom, and T. W. Hänsch and I. Bloch. Coherent transport of neutral atoms in spin-dependent optical lattice potentials. *Phys. Rev. Lett.*, 91:010407, 2003.
- [41] Wolfgang Demetroder. *Laser Spectroscopy*. Springer, 1998.
- [42] Melina Pappa. *Imaging Bose-Einstein condensates at ultra-low atom-numbers and time averaged adiabatic potentials*. PhD thesis, University of Crete, 2011.
- [43] E. W. Streed, A. P. Chikkatur, T. L. Gustavson, M. Boyd, Y. Torii, D. Schneble, G. K. Campbell, D. E. Pritchard, and W. Ketterle. Large atom number Bose-Einstein condensate machines. *Rev. Sci. Instrum.*, 77:023106, 2006.

- [44] E. Hecht. *Optics*. Addison Wesley, Massachusetts, 1987.
- [45] M. R. Andrews, M-O. Mewes, N. J. van Druten, D. S. Durfee, and D. M. Kurn W. Ketterle. Direct, nondestructive observation of a bose condensate. *Science*, 273:84, 1996.
- [46] Bradley C.C., Sackett A., and Hulet R.G. Bose-Einstein condensation of lithium: Observation of limited condensate number. *Phys. Rev. Lett.*, 78:985, 1996.
- [47] Bradley C.C., Sackett A., and Hulet R.G. Analysis of in situ images of Bose-Einstein condensate of lithium. *Phys. Rev. A*, 55:3951, 1996.
- [48] R. Meppelink, R. A. Rozendaal, S. B. Koller, J. M. Vogels, and P. van der Straten. Thermodynamics of Bose-Einstein condensed clouds using phase-contrast imaging. *Phys. Rev. A*, 81:053632, 2010.
- [49] M. R. Andrews, D. M. Kurn, H.-J. Miesner, D. S. Durfee, C. G. Townsend, S. Inouye, and W. Ketterle. Propagation of sound in a Bose-Einstein condensate. *Phys. Rev. Lett.*, 79:553, 1997.
- [50] M. R. Andrews, C. G. Townsend, H.-J. Miesner, D. S. Durfee, D. M. Kurn, and W. Ketterle. Observation of interference between two Bose condensates. *Science.*, 275:637, 1997.
- [51] L. D. Turner, K. F. E. M. Domen, and R. E. Scholten. Diffraction-contrast imaging of cold atoms. *Phys. Rev. A*, 72:031403, 2005.
- [52] R. Newell S. Kadlecek, J. Sebby and T. G. Walker. Nondestructive spatial heterodyne imaging of cold atoms. *Opt. Lett.*, 26:137, 2001.
- [53] Daniel A. Steck. *Rubidium 87 line data*. 2001.
- [54] J. Goodman. *Introduction to Fourier Optics*. Roberts & Co Publishers, (3rd ed.), 2005.
- [55] R. Carpentier and R.-J. Champeau. A simple though rigorous method for dealing with spatial filtering problems. *Eur. J. Phys.*, 24:543, 2003.
- [56] E. Belbruno. Random walk in celestial mechanics. *Regul. Chaotic Dyn.*, 14:7, 2009.
- [57] J. Ye, S. Swartz, P. Jungner, and J. Hall. Hyperfine structure and absolute frequency of the $^{87}\text{Rb } ^5\text{P}_{3/2}$ state. *Opt. Lett.*, 21:1280, 1996.
- [58] S. Bize, Y. Sortais, M. Santos, C. Mandache, A. Clairon, and C. Salomon. High-accuracy measurement of the ^{87}Rb ground-state hyperfine splitting in an atomic fountain. *Europhys. Lett.*, 45 (5):558, 1999.

- [59] C. Hawthorn, K. Weber, and R. Scholten. Littrow configuration tunable external cavity diode laser with fixed direction output beam. *Rev. Sci. Instrum.*, 72:4477, 2001.
- [60] T. Hof, D. Fick, and H. J. Jansch. Application of diode lasers as a spectroscopic tool at 670 nm. *Opt. Commun.*, 124:283, 1996.
- [61] J. Wilson A. Arnold and M. Boshier. A simple extended-cavity diode laser. *Rev. Sci. Instrum.*, 69:1236, 1998.
- [62] K. L. Corwin, Z.-T. Lu, C. F. Hand, R. J. Epstein, and C. E. Wieman. Frequency-stabilized diode laser with the Zeeman shift in an atomic vapor. *Appl. Opt.*, 37:3295, 1998.
- [63] N. Beverini, E. Maccioni, P. Marsili, A Ruffini, and F. Sorrentino. Frequency stabilization of a diode laser on the Cs D_2 resonance line by the zeeman effect in a vapor cell. *Appl. Phys. B*, 73:133, 2001.
- [64] C. J. Myatt, N. R. Newbury, and C. E. Wieman. Simplified atom trap by using direct microwave modulation of a diode laser. *Opt. Lett.*, 18:649, 1993.
- [65] Gustav Wikström. Trapping and imaging of single neutral atoms. Master's thesis, Umeå University, 2010.
- [66] D. Schrader, I. Dotsenko, M. Khudaverdyan, Y. Miroshnychenko, A. Rauschenbeutel, and D. Meschede. Neutral atom quantum register. *Phys. Rev. Lett.*, 93:150501, 2004.
- [67] D. Frese, B. Ueberholz, S. Kuhr, W. Alt, D. Schrader, V. Gomer, and D. Meschede. Single atoms in an optical dipole trap: Towards a deterministic source of cold atoms. *Phys. Rev. Lett.*, 85:3777, 2000.
- [68] S. Bakr, J. I. Gillen, A. Peng, S. Fölling, and M. Greiner. A quantum gas microscope for detecting single atoms in a Hubbard-regime optical lattice. *Nature*, 462:74, 2009.
- [69] R. Bücker, A. Perrin, S. Manz, T. Betz, Ch. Koller, T. Plisson, J. Rottmann, T. Schumm, and J. Schmiedmayer. Single-particle-sensitive imaging of freely propagating ultracold atoms. *New J. Phys.*, 11:103039, 2009.
- [70] Brian Phillip Anderson. *Bose-Einstein condensation and macroscopic interference with atomic tunnel arrays*. PhD thesis, Stanford University, 2000.
- [71] G. O. Konstantinidis, M. Pappa, G. Wikström, P. C. Condylis, M. Baker, O. Morizot, and W. von Klitzing. Imaging of ultra-low atom numbers in a magneto-optic trap using optical fourier filtering. arXiv, 2011.

- [72] M. Pappa, P. C. Condylis, G. O. Konstantinidis, V. Bolpasi, A. Lazoudis, O. Morizot, D. Sahagun, M. Baker, and W. von Klitzing. Ultra-sensitive atom imaging for matter-wave optics. *New J. Phys.*, 13:115012, 2011.
- [73] C. F. Ockeloen, A. F. Tauschinsky, R. J. C. Spreeuw, and S. Whitlock. Detection of small atom numbers through image processing. *Phys. Rev. A*, 82:061606, 2010.
- [74] Timo B. Ottenstein. A new objective for high resolution imaging of bose-einstein condensates. Master's thesis, University of Heidelberg, 2006.
- [75] P. J. Mohr, B. N. Taylor, and D. B. Newell. *The 2006 CODATA Recommended Values of the Fundamental Physical Constants*. Web Version 5.1, available at <http://physics.nist.gov/constants> (National institute of Standards and Technology), December 2007.
- [76] David R. Lide (Ed.). *CRC Handbook of Chemistry and Physics*. 82nd ed. CRC Press, Boca Raton, 2001.
- [77] M. P. Bradley, J. V. Porto, S. Rainville, J. K. Thompson, and D. E. Pritchard. Penning trap measurements of the masses of ^{133}Cs , $^{87,85}\text{Rb}$, and ^{23}Na with uncertainties ≤ 0.2 ppb. *Phys. Rev. Lett.*, 83:4510, 1999.
- [78] S. A. Lee, J. Helmcke, J. L. Hall, and B. P. Stoicheff. Doppler-free two-photon transitions to Rydberg levels: convenient, useful, and precise reference wavelengths for dye lasers. *Opt. Lett.*, 3:141, 1978.
- [79] G. P. Barwood, P. Gill, and W. R. C. Rowley. Frequency measurements on optically narrowed Rb-stabilised laser diodes at 780 nm and 795 nm. *Appl. Phys. B*, 53:142, 1991.
- [80] R. F. Gutterres, C. Amiot, A. Fioretti, C. Gabbanini, M. Mazzoni, and O. Dulieu. Determination of the ^{87}Rb $5p$ state dipole matrix element and radiative lifetime from the photoassociation spectroscopy of the rb_2 $0_g-(P_{3/2})$ long-range state. *Phys. Rev. A*, 66:024502, 2002.
- [81] E. Arimondo, M. Inguscio, and P. Violino. Experimental determinations of the hyperfine structure in the alkali atoms. *Rev. Mod. Phys.*, 49:31, 1977.
- [82] C. Krenn, W. Scherf, O. Khait, M. Musso, and L. Windholz. Stark effect investigations of resonance lines of neutral potassium, rubidium, europium and gallium. *Z. Phys. D*, 41:229, 1997.